UNIVERSITY OF Southampton

University of Southampton Research Repository
ePrints Soton

Copyright © and Moral Rights for this thesis are retained by the author and/or other copyright owners. A copy can be downloaded for personal non-commercial research or study, without prior permission or charge. This thesis cannot be reproduced or quoted extensively from without first obtaining permission in writing from the copyright holder/s. The content must not be changed in any way or sold commercially in any format or medium without the formal permission of the copyright holders.

When referring to this work, full bibliographic details including the author, title, awarding institution and date of the thesis must be given e.g.

AUTHOR (year of submission) "Full thesis title", University of Southampton, name of the University School or Department, PhD Thesis, pagination

http://eprints.soton.ac.uk

UNIVERSITY OF Southampton

Faculty of Engineering and the Environment

Computer simulation studies of complex magnetic materials

by **Weiwei Wang**

Thesis for the degree of
Doctor of Philosophy

Supervisors: Prof. Hans Fangohr, Dr. Ian Hawke

October 2015

UNIVERSITY OF SOUTHAMPTON

ABSTRACT

FACULTY OF ENGINEERING AND THE ENVIRONMENT

Doctor of Philosophy

COMPUTER SIMULATION STUDIES OF COMPLEX MAGNETIC MATERIALS

by Weiwei Wang

With the development of both computing power and software engineering, computer simulation of the micromagnetic model or atomistic spin model, has become an important tool for studying a wide range of different complex phenomena in magnetic materials. Meanwhile, the rapid improvement of advanced measurement techniques has allowed the probing of ultrafast magnetization dynamics, as well as the magnetic phenomena involving charge current, heat and light. The simulation of magnetism is now moving towards a multiphysics method. Therefore, fast, user-friendly, and extensible codes with accurate algorithms are helpful in understanding the physics and designing novel magnetic devices on the nanoscale.

In the preparation of this thesis we have developed Fidimag, which is a Python/C simulation tool supporting both micromagnetic and atomistic spin models. The software has also been extended to support the Landau-Lifshitz-Baryakhtar (LLBar) equation. Using Fidimag, we have performed simulations to study the domain-wall motion and spin-wave decay with the LLBar equation. We also explain the exchange damping in the LLBar equation as the phenomenological nonlocal damping by linking it to spin pumping, therefore, LLBar equation can be considered as a phenomenological equation of the nonlocal damping.

We studied magnon-induced domain-wall motion in the presence of Dzyaloshinskii-Moriya interaction (DMI) numerically and theoretically. We find that the presence of DMI and easy-plane anisotropy can drive the domain wall very effectively and that the domain-wall velocity depends on the sign of DMI constant. While the negative velocity is considered as a result of angular momentum conservation, we attribute this fast domain-wall motion to linear momentum transfer between magnons and the domain wall. By numerically solving the Landau-Lifshitz-Gilbert equation with a classical spin model on a two-dimensional system, we show that both magnetic skyrmions and skyrmion lattices can be moved with microwave magnetic fields. The mechanism is enabled by breaking the axial symmetry of the skyrmion with a static in-plane external field.

Contents

Declaration of Authorship xi

List of publications xii

Acknowledgements xiii

1 Introduction 1
- 1.1 Background . . . 1
- 1.2 Structure of this thesis . . . 4

2 Micromagnetic and Atomistic modeling 5
- 2.1 Magnetic moments . . . 6
- 2.2 Equation of Motion . . . 6
- 2.3 Interactions . . . 7
  - 2.3.1 Exchange interaction . . . 8
  - 2.3.2 Dzyaloshinskii-Moriya interaction (DMI) . . . 8
  - 2.3.3 Dipolar interaction . . . 10
  - 2.3.4 Anisotropy . . . 10
  - 2.3.5 Zeeman energy . . . 11
- 2.4 Atomistic spin model . . . 11
- 2.5 Micromagnetics . . . 13
  - 2.5.1 Exchange energy . . . 14
  - 2.5.2 Magnetostatic energy . . . 14
  - 2.5.3 Dzyaloshinskii-Moriya Energy . . . 15
- 2.6 Landau-Lifshitz-Gilbert (LLG) equation . . . 16
  - 2.6.1 Spherical form of LLG equation . . . 17
  - 2.6.2 Spin transfer torque . . . 18
  - 2.6.3 Nonlocal spin transfer torque . . . 19
- 2.7 Finmag and Fidimag . . . 20

3 Fidimag 21
- 3.1 Introduction . . . 21
- 3.2 Fast Summation of Dipolar interactions . . . 22
  - 3.2.1 Fast Summation . . . 23
  - 3.2.2 Dipolar interaction in triangular lattice . . . 23
- 3.3 Landau-Lifshitz-Baryakhtar equation . . . 24
- 3.4 Eigenvalue Method . . . 25
- 3.5 Verification I . . . 27

3.5.1 A magnetic moment under an external magnetic field 27
3.5.2 Domain-wall motion under charge currents 27
3.5.3 Magnetic skyrmions 30
3.5.4 Normal modes of a spin chain 32
3.6 Stochastic LLG equation 34
3.7 Verification II 35
3.7.1 A magnetic moment 35
3.7.2 Equilibrium distribution of a nanoparticle 36
3.7.3 Magnon temperature 36

4 Phenomenological description of nonlocal damping 39
4.1 Introduction 39
4.2 Basic equations 41
4.3 Spin-wave decay 45
4.4 Domain-wall motion 48
4.4.1 Parallel relaxation 51
4.4.2 Nonlocal damping 53
4.5 Ferromagnetic resonance (FMR) 54
4.6 Summary 56

5 Magnon-driven domain-wall motion with Dzyaloshinskii-Moriya interaction 57
5.1 Introduction 57
5.2 The system 58
5.3 Domain-wall profile and Spin-wave excitation 59
5.4 Domain-wall motion 61
5.5 Two types of domain walls 65
5.6 Summary 67

6 Driving magnetic skyrmions with microwave fields 69
6.1 Introduction 69
6.2 The system and asymmetric skyrmions 70
6.3 Spin waves modes 72
6.4 Skyrmion motion 73
6.5 Summary 77

7 Conclusion and Outlook 79
7.1 Conclusion 79
7.2 Outlook 80

A 81
A.1 Section A 81
A.2 Section B 82
A.3 Section C 82
A.4 Section D 83

B Using discontinuous Galerkin Methods 85
B.1 Introduction 85
B.2 Laplace operator using CG method 85

B.3 Background . . . 86
B.3.1 H(div) space . . . 86
B.3.2 BDM space . . . 87
B.3.3 Piola mapping . . . 87
B.4 Using BDM space . . . 88
B.5 MFMFE . . . 89
B.6 A Test . . . 89

C Treecode for Boundary Element Method **91**
C.1 General problem . . . 91
C.2 Treecode . . . 91
C.2.0.1 Particle-cluster interactions . . . 92
C.2.0.2 Recurrence relations of Taylor coefficients . . . 93
C.2.0.3 Implementation of Treecode . . . 94
C.2.1 Combine Treecode with FEM/BEM . . . 95
C.3 Numerical Tests . . . 96
C.4 Improvement . . . 97
C.5 Summary . . . 99

Bibliography **101**

List of Figures

2.1 Three heat reservoirs (spin, lattice and electron) model. 11

3.1 Structure of Fidimag. 21
3.2 Triangular lattice embedded in rectangular mesh. 24
3.3 The procession motion of a magnetic moment. 28
3.4 Domain-wall motion driven by spin transfer torque. 29
3.5 Two types of skymrions. 30
3.6 Belavin-Polyakov skyrmion. 32
3.7 Normal modes of a spin chain. 33
3.8 Average magnetization of a magnetic moment. 35
3.9 Equilibrium distribution of a nanoparticle 36
3.10 Equilibrium magnetization of a spin chain. 37

4.1 The spin-wave amplitude decay along a rod. 46
4.2 Frequency-dependent spin-wave decay. 47
4.3 Domain-wall velocities with different susceptibilities. 49
4.4 Magnetization length difference of a domain wall. 50
4.5 Domain-wall velocities for different exchange dampings. 53
4.6 Dynamic susceptibility of an elliptical-shaped nanomagnet. 55
4.7 Fitted damping from dynamic susceptibility. 55

5.1 Domain-wall profile in the presence of DMI 59
5.2 The domain-wall displacements. 62
5.3 The domain-wall velocity for $K_\perp = 0$. 62
5.4 The domain-wall velocity for $K_\perp > 0$ 63
5.5 The wavevector of magnons changes. 65
5.6 Two types of domain walls. 66

6.1 Skyrmion configurations. 71
6.2 Dynamical susceptibility χ_{zz} of skyrmions. 72
6.3 The velocities of a single skyrmion. 73
6.4 Total spatial force density. 74
6.5 Spatial force density. 76
6.6 The velocities of skyrmion lattices. 77

B.1 An unstructured mesh. 90
B.2 Comparison of DG and CG methods. 90

C.1 The particle-cluster interaction. 92

C.2 Memory usage for Treecode and FK methods 96
C.3 Relative error comparison. 97
C.4 Comparison of running time. 98

List of Tables

2.1 Typical transport parameters of soft NiFe alloy. 20

3.1 RK2a scheme. 34
3.2 RK2b scheme. 34
3.3 RK2c scheme. 34
3.4 RK3 scheme. 34

6.1 Unit conversion table 72

B.1 Compute matrix in BDM space. 88

C.1 The algorithm of treecode method. 94

Declaration of Authorship

I, Weiwei Wang, declare that the thesis entitled *Computer simulation studies of complex magnetic materials* and the work presented in the thesis are both my own, and have been generated by me as the result of my own original research. I confirm that:

- this work was done wholly or mainly while in candidature for a research degree at this University;
- where any part of this thesis has previously been submitted for a degree or any other qualification at this University or any other institution, this has been clearly stated;
- where I have consulted the published work of others, this is always clearly attributed;
- where I have quoted from the work of others, the source is always given. With the exception of such quotations, this thesis is entirely my own work;
- I have acknowledged all main sources of help;
- where the thesis is based on work done by myself jointly with others, I have made clear exactly what was done by others and what I have contributed myself;
- parts of this work have been published as: [1], [2] and [3].

Signed:.....

Date:.....

List of publications

1. W. Wang, M. Dvornik, M.-A. Bisotti, D. Chernyshenko, M. Beg, M. Albert, A. Vansteenkiste, B. V. Waeyenberge, A. N. Kuchko, V. V. Kruglyak, and H. Fangohr, *Phenomenological description of the nonlocal magnetization relaxation in magnonics, spintronics, and domain-wall dynamics*, Physical Review B **92**, 054430 (2015).

2. W. Wang, M. Albert, M. Beg, M.-A. Bisotti, D. Chernyshenko, D. Cortés-Ortuño, I. Hawke and H. Fangohr, *Magnon-Driven Domain-Wall Motion with the Dzyaloshinskii-Moriya Interaction*, Physical Review Letters **114**, 087203 (2015).

3. Weiwei Wang, Marijan Beg, Bin Zhang, Wolfgang Kuch and Hans Fangohr, *Driving magnetic skyrmions with microwave fields*, Physical Review B **92**, 020403(R) (2015).

4. Bin Zhang, Weiwei Wang, Marijan Beg, Hans Fangohr and Wolfgang Kuch, *Microwave-induced dynamic switching of magnetic skyrmion cores in nanodots*, Applied Physics Letters **106**, 102401 (2015).

5. P. J. Metaxas, M. Sushruth, R. A. Begley, J. Ding, R. C. Woodward, I. S. Maksymov, M. Albert, W. Wang, H. Fangohr, A. O. Adeyeye, and M. Kostylev, *Sensing magnetic nanoparticles using nano-confined ferromagnetic resonances in a magnonic crystal*, Applied Physics Letters **106**, 232406 (2015).

6. Simone Borlenghi, Weiwei Wang, Hans Fangohr, Lars Bergqvist and Anna Delin, *Designing a spin-seebeck diode*, Physical Review Letters, **112**, 047203 (2014).

7. D. Kumar, P. Sabareesan, W. Wang, H. Fangohr and A. Barman, *Effect of Hole Shape on Spin-Wave Band Structure in One-Dimensional Magnonic Antidot Waveguide*, Journal of Applied Physics, **114**, 023910 (2013).

Acknowledgements

Firstly, I would like to thank my supervisor Prof. Hans Fangohr for giving me the chance to perform this work. Prof. Hans Fangohr is an excellent supervisor and working with him was a real pleasure. I appreciate his continuous support during the whole period of my PhD study. Similar acknowledgments go to my second supervisor, Dr. Ian Hawke, for providing support with his mathematical expertise when I was lost in equations.

I would like to thank Prof. Volodymyr V. Kruglyak, Dr. Mykola Dvornik, Dr. Dheeraj Kumar, Dr. Simone Borlenghi, Dr. Bin Zhang and Prof. Wolfgang Kuch for the stimulating discussions as well as their contributions to the publications related to this work.

I owe a big thank to all the Finmag team members: Dmitri Chernyshenko, Marc-Antonio Bisotti, Maximilian Albert, Marijan Beg, Rebecca Carey, Mark Vousden and David Cortés-Ortuño. I am especially thankful to Dmitri Chernyshenko and Marc-Antonio Bisotti from whom I learned a lot about programming and software tools and to Maximilian Albert with whom I had many fruitful conversations. I also really appreciate the great help from Marijan Beg throughout the PhD. He also helped me a lot in solving travel issues.

I would also like to thank Ryan Pepper and Marijan Beg for their patient and precise proofreading of this thesis. I acknowledge financial support from China Scholarship Council and EPSRC's DTC Grant.

最后，感谢父母一直以来的理解与支持。

Chapter 1

Introduction

1.1 Background

The various phenomena in magnetic materials are closely related to our daily life. Recorded knowledge of magnetism goes back to the distant past. For example, in ancient China, the earliest literary mention of magnetism is in a 4th-century B.C. book *The Master of Demon Valley*. It has been suggested that hematite might have been used as a magnet by the Olmec earlier than 1000 B.C. [4]. However, the use of magnetic materials has been limited until very recently. This is because people knew very little about the theory behind magnetics.

Things began to change in the 1800s. The first milestone was Maxwell's electromagnetic theory, in which the macroscopic electrical and magnetic phenomena are unified by differential equations. After that, the importance of magnetic materials became recognized. For example, people managed to use magnetic materials to generate alternating currents. The second milestone was the development of quantum theory. This allowed the use of magnetism on much smaller scales, culminating today at the nanoscale.

Nowadays, the application of magnetic materials is broad, with uses in data storage, magnetoresistive random-access memory [5], magnetic sensors [6] and logic devices [7]. Meanwhile, new research topics such as spin caloritronics and magnonics develop quickly. As computing power has increased, simulations of the micromagnetic model [8] and the atomistic spin model [9] have become an important tool to study the complex phenomena in magnetic materials. These simulations have allowed the study of the dynamics of spin waves, domain walls, vortices and skyrmions.

Magnonics is a young developing research field that emerged recently [10, 11] although the concept of spin waves was introduced by Bloch 80 years ago. Magnons are the particle-like spin excitations in magnetic mediums while the wave-like counterpart are known as spin waves [12]. Both quantum mechanical and classical properties can

be found in spin waves. Due to new techniques in tailoring ferromagnetic materials, phenomena such as spin wave interference [13] have been observed and thus stimulated the fast development of field of magnonics.

As the quanta of spin waves, magnons obey Bose-Einstein statistics. Indeed, Bose-Einstein condensation (BEC) of magnons was demonstrated in various magnetic systems [14], and even at room temperature in yttrium-iron garnets (YIG) [15, 16]. The density n_0 of the room temperature BEC is unknown but quite low and satisfies $n_0/n \ll 1$ where n is the pumped density of the magnons [17]. Because of this the BEC can survive despite the attractive intermagnon interactions. Furthermore, it was suggested that the repulsive interactions could emerge by changing the field configuration so that the BEC could stabilize at a much higher density [17].

It is believed that periodically patterned magnetic materials in the nanoscale will be used in the future [12]. The propagation of waves in periodically shaped media is of special interest in modern physics and technology [11]. The magnonic crystal is the magnetic counterpart of the photonic crystal [18]. Recently, various types of magnonic crystals have been studied both theoretically and experimentally [19–22]. A typical method to manipulate the band structure of spin waves in these magnonic crystals is to use periodic modulation of nanostrip widths [22]. Storage-recovery phenomena were demonstrated in an artificial crystal with a limited number of periods by employing a quasinormal mode [23].

From the classical point of view, spin waves are the phase-coherent precessions of microscopic vectors of magnetization in the magnetic material, which gives us the opportunity to use mature micromagnetic tools to study the spin-wave dynamics. With the fast development of computational power, numerical micromagnetic simulations start to play more important roles in magnonics. The existing micromagnetic tools are based on two numerical techniques, i.e., the finite difference method (FDM) such as OOMMF [24] and the finite element method (FEM) such as Magpar [25] and Nmag [26]. It is well known that the FDM is not suitable for irregular samples while FEM does not have this limitation. The demagnetizing field calculations are complex, and while due to the short range interaction we would expect the exchange field calculation to be less complex, this is not the case due to the irregularity of cells in FEM. The common method used in FEM to compute the exchange fields is the so-called box method. For unstructured (irregular) meshes the error of the box method could be significant and even worse than $O(h)$ where h is the element edge length [27].

Usually, the finite element method in this context refers to the continuous Galerkin method as implemented in existing FEM micromagnetics packages [25, 26]. The saturation magnetization is stored in cells (tetrahedra for 3D) but the unit magnetization vectors are attached in nodes for the dynamics which is generally governed by the Landau-Lifshitz-Gilbert equation (LLG). This modeling is slightly inconsistent especially when

information about the saturation magnetization is needed in the LLG equation for multi-materials, such as the spin transfer torque case [28]. This inspired us to look for other possible FEM techniques in numerical micromagnetics.

Spin caloritronics [29] is a young developing research field that involves with spin and heat currents. In the presence of temperature gradients, magnetic solitons such as magnetic domain walls and magnetic skyrmions move [30–33]. Experimentally, thermal-driven domain-wall motion has been observed in a magnetic insulator YIG (yttrium iron garnet) film [34]. A common and powerful tool used in spin caloritronics is the stochastic LLG (SLLG) equation used both at the micromagnetic and atomistic levels. For example, the SLLG equation at the atomistic level is used to study domain wall and skyrmion dynamics [30, 33] while the SLLG equation at the micromagnetic level is used in studying domain-wall motion [31] and magnon spin currents [35, 36].

The spin-wave amplitude decays when propagating in the media due to energy dissipation and therefore how the relaxation process is described is a critical problem, attracting great research interest [37–41]. In the LLG equation the damping term is characterized by the Gilbert damping constant. Phenomenologically, the Gilbert damping term can be derived from the Lagrange equation with Rayleigh's dissipation term by assuming the magnetization is uniform [8] which means that the Gilbert damping is local. Different forms of damping including nonlocal effects have been suggested, for example, a tensor form of magnetization damping was proposed to describe the magnetization relaxation processes of a uniformly magnetized film [39]. Enhanced damping phenomena in thin ferromagnetic films were observed in experiments [38], and this is explained by the spin current pumping from the ferromagnetic layer to the nonmagnetic metal [42]. A recent experiment on permalloy in nanoscale shows that the damping is dependent on its shape and size [41], which confirms that the damping is nonlocal.

The Dzyaloshinskii-Moriya interaction (DMI) [43, 44] is an antisymmetric interaction arising from spin-orbit coupling due to broken inversion symmetry in lattices or at the interface of magnetic films. The most fascinating part about the DMI is that two spins are in the lowest energy state when they are perpendicular rather than parallel or anti-parallel. The existence of DMI leads to new magnetic profiles and dynamics. For example, a domain wall is curled in the presence of DMI and the domain-wall motion under an external field [45] or charge current [46] is also modified.

A stable magnetization profile that can exist due to the existence of the DMI is the skyrmion [47], which is a topologically stable soliton. Unlike the vortex state, a skyrmion can exist in the ferromagnetic background. Skyrmions are considered to have potental application in data storage and thus the dynamics is of great interest. A skyrmion can be driven by charge currents [48, 49], magnetic or electric field gradients [32, 50] and spin waves [33, 51]. It is of interest to find new ways to control the skyrmion motion.

1.2 Structure of this thesis

What follows is a brief outline of this thesis. In Chapter 2 we will provide a short introduction about the classical spin model and micromagnetics. We start from a basic concept in magnetism – the magnetic moment, and write down the equation of motion (Landau-Lifshitz-Gilbert equation), as well as the common interactions between magnetic moments. In Chapter 3 we will introduce our finite different micromagnetic/atomistic simulation package – Fidimag, which was developed throughout the work contained in this thesis. Some implementation details and verifications for Fidimagwill be presented.

Chapter 4 will present the details of nonlocal damping. We will first explain the exchange damping in the Landau-Lifshitz-Baryakhtar equation as nonlocal damping by linking it to the spin current pumping. The spin-wave propagation along a single rod will be studied using micromagnetic simulations and analytical calculations. Furthermore, the domain-wall motion under an external field will be studied using the Landau-Lifshitz-Baryakhtar equation.

In Chapter 5 we will study domain-wall motion driven by spin waves (magnons) in the presence of the Dzyaloshinskii-Moriya interaction (DMI). In general, when spin waves pass through a domain wall, the spin waves transfers spin angular momentum to it and thus the domain wall moves towards to the magnon source. In the presence of the DMI, the spin waves on the two branches of domains have different wavevectors. We will show this wavevector change leads to a fast domain-wall motion. We attribute this to linear momentum transfer.

Chapter 6 will be devoted to the study of magnetic skyrmions driven by microwave fields. In this study we will solve the Landau-Lifshitz-Gilbert equation numerically with a classical spin model on a two-dimensional system. We will show that both magnetic skyrmions and skyrmion lattices can be moved with microwave magnetic fields if the axial symmetry of the skyrmions is broken by a static in-plane external field. The net velocity of the skyrmion depends on the frequency and amplitude of the microwave fields as well as the strength of the in-plane field.

In Appendix B a method called called multipoint flux mixed finite element method (MFMFE) is implemented to compute the exchange field for irregular cells such as triangles and tetrahedra in micromagnetics. In Appendix C we will introduce a treecode method in computing the demagnetizing fields.

Chapter 2

Micromagnetic and Atomistic modeling

Both Maxwell's electromagnetic theory and quantum theory were well developed by the 1930s. However, both theories are not enough to describe various phenomena such as the hysteresis loops of ordered spin structures and macroscopic magnetization processes [52]. Maxwell's electromagnetic theory has been verified experimentally in a large range of scales, from microscopic to macroscopic. In media, the magnetic induction **B** and electric field **E** in Maxwell's equations can be considered as the statistical average of the microscopic electromagnetic field **e** and **h** in an element of media [53]

$$\mathbf{E} = \langle \mathbf{e} \rangle_{\text{element}} \qquad \mathbf{B} = \langle \mathbf{h} \rangle_{\text{element}}. \tag{2.1}$$

This is because microscopically, the electrons are not static and the atoms vibrate, which results in the micro-electric field **e** and micro-magnetic field **h** being highly nonuniform in time and space [53]. The most basic macroscopic magnetic properties of materials can not be understood without quantum theory [54], although quantum theory gives a description of magnetic properties on the atomistic level [52]. The development of the continuum theory for micromagnetism was intended to bridge the gap between Maxwell's theory and quantum theory, which became necessary after Barkhausen's experiment, known as Barkhausen's jumps and the domain-wall velocity experiment performed by Sixtus and Tonks [52]. The model was developed quickly after Heisenberg and Dirac's explanation of ferromagnetism based on the exchange interactions, and Landau and Lifshitz derived a continuum expression for the exchange energy. This allowed an interpretation of domain patterns, which was a breakthrough toward the continuum theory of magnetism.

Today, the atomistic spin model has become an essential tool in understanding various complex behaviors of magnetic nanomaterials [9, 55], such as surface anisotropy in

magnetic nanoparticles, ultrafast laser-induced magnetization dynamics and temperature effects [9]. The dynamics of novel magnetic textures such as magnetic skyrmions can be modeled using the atomistic spin model [47]. The atomistic spin model can be considered as a natural extension of the Ising model: the atomic spin is allowed to vary freely in 3D space while in the Ising model, a spin only has two states – spin-up and spin-down [55]. The Ising model has been studied extensively for phase transition problems, however this model is too simplistic and can not be applied to study dynamic simulations of magnetic materials. As we will see in this Chapter, the atomistic spin model combined with the Landau-Lifshitz-Gilbert equation can deal with the dynamics, even in the presence of temperature [56].

2.1 Magnetic moments

Magnetic moment is a fundamental object in magnetism; classically it is equivalent to a current loop, or a magnetic dipole. In atoms the magnetic moment $\boldsymbol{\mu}$ is associated with its spin angular momentum $\mathbf{S}$ and orbital angular momentum $\mathbf{L}$. For metal systems with quenched orbital moments, the magnetic moment is mainly related to the spin angular momentum

$$\boldsymbol{\mu} = -g\mu_B \mathbf{S}, \tag{2.2}$$

where $g = 2$ is the Lande factor and $\mu_B = |e|\hbar/(2m)$ is the Bohr magneton. Here the local spin $\mathbf{S} = \mathbf{S}(\mathbf{r})$ is treated as a classical variable [57], thus its relation to magnetization is

$$\mathbf{M}(\mathbf{r}) = -\frac{\hbar\gamma}{\Omega(\mathbf{r})}\mathbf{S}(\mathbf{r}), \tag{2.3}$$

where $\gamma = g\mu_B/\hbar$ (> 0) is the gyromagnetic ratio and $\Omega(\mathbf{r})$ is the local atomic volume per magnetic ion. For a simple cubic lattice, $\Omega(\mathbf{r}) = a^3$ where a is the lattice constant.

2.2 Equation of Motion

According to Ehrenfest's theorem, the expectation value of an operator A (assuming A has no explicit time dependence) can be given by

$$\frac{d}{dt}\langle\hat{A}\rangle = \frac{i}{\hbar}\langle[\hat{\mathcal{H}}, \hat{A}]\rangle, \tag{2.4}$$

where $[\mathcal{H}, A]$ is the usual commutator. Considering an electron under a magnetic field $\mathbf{H}$ with the Hamiltonian operator

$$\mathcal{H} = g\mu_B \mathbf{H} \cdot \hat{\mathbf{S}}, \tag{2.5}$$

where $\hat{\mathbf{S}}$ is the spin angular momentum operator. By using the angular momentum commutation relations $[\hat{S}_i, \hat{S}_j] = i\epsilon_{ijk}\hat{S}_k$ and Eq. (2.4), the expectation value of $\hat{\mathbf{S}}$ becomes

$$\frac{d}{dt}\langle\hat{\mathbf{S}}\rangle = -\gamma\langle\hat{\mathbf{S}}\rangle \times \mathbf{H}. \tag{2.6}$$

Note that Eq. (2.6) holds true for a time-dependent magnetic field $\mathbf{H}$ [58]. Therefore, the dynamics of the magnetic moment $\boldsymbol{\mu}$ is governed by the equation

$$\frac{d}{dt}\boldsymbol{\mu} = -\gamma\boldsymbol{\mu} \times \mathbf{H}. \tag{2.7}$$

As we can see, the energy is conserved if the dynamics is governed by Eq. (2.7). In reality, the magnetic moments are subject to energy dissipation arising from different sources such as phonons [57]. Phenomenologically an extra damping term can be added to Eq. (2.7) and the Landau-Lifshitz-Gilbert (LLG) equation is obtained [8],

$$\frac{\partial\boldsymbol{\mu}}{\partial t} = -\gamma\boldsymbol{\mu} \times \mathbf{H} + \frac{\alpha}{\mu_s}\boldsymbol{\mu} \times \frac{\partial\boldsymbol{\mu}}{\partial t}. \tag{2.8}$$

where $\mu_s = |\boldsymbol{\mu}|$ and α is a dimensionless damping constant – the Gilbert damping parameter. This damping constant α is phenomenological, and α is usually less than 0.1 in Fe, Co, Ni metals or alloys [53]. In Permalloy, the damping is even less than 0.01. The Gilbert damping term also emerges by employing a modified Hamiltonian $\hat{H} = \hat{\mathcal{H}} - i\lambda(\hat{\mathcal{H}} - \langle\hat{\mathcal{H}}\rangle)$ where λ is the damping constant [59]. Equation (2.8) can be rewritten in a dimensionless form

$$\frac{\partial\mathbf{m}}{\partial t} = -\gamma\mathbf{m} \times \mathbf{H}_{\text{eff}} + \alpha\mathbf{m} \times \frac{\partial\mathbf{m}}{\partial t}, \tag{2.9}$$

where $\mathbf{m} = \boldsymbol{\mu}/\mu_s$ is the unit vector of the magnetic momentum and $\mathbf{H}_{\text{eff}}$ represents the total effective field arising from various interactions.

2.3 Interactions

There are several typical interactions between magnetic moments, such as the exchange interaction, anisotropy interaction, dipolar interaction, Dzyaloshinskii-Moriya interaction and Zeeman interaction. The total Hamiltonian is the summation of these

$$\mathcal{H} = \mathcal{H}_{\text{ex}} + \mathcal{H}_{\text{dmi}} + \mathcal{H}_{\text{d}} + \mathcal{H}_{\text{an}} + \mathcal{H}_{\text{a}}, \tag{2.10}$$

where $\mathcal{H}_{\text{ex}}$, $\mathcal{H}_{\text{dmi}}$, $\mathcal{H}_{\text{d}}$, $\mathcal{H}_{\text{an}}$ and $\mathcal{H}_{\text{a}}$ are the Hamiltonians of the exchange interaction, Dzyaloshinskii-Moriya interaction, dipolar interaction, anisotropy interaction and Zeeman interaction, respectively. The effective field $\mathbf{H}_{\text{eff}}$ can be computed from the total

Hamiltonian $\mathcal{H}$

$$\mathbf{H}_{\text{eff}} = -\frac{1}{\mu_s}\frac{\partial \mathcal{H}}{\partial \mathbf{m}}. \tag{2.11}$$

2.3.1 Exchange interaction

The exchange interaction is the strongest magnetic interaction and the most difficult one to treat theoretically [60]. The classical Heisenberg Hamiltonian with the nearest-neighbor exchange interaction is given by

$$\mathcal{H}_{\text{ex}} = -J\sum_{\langle i,j\rangle}\mathbf{m}_i\cdot\mathbf{m}_j, \tag{2.12}$$

where $\langle i,j\rangle$ represents a unique pair between lattice sites i and j and we assume that the summation is taken only once for each pair. The strength of exchange interaction is indicated by the exchange constant J. A positive J leads to the ferromagnetic state since the Hamiltonian [Eq. (2.12)] is minimal when the magnetic moments $\mathbf{m}_i$ and $\mathbf{m}_j$ are parallel while a negative J results in the antiferromagnetic state. Note that if we write $\mathcal{H}_{\text{ex}} = -\tilde{J}\sum_{\langle i,j\rangle}\mathbf{S}_i\cdot\mathbf{S}_j$ then we have $J = \tilde{J}S^2$. The effective exchange field at site i can be computed as

$$\mathbf{H}_{\text{ex,i}} = \frac{J}{\mu_s}\sum_{\langle i,j\rangle}\mathbf{m}_j. \tag{2.13}$$

2.3.2 Dzyaloshinskii-Moriya interaction (DMI)

In a more general form, the Hamiltonian of Heisenberg exchange [Eq. (2.12)] can be extended to

$$\mathcal{H}_{\text{ex}} = -\sum_{\langle i,j\rangle}\mathbf{S}_i^T\hat{\mathcal{A}}_{ij}\mathbf{S}_j, \tag{2.14}$$

where $\hat{\mathcal{A}}_{ij} = \{A_{ij}^{\mu\nu}\}$ with $\mu,\nu = x,y,z$ is the exchange tensor. We can decompose $\hat{\mathcal{A}}_{ij}$ into three parts, i.e.,

$$\hat{\mathcal{A}}_{ij} = J_{ij}\mathcal{I} + \hat{\mathcal{A}}_{ij}^s + \hat{\mathcal{A}}_{ij}^a, \tag{2.15}$$

where $\mathcal{I}$ is the unit tensor and J_{ij} is the isotropic exchange coefficient,

$$J_{ij} = \frac{1}{3}\text{Tr}(\hat{\mathcal{A}}_{ij}). \tag{2.16}$$

This is why the exchange interaction [Eq. (2.12)] is called the isotropic exchange interaction. The traceless symmetric anisotropic exchange tensor $\hat{\mathcal{A}}_{ij}^s$ is defined by

$$\hat{\mathcal{A}}_{ij}^s = \frac{1}{2}(\hat{\mathcal{A}}_{ij} + \hat{\mathcal{A}}_{ij}^T) - J_{ij}\mathcal{I}, \tag{2.17}$$

and the antisymmetric exchange matrix tensor can be computed as

$$\hat{\mathcal{A}}_{ij}^{a} = \frac{1}{2}(\hat{\mathcal{A}}_{ij} - \hat{\mathcal{A}}_{ij}^{T}). \tag{2.18}$$

Hence, the Hamiltonian [Eq. (2.14)] can be rewritten as

$$\mathcal{H}_{\text{ex}} = -\sum_{\langle i,j \rangle} J_{ij}\mathbf{S}_i \cdot \mathbf{S}_j - \sum_{\langle i,j \rangle} \mathbf{S}_i^T \hat{\mathcal{A}}_{ij}^{s}\mathbf{S}_j - \sum_{\langle i,j \rangle} \mathbf{S}_i^T \hat{\mathcal{A}}_{ij}^{a}\mathbf{S}_j. \tag{2.19}$$

The last term (the antisymmetric part) of Hamiltonian [Eq. (2.19)] can be recast into

$$\mathcal{H}_{\text{dmi}} = \sum_{\langle i,j \rangle} \tilde{\mathbf{D}}_{ij} \cdot (\mathbf{S}_i \times \mathbf{S}_j), \tag{2.20}$$

where

$$\tilde{D}_{ij}^{x} = A_{ij}^{zy} - A_{ij}^{yz}, \quad \tilde{D}_{ij}^{y} = A_{ij}^{xz} - A_{ij}^{zx}, \quad \tilde{D}_{ij}^{z} = A_{ij}^{yx} - A_{ij}^{xy}. \tag{2.21}$$

This antisymmetric exchange interaction was first studied by Dzyaloshinskii (1958) [43] and Moriya (1960) [44]. Dzyaloshinskii predicted that the combination of symmetry and spin-orbit couplings can lead to antisymmetric exchange interactions and Moriya found a microscopic mechanism which gives rise to such antisymmetric terms in systems with spin-orbit couplings. Therefore, the anisotropic exchange interaction [Eq. (2.20)] is known as the Dzyaloshinskii-Moriya interaction (DMI). As we can see, the isotropic exchange coefficient $\mathcal{J}_{ij}$ and the pseudovector $\tilde{\mathbf{D}}_{ij}$ have different symmetry properties:

$$\mathcal{J}_{ij} = \mathcal{J}_{ji}, \quad \tilde{\mathbf{D}}_{ij} = -\tilde{\mathbf{D}}_{ji}. \tag{2.22}$$

In general the DMI can arise from the spin-orbit interaction and the vector $\tilde{\mathbf{D}}$ lies parallel or perpendicular to the line connecting the two spins [54, 61]. For the parallel case, one can assume $\tilde{\mathbf{D}}_{ij} = \tilde{D}\hat{\mathbf{r}}_{ij}$ while for the perpendicular case one can assume $\tilde{\mathbf{D}}_{ij} = \tilde{D}\hat{\mathbf{r}} \times \mathbf{e}_z$ if both spins are located in the xy-plane [62]. The former actually corresponds to the bulk DMI while the latter is the interfacial DMI. This two types DMI have been found in bulk materials such as MnSi [63] and FeGe [64], as well as in magnetic interfaces [62]. Therefore, the Hamiltonian for DMI can be written as

$$\mathcal{H}_{\text{dmi}} = \sum_{\langle i,j \rangle} \mathbf{D}_{ij} \cdot [\mathbf{m}_i \times \mathbf{m}_j], \tag{2.23}$$

where $\mathbf{D}_{ij} = \tilde{\mathbf{D}}_{ij}S^2$. The corresponding effective field can be computed by

$$\mathbf{H}_{\text{dmi,i}} = -\frac{1}{\mu_s}\frac{\partial \mathcal{H}_{\text{dmi}}}{\partial \mathbf{m}_i} = \frac{1}{\mu_s}\sum_{\langle i,j \rangle} \mathbf{D}_{ij} \times \mathbf{m}_j, \tag{2.24}$$

where the identity $\mathbf{a} \cdot (\mathbf{b} \times \mathbf{c}) = (\mathbf{a} \times \mathbf{b}) \cdot \mathbf{c}$ is used.

2.3.3 Dipolar interaction

The dipolar interaction is a long-range interaction. The Hamiltonian for dipolar interaction between magnetic moments $\boldsymbol{\mu}_i$ and $\boldsymbol{\mu}_j$ is

$$\mathcal{H}_{\mathrm{d}} = -\frac{\mu_0 \mu_s^2}{4\pi} \sum_{i<j} \frac{3(\mathbf{m}_i \cdot \hat{\mathbf{r}}_{ij})(\mathbf{m}_j \cdot \hat{\mathbf{r}}_{ij}) - \mathbf{m}_i \cdot \mathbf{m}_j}{r_{ij}^3}, \tag{2.25}$$

where r_{ij} is the distance between two magnetic moments. Therefore, the effective field can be computed by

$$\mathbf{H}_{\mathrm{d,i}} = \frac{\mu_0 \mu_s}{4\pi} \sum_{i \neq j} \frac{3\hat{\mathbf{r}}_{ij}(\mathbf{m}_j \cdot \hat{\mathbf{r}}_{ij}) - \mathbf{m}_j}{r_{ij}^3}. \tag{2.26}$$

2.3.4 Anisotropy

In the presence of anisotropy, a magnetic moment tends to align along some preferred direction. Many physical effects can lead to an anisotropy, for instance, the magnetocrystalline anisotropy can arise from the interaction between local crystal environment and atomic electron orbitals [55]. The simplest form of the anisotropy is the so-called uniaxial anisotropy, and its Hamiltonian is given by

$$\mathcal{H}_{\mathrm{an}} = -K \sum_i (\mathbf{m}_i \cdot \mathbf{u})^2,$$

where the unit vector $\mathbf{u}$ is the easy axis and the constant K represents the anisotropy strength. The corresponding effective field due to the uniaxial anisotropy is

$$\mathbf{H}_{\mathrm{an,i}} = \frac{2K}{\mu_s} (\mathbf{m}_i \cdot \mathbf{u}) \mathbf{u}. \tag{2.27}$$

Some materials such as Nickel have a cubic crystal structure, and thus they have a different form of anisotropy called cubic anisotropy. The Hamiltonian of cubic anisotropy is given by

$$\mathcal{H}_{\mathrm{an}}^c = K_c \sum_i (m_x^4 + m_y^4 + m_z^4). \tag{2.28}$$

By using the identity $m_x^2 + m_y^2 + m_z^2 = 1$, it is straightforward to see that the Hamiltonian [Eq. (2.28)] is equivalent to the form

$$\mathcal{H}_{\mathrm{an}}^c = -2K_c \sum_i (m_x^2 m_y^2 + m_y^2 m_z^2 + m_z^2 m_x^2). \tag{2.29}$$

2.3.5 Zeeman energy

The effective field of a magnetic moment in the presence of an external field $\mathbf{H}_\mathrm{a}$ is obviously $\mathbf{H}_\mathrm{a}$ itself. This also can be seen from the Zeeman energy given by

$$\mathcal{H}_\mathrm{a} = -\mu_s \sum_i \mathbf{m}_i \cdot \mathbf{H}_\mathrm{a}. \tag{2.30}$$

2.4 Atomistic spin model

By treating the spin as a classical variable, the dynamics of atomic spin is governed by the LLG equation (2.9). Various physical effects are considered through the total effective field $\mathbf{H}_\mathrm{eff}$, which can be computed by the total Hamiltonian. The reason to use the atomistic spin model rather than the continuum micromagnetic model is that, for some cases the continuum micromagnetic model may fail. In general, there are two ways to establish the parameters in the atomistic spin model [55]: using *ab initio* density functional theory calculations or determined by experiments.

The LLG equation (2.9) does not contain the temperature effect, which is only applicable for simulations at zero temperature. In reality, the temperature is involved in magnetic system. In general three types of excitations can be stored in a ferromagnetic solid: the energy of electrons, the excitation of phonons, and the excitation of magnons. In this framework, the magnetization dynamics can be understood within the three thermodynamic subsystems: the spin system, the lattice and the electronic system [9, 60].

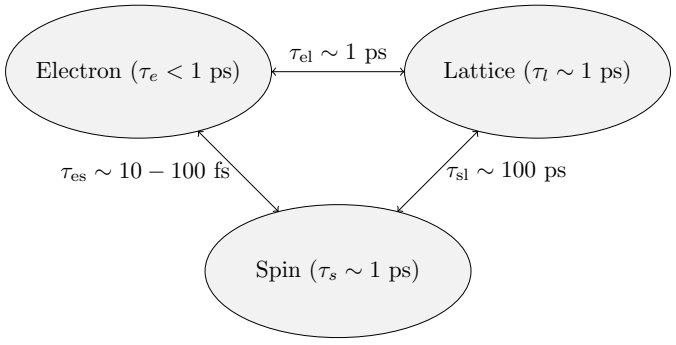

Figure 2.1: Three heat reservoirs in a ferromagnetic metal. All three reservoirs also can be separately excited. Approximate relaxation times within the reservoirs and between the reservoirs are included. Figure is adapted from Ref. [9].

Energy can be exchanged between the three subsystems, as shown in Fig. 2.1. It is important to realize that the angular momentum transfer is accompanied when the energy is transfered to or from the spin system and in this case the angular momentum

needs to be conserved as well. The timescale of the spin-lattice relaxation time τ_{sl} is of the order 100 picoseconds (ps), which is slower than the electron-lattice relaxation time τ_{el} ($\tau_{el} \sim 1$ ps) [9]. Compared with them, the spin-electron relaxation time τ_{es} is slightly fast, which has been found to be at the order of 100 fs.

When the spin system is connected to a thermal reservoir, thermal excitations can be generated by adding a stochastic field to the effective field in the standard LLG equation (2.9), in this way, the effect of temperature is included for magnetic dynamics. The LLG equation with stochastic field $\boldsymbol{\xi}$ is

$$\frac{\partial \mathbf{m}}{\partial t} = -\gamma \mathbf{m} \times (\mathbf{H}_{\text{eff}} + \boldsymbol{\xi}) + \alpha \mathbf{m} \times \frac{\partial \mathbf{m}}{\partial t}. \tag{2.31}$$

The equation (2.31) is the so called stochastic LLG (SLLG) equation. The thermal fluctuation is assumed to be a Gaussian white noise, i.e., the thermal noise $\boldsymbol{\xi}$ obeys the properties

$$\langle \boldsymbol{\xi} \rangle = 0, \quad \left\langle \boldsymbol{\xi}_i^u, \boldsymbol{\xi}_j^v \right\rangle = 2D\delta_{ij}\delta_{uv}, \tag{2.32}$$

where i and j are Cartesian indices, u and v indicate the magnetization components and $\langle \cdot, \cdot \rangle$ represents the average taken over different realizations of the fluctuating field [65]. The constant D denotes the strength of the thermal fluctuations:

$$D = \frac{\alpha k_B T}{\gamma \mu_s}. \tag{2.33}$$

This model [Eqs. (2.31)-(2.33)] is the so called Langevin dynamics model. The strength of D can be determined by the Fokker-Planck equation. The SLLG equation (2.31) can be rewritten in a more general form

$$\frac{dm_i}{dt} = A_i + \sum_k B_{ik} L_k, \tag{2.34}$$

where $L_k = \xi_k$ and

$$\begin{aligned} A_i &= -\frac{\gamma}{1+\alpha^2} \left[\mathbf{m} \times \mathbf{H}_{\text{eff}} + \alpha \mathbf{m} \times (\mathbf{m} \times \mathbf{H}_{\text{eff}}) \right]_i, \\ B_{ik} &= \frac{\gamma}{1+\alpha^2} \left[\alpha(\delta_{ik} - m_i m_k) - \textstyle\sum_j \epsilon_{ijk} m_j \right]. \end{aligned} \tag{2.35}$$

As we can see, the SLLG equation is multiplicative since $\partial B_{ik}/\partial m_j \neq 0$ (the noise is called "additive" if $\partial B_{ik}/\partial m_j = 0$, whereas in this case the Ito stochastic calculus and the Stratonovich stochastic calculus coincide). By using the Stratonovich calculus, the time evolution of nonequilibrium probability distribution $P = P(\mathbf{m}, t)$ is given by the

Fokker-Planck equation [65]:

$$\frac{\partial P}{\partial t} = -\sum_i \frac{\partial}{\partial m_i}\left[\left(A_i - D\sum_k B_{ik}\sum_j \frac{\partial B_{jk}}{\partial m_j} - D\sum_{jk} B_{ik}B_{jk}\frac{\partial}{\partial m_j}\right)P\right]. \tag{2.36}$$

It is found that the second term $\sum_k B_{ik}\sum_j \partial B_{jk}/\partial m_j = 0$ and thus we arrive at

$$\frac{\partial P}{\partial t} = \frac{\partial}{\partial \mathbf{m}}\cdot\left\{\left[\frac{\gamma}{1+\alpha^2}\mathbf{m}\times(\mathbf{H}_{\text{eff}} + \alpha\mathbf{m}\times\mathbf{H}_{\text{eff}}) - \frac{1}{2\tau}\mathbf{m}\times(\mathbf{m}\times\frac{\partial}{\partial\mathbf{m}})\right]P\right\}, \tag{2.37}$$

where $\tau^{-1} = 2D\gamma^2/(1+\alpha^2)$ is the free-diffusion time (also known as Néel time). In thermal equilibrium $P(\mathbf{m})$ have to satisfy the Boltzmann distribution,

$$P_0(\mathbf{m}) \propto \exp[-\beta\mathcal{H}(\mathbf{m})], \tag{2.38}$$

where $\beta = 1/(k_B T)$. Note that the definition of the effective field is given by equation (2.11), so we have $\partial P_0/\partial\mathbf{m} = \mu_s\beta\mathbf{H}_{\text{eff}}P_0$, and thus the first term vanishes since $\partial/\partial\mathbf{m}\,(\mathbf{m}\times\mathbf{H}_{\text{eff}}P_0) = 0$. Hence, the Fokker-Planck equation reduces to

$$\frac{\partial P_0}{\partial t} = \frac{\partial}{\partial \mathbf{m}}\cdot\left\{\left[\frac{\alpha\gamma}{1+\alpha^2}\mathbf{m}\times(\mathbf{m}\times\mathbf{H}_{\text{eff}}) - \frac{\beta\mu_s}{2\tau}\mathbf{m}\times(\mathbf{m}\times\mathbf{H}_{\text{eff}})\right]P_0\right\}. \tag{2.39}$$

The stationary solution requires $\partial P_0/\partial t = 0$, which results in

$$\tau = \frac{(1+\alpha^2)\beta\mu_s}{2\alpha\gamma}. \tag{2.40}$$

Comparing Eq. (2.40) with the Néel time, the amplitude of D in Eq. (2.33) can be obtained.

2.5 Micromagnetics

In the continuum theory, the isolated magnetic moments are replaced by a continuum function, magnetization $\mathbf{M}(\mathbf{r})$, which represents the average moment density over a local volume $V(\mathbf{r}, \Delta r)$,

$$\mathbf{M}(\mathbf{r}) = \frac{1}{V(\mathbf{r},\Delta r)}\sum_i \boldsymbol{\mu}_i. \tag{2.41}$$

In this continuum case, the dynamics of magnetization $\mathbf{M}$ is still governed by the LLG equation (2.9), where $\mathbf{m} = \mathbf{M}(\mathbf{r})/M_s$ with M_s the saturation magnetization. The effective field $\mathbf{H}_{\text{eff}}$ is then calculated as the functional derivative

$$\mathbf{H}_{\text{eff}} = -\frac{1}{\mu_0 M_s}\frac{\delta E}{\delta \mathbf{m}}, \tag{2.42}$$

where E is the total micromagnetic energy, which can be obtained from the total Hamiltonian of the atomistic model on the continuum limit.

2.5.1 Exchange energy

In the continuum limit the isotropic exchange energy can be written as

$$E_{\text{ex}} = \int_{\Omega} A(\nabla \mathbf{m})^2 dx \tag{2.43}$$

where $(\nabla \mathbf{m})^2 = (\nabla m_x)^2 + (\nabla m_y)^2 + (\nabla m_z)^2$. So the corresponding effective field is

$$\mathbf{H}_{\text{ex}} = \frac{2A}{\mu_0 M_s} \nabla^2 \mathbf{m}, \tag{2.44}$$

and the relation between A and J for simple cubic lattice is $J = 2Aa$.

2.5.2 Magnetostatic energy

In the continuum case, the dipolar interaction is represented by the demagnetizing field, also known as the stray field. By applying the Maxwell's equations for the zero macroscopic current case (i.e., only consider the fields due to the magnetic moments), the demagnetizing field in a sample can be computed as the gradient of a magnetic scalar potential Φ

$$\mathbf{H}_d(\mathbf{r}) = -\nabla \Phi(\mathbf{r}) \tag{2.45}$$

The magnetic potential satisfies the equation

$$\nabla^2 \Phi = -\rho_m, \tag{2.46}$$

where $\rho_m = -\nabla \cdot \mathbf{M}$ can be considered as the magnetic volume charge density. Therefore, outside of the sample $\rho_m = 0$. The boundary conditions read

$$\Phi^+ = \Phi^- \tag{2.47}$$

$$\sigma_m = (\nabla \Phi^- - \nabla \Phi^+) \cdot \mathbf{n} \tag{2.48}$$

where $\sigma_m = \mathbf{M} \cdot \mathbf{n}$ is the magnetic surface charge density. With the help of a Green function, the solution of Φ can be obtained

$$\Phi(\mathbf{r}) = \frac{1}{4\pi} \left(\int_V \frac{\rho_m(\mathbf{r}')}{|\mathbf{r} - \mathbf{r}'|} \mathrm{d}^3 r' + \int_S \frac{\sigma_m(\mathbf{r}')}{|\mathbf{r} - \mathbf{r}'|} \mathrm{d}^2 r' \right). \tag{2.49}$$

It is easy to check that the potential decays to zero at infinity. Inserting Eq. (2.49) into Eq. (2.45), the demagnetizing field is given by

$$\mathbf{H}_{\mathrm{d}}(\mathbf{r}) = \frac{1}{4\pi}\left(\int_V \rho_m(\mathbf{r}')\frac{\mathbf{r}-\mathbf{r}'}{|\mathbf{r}-\mathbf{r}'|^3}\mathrm{d}^3r' + \int_S \sigma_m(\mathbf{r}')\frac{\mathbf{r}-\mathbf{r}'}{|\mathbf{r}-\mathbf{r}'|^3}\mathrm{d}^2r'\right). \tag{2.50}$$

From the view point of the energy, the demagnetization energy, also known as magnetostatic energy, is given by

$$E_{\mathrm{d}} = -\frac{\mu_0}{2}\int_V \mathbf{H}_{\mathrm{d}}(\mathbf{r})\cdot\mathbf{M}(\mathbf{r})dV. \tag{2.51}$$

2.5.3 Dzyaloshinskii-Moriya Energy

In the continuum limit the DMI energy can be written as

$$E_{\mathrm{dmi}} = \int_\Omega D_a\mathbf{m}\cdot(\nabla\times\mathbf{m})dx, \tag{2.52}$$

and the effective field is

$$\mathbf{H} = -\frac{2D_a}{\mu_0 M_s}(\nabla\times\mathbf{m}), \tag{2.53}$$

where $D_a = -D/a^2$. For the interfacial case, the effective field thus becomes,

$$\mathbf{H} = \frac{2D}{M_s a^2}(\mathbf{e}_x\times\frac{\partial\mathbf{m}}{\partial y} - \mathbf{e}_y\times\frac{\partial\mathbf{m}}{\partial x}) \tag{2.54}$$

Compared with the effective field of the interfacial DMI [62]

$$\mathbf{H} = \frac{2D_a}{\mu_0 M_s}((\nabla\cdot\mathbf{m})\mathbf{e}_z - \nabla m_z), \tag{2.55}$$

we find $D_a = D/a^2$. Actually, the DM energy density (2.52) is related to the so called *Lifshitz invariants*, which are terms in the form,

$$L_{ij}^{(k)} = m_i\frac{\partial m_j}{\partial x_k} - m_j\frac{\partial m_i}{\partial x_k}. \tag{2.56}$$

The DM energy density has different forms depending on the symmetry class, for example, the energy density (2.52) corresponds to the T symmetry,

$$L = L_{yx}^{(z)} + L_{xz}^{(y)} + L_{zy}^{(x)} = \mathbf{m}\cdot(\nabla\times\mathbf{m}). \tag{2.57}$$

2.6 Landau-Lifshitz-Gilbert (LLG) equation

The LLG equation (2.9) can be rewritten as

$$\frac{\partial \mathbf{m}}{\partial t} = -\frac{\gamma}{1+\alpha^2}\mathbf{m}\times\mathbf{H}_{\text{eff}} - \frac{\alpha\gamma}{1+\alpha^2}\mathbf{m}\times(\mathbf{m}\times\mathbf{H}_{\text{eff}}), \tag{2.58}$$

which is equivalent to the Landau-Lifshitz (LL) equation

$$\frac{\partial \mathbf{m}}{\partial t} = -\gamma_L\mathbf{m}\times\mathbf{H}_{\text{eff}} - \alpha\gamma_L\mathbf{m}\times(\mathbf{m}\times\mathbf{H}_{\text{eff}}). \tag{2.59}$$

if we set $\gamma_L = \gamma/(1+\alpha^2)$. Therefore, Eq. (2.58) is the LL form of LLG equation. The LL equation (2.59) is first introduced by Landau and Lifshitz in 1935 to describe the dispersive theory in ferromagnets [66]. Later, Gilbert derived the LLG equation by using the Lagrangian formulation with a Rayleigh's dissipation function [8]:

$$\frac{d}{dt}\frac{\delta\mathcal{L}(\mathbf{m},\dot{\mathbf{m}})}{\delta\dot{\mathbf{m}}} - \frac{\delta\mathcal{L}(\mathbf{m},\dot{\mathbf{m}})}{\delta\mathbf{m}} + \frac{\delta\mathcal{R}(\dot{\mathbf{m}})}{\delta\dot{\mathbf{m}}} = 0, \tag{2.60}$$

where

$$\mathcal{R}(\dot{\mathbf{m}}) = \frac{\eta_0}{2}\int \dot{\mathbf{m}}\cdot\dot{\mathbf{m}}\, d\mathbf{r} \tag{2.61}$$

is a Rayleigh's dissipation functional [8]. In this case the damping mechanisms is local and uniform. In fact, several nonuniform mechanisms such as rapid spin reorientation in magnetization dynamics can also contribute to the damping [8]. A more general dissipation functional is suggested:

$$\mathcal{R}_{\text{all}}(\dot{\mathbf{m}}) = \frac{1}{2}\int\int \eta(\mathbf{r},\mathbf{r}')\dot{\mathbf{m}}(\mathbf{r},t)\cdot\dot{\mathbf{m}}(\mathbf{r}',t)\, d\mathbf{r}d\mathbf{r}'. \tag{2.62}$$

It can be seen that $\mathcal{R}$ is a special case of $\mathcal{R}_{\text{all}}$ if we set $\eta(\mathbf{r},\mathbf{r}') = \eta_0\delta(\mathbf{r}-\mathbf{r}')$. However, to keep the dissipation simple, the local dissipation functional [Eq. (2.61)] will be used. The Lagrangian $\mathcal{L} = \mathcal{T} - E$ where $\mathcal{T}$ and E are the magnetic kinetic energy and magnetic potential energy, respectively. Inserting the Lagrange $\mathcal{L}$ into Eq. (2.60), one obtains

$$\frac{d}{dt}\frac{\delta\mathcal{T}(\mathbf{m},\dot{\mathbf{m}})}{\delta\dot{\mathbf{m}}} - \frac{\delta\mathcal{T}(\mathbf{m},\dot{\mathbf{m}})}{\delta\mathbf{m}} + (-\mathbf{H}_{\text{eff}} + \eta_0\dot{\mathbf{m}}) = 0. \tag{2.63}$$

By assuming that for $\eta_0 = 0$ case the equation (2.63) corresponds to

$$\frac{\partial \mathbf{m}}{\partial t} = -\gamma\mathbf{m}\times\mathbf{H}_{\text{eff}}, \tag{2.64}$$

the LLG equation (2.9) can be obtained for $\eta_0 > 0$ case with $\alpha = \gamma\eta_0$. In practice we need to use the LL form of the LLG equation [Eq. (2.58)] for numerical implementation.

2.6.1 Spherical form of LLG equation

The length of magnetization unit vector is equal to unity, i.e., $|\mathbf{m}| = 1$. Therefore, the dynamics of magnetization can be described by two variables. In spherical coordinates, the direction of magnetization is determined by the polar angle θ and the azimuthal angle ϕ, that is, $\mathbf{m} = (\sin\theta\cos\phi, \sin\theta\sin\phi, \cos\theta)$. Hence, we have

$$\dot{\mathbf{m}} = \dot{\theta}\mathbf{e}_\theta + \sin\theta\dot{\phi}\mathbf{e}_\phi, \tag{2.65}$$

where

$$\begin{aligned} \mathbf{e}_\theta &= (\cos\theta\cos\phi, \cos\theta\sin\phi, -\sin\theta), \\ \mathbf{e}_\phi &= (-\sin\phi, \cos\phi, 0). \end{aligned} \tag{2.66}$$

Note that $\delta E/\delta\theta = \mathbf{e}_\theta \cdot \delta E/\delta\mathbf{m}$ and $\delta E/\delta\phi = \sin\theta(\mathbf{e}_\phi \cdot \delta E/\delta\mathbf{m})$, so the precessional term $-\gamma\mathbf{m}\times\mathbf{H}_{\text{eff}}$ in LLG equation can be rewritten as

$$\begin{aligned} -\gamma\mathbf{m}\times\mathbf{H}_{\text{eff}} &= \frac{\gamma}{\mu_0 M_s}\left[(\mathbf{e}_\theta\times\mathbf{e}_\phi)\times\frac{\delta E}{\delta\mathbf{m}}\right] = \frac{\gamma}{\mu_0 M_s}\left[(\frac{\delta E}{\delta\mathbf{m}}\cdot\mathbf{e}_\theta)\mathbf{e}_\phi - (\frac{\delta E}{\delta\mathbf{m}}\cdot\mathbf{e}_\phi)\mathbf{e}_\theta\right] \\ &= -\gamma H_\theta\mathbf{e}_\phi + \gamma H_\phi\mathbf{e}_\theta, \end{aligned} \tag{2.67}$$

where the field H_θ and H_ϕ are defined by

$$H_\theta = -\frac{1}{\mu_0 M_s}\frac{\delta E}{\delta\theta}, \qquad H_\phi = -\frac{1}{\mu_0 M_s\sin\theta}\frac{\delta E}{\delta\phi}. \tag{2.68}$$

The damping term in the LLG equation can be rewritten as

$$\alpha\mathbf{m}\times\dot{\mathbf{m}} = \alpha\dot{\theta}\mathbf{e}_\phi - \alpha\sin\theta\dot{\phi}\mathbf{e}_\theta, \tag{2.69}$$

where we have used $\mathbf{m}\times\mathbf{e}_\theta = \mathbf{e}_\phi$ and $\mathbf{m}\times\mathbf{e}_\phi = -\mathbf{e}_\theta$. Therefore, we arrive at the spherical form of LLG equation:

$$\begin{aligned} \dot{\theta} + \alpha\sin\theta\dot{\phi} &= \gamma H_\phi, \\ \alpha\dot{\theta} - \sin\theta\dot{\phi} &= \gamma H_\theta. \end{aligned} \tag{2.70}$$

The spherical form of LLG equation (2.70) also can be derived from the Euler-Lagrange equation,

$$\frac{d}{dt}\left(\frac{\delta\mathcal{L}}{\delta\dot{X}}\right) - \frac{\delta\mathcal{L}}{\delta X} + \frac{\delta\mathcal{R}}{\delta\dot{X}} = 0, \tag{2.71}$$

where X refers to θ and ϕ. The Lagrangian $\mathcal{L}$ is given by

$$\mathcal{L} = \int_\Omega \frac{\mu_0 M_s}{\gamma}\dot{\phi}(1-\cos\theta)\,dV - E, \tag{2.72}$$

where $(\mu_0 M_s/\gamma)\dot{\phi}(1-\cos\theta)$ is the Berry phase term that plays the role of magnetic kinetic energy. The dissipation is given by

$$\mathcal{R} = \int_\Omega \frac{\alpha\mu_0 M_s}{2\gamma}\left(\dot{\theta}^2 + \sin^2\theta\dot{\phi}^2\right) dV. \tag{2.73}$$

2.6.2 Spin transfer torque

The discovery of giant magnetoresistance (GMR) shows that the resistance of a ferromagnetic conductor depends on its magnetization configuration. This suggests that there is an interaction between the conduction electrons and the magnetization, which changes its electric conductivity. In the opposite direction, the flow of an electric current will affect the magnetization dynamics. Indeed, conduction electrons transfer the spin angular momentum to the magnetization of a ferromagnet [67, 68]. Interestingly, Zhang and Li found that [28] most of the physics on the interplay between the magnetization dynamics of local moments and the spin-polarized transport of itinerant electrons can be mostly captured by the s-d model. The extended LLG equation with the spin transfer torque is given by [28, 57, 69],

$$\frac{\partial \mathbf{m}}{\partial t} = -\gamma\mathbf{m}\times\mathbf{H}_{\text{eff}} + \alpha\mathbf{m}\times\frac{\partial\mathbf{m}}{\partial t} + u_0(\mathbf{j}\cdot\nabla)\mathbf{m} - \beta u_0[\mathbf{m}\times(\mathbf{j}\cdot\nabla)\mathbf{m}] \tag{2.74}$$

where $\mathbf{j}$ is the spin-polarized electric current. The parameter u_0 is given by

$$u_0 = \frac{Pg\mu_B}{2eM_s} = \frac{Pg\mu_B a^3}{2e\mu_s}, \tag{2.75}$$

where μ_B is the Bohr magneton, P is the spin polarization of the electric current, $e(>0)$ is the electronic charge and M_s is the saturation magnetization. Equation (2.74) is also known as Zhang-Li extension. The last term in Eq. (2.74) is called nonadiabatic β-term, which is very important for the domain-wall motion driven by spin transfer torque even the value of β is relatively small.

Equation (2.74) also have other formats, for example, the adiabatic term can be rewritten as $u_0(\mathbf{j}\cdot\nabla)\mathbf{m} = -u_0\mathbf{m}\times[\mathbf{m}\times(\mathbf{j}\cdot\nabla)\mathbf{m}]$ if we noticed $\mathbf{m}\cdot\partial_x\mathbf{m} = 0$. For numerical purpose, we change Eq. (2.74) into its LL form,

$$\begin{aligned}(1+\alpha^2)\frac{\partial\mathbf{m}}{\partial t} =& -\gamma\mathbf{m}\times\mathbf{H}_{\text{eff}} - \alpha\gamma\mathbf{m}\times(\mathbf{m}\times\mathbf{H}_{\text{eff}}) \\ &+ (1+\alpha\beta)u_0(\mathbf{j}\cdot\nabla)\mathbf{m} - (\beta-\alpha)u_0[\mathbf{m}\times(\mathbf{j}\cdot\nabla)\mathbf{m}].\end{aligned} \tag{2.76}$$

Furthermore, we take an extra step to remove the longitudinal component of $(\mathbf{j}\cdot\nabla)\mathbf{m}$ although in principle $\partial_x\mathbf{m}$ is always perpendicular to $\mathbf{m}$, therefore, Eq. (2.74) becomes

$$(1+\alpha^2)\frac{\partial\mathbf{m}}{\partial t} = -\gamma\mathbf{m}\times\mathbf{H}_\perp + \alpha\gamma\mathbf{H}_\perp + (1+\alpha\beta)u_0\boldsymbol{\tau}_\perp - (\beta-\alpha)u_0(\mathbf{m}\times\boldsymbol{\tau}_\perp) \tag{2.77}$$

where $\boldsymbol{\tau} = (\mathbf{j}\cdot\nabla)\mathbf{m}$ is the effective torque generated by current. If we assume $\mathbf{u} = u_0 j\mathbf{e}_z$, the Eq. (2.74) can be rewritten in spherical form

$$\begin{aligned}\dot{\theta} + \alpha\sin\theta\dot{\phi} &= \gamma H_\phi + u\theta' - u\beta\sin\theta\phi',\\ \alpha\dot{\theta} - \sin\theta\dot{\phi} &= \gamma H_\theta + u\beta\theta' - u\sin\theta\phi',\end{aligned} \tag{2.78}$$

where we have used $\partial_z\mathbf{m} = \theta'\mathbf{e}_\theta + \sin\theta\phi'\mathbf{e}_\phi$ and $\mathbf{m}\times(\partial_z\mathbf{m}) = \theta'\mathbf{e}_\phi - \sin\theta\phi'\mathbf{e}_\theta$.

2.6.3 Nonlocal spin transfer torque

In deriving the LLG equation (2.74) to include the spin transfer torque effect, the magnetization is assumed to vary slowly in space, e.g., the domain-wall width is much larger than the transport length scale [28]. In the slow magnetization approximation, the spatial derivative of the nonequilibrium spin density $\delta\mathbf{m}$ can be discarded. However, when the domain wall (such as an atomically sharp domain wall) is very thin, this assumption is no longer valid. In this case, the LLG equation with spin transfer torque is given by,

$$\frac{\partial\mathbf{m}}{\partial t} = -\gamma\mathbf{m}\times\mathbf{H}_{\text{eff}} + \alpha\mathbf{m}\times\frac{\partial\mathbf{m}}{\partial t} + \mathbf{T}, \tag{2.79}$$

where $\mathbf{T}$ is the spin transfer torque. In the slow magnetization approximation, it is given by

$$\mathbf{T}_{\text{loc}} = u_0(\mathbf{j}\cdot\nabla)\mathbf{m} - \beta u_0[\mathbf{m}\times(\mathbf{j}\cdot\nabla)\mathbf{m}]. \tag{2.80}$$

In general case, the spin transfer torque can be computed by [28]

$$\mathbf{T} = -\frac{\mathbf{m}\times\delta\mathbf{m}}{\tau_{\text{sd}}}, \tag{2.81}$$

where $\tau_{sd} = 2\pi\hbar/J_{\text{ex}}$ is the s-d exchange time. Meanwhile, the nonequilibrium spin density $\delta\mathbf{m}$ is governed by

$$\frac{\partial\delta\mathbf{m}}{\partial t} = D\nabla^2\delta\mathbf{m} + \frac{\mathbf{m}\times\delta\mathbf{m}}{\tau_{\text{sd}}} - \frac{\delta\mathbf{m}}{\tau_{\text{sf}}} + u_0(\mathbf{j}\cdot\nabla)\mathbf{m}, \tag{2.82}$$

where D is the diffusion constant and τ_{sf} is the spin-flip time. By changing Eq. (2.79) into LL form, we obtain

$$(1+\alpha^2)\frac{\partial\mathbf{m}}{\partial t} = -\gamma\mathbf{m}\times\mathbf{H}_{\text{eff}} - \alpha\gamma\mathbf{m}\times(\mathbf{m}\times\mathbf{H}_{\text{eff}}) - \frac{\mathbf{m}\times\delta\mathbf{m}}{\tau_{\text{sd}}} + \alpha\frac{\delta\mathbf{m}}{\tau_{\text{sd}}}. \tag{2.83}$$

Therefore, for the general case, the dynamics of the magnetization can be obtained by solving Eqs. (2.82) and (2.83) simultaneously.

Table 2.1: Typical transport parameters of soft NiFe alloy [70].

Variable	Symbol	Value
diffusion constant	D	2.5×10^{-4} m^2/s
spin-flip time	τ_{sf}	4×10^{-15} s
s-d exchange time	τ_{sd}	1×10^{-13} s

Table 2.1 shows the typical transport parameters for soft NiFe alloy [70], the spin-flip time τ_{sf} and the s-d exchange time τ_{sd} can be derived from the diffusion length $\lambda_{sf} = \sqrt{D\tau_{sf}}$ and $\lambda_{sd} = \sqrt{D\tau_{sd}}$, respectively. As we can see, the typical spin-flip time is in fs scale and the exchange time is in sub-ps scale.

2.7 Finmag and Fidimag

Finmag is a finite element micromagnetic simulation package. As with Nmag, Finmag can be called by Python, which is an popular intuitive scripting language. In Finmag, the FEniCS/DOLFIN [71] project is intensively used, which means that all features of FEniCS/dolfin are exposed to users of Finmag. A useful feature of dolfin is that one can describe a finite element variational problem easily in a python script using high-level mathematical description. Therefore, Finmag can be extended easily when users want to model new interactions. Currently, typical micromagnetic interactions such as the exchange, Zeeman, DMI, and demagnetization interactions are implemented in Finmag, and the common dynamical equations such as the LLG equation, the stochastic LLG equation, spin transfer torque as well as nonlocal spin transfer torque are supported in Finmag. The extended equations such as the LLB equation and Baryakhtar equation are also supported in Finmag. C/C++ are used internally where necessary to increase the speed.

Fidimag is a Python based micromagnetic/atomistic spin simulation package. As a scripting language, Python runs through an interpreter and suffers from a performance overhead when compared to lower level languages. Therefore, we make use of C where as necessary and Cython is chosen to link the Python and C. There are two main parts in Fidimag – micromagnetic and atomistic codes. For the micromagnetic part, Fidimag use the finite difference method to discretize the samples. In Fidimag we also make use of existing libraries. For example, the dipolar interactions are sped up by using the fast Fourier transformation techniques from FFTW library; The LLG equation is solved by Sundials/cvode, which is a general differential equation solver package.

Chapter 3

Fidimag

3.1 Introduction

The motivation to develop Fidimag is that we want to make use of the advantages of modern script languages. In Fidimag we choose Python, which is much better suited as a "glue" language. The basic structure of Fidimag is shown in Fig. 3.1. There are two main parts (micromagnetics and atomistic spin model) in Fidimag. Based on standard micromagnetics, common extensions such as temperature effects and spin transfer torques are included as well. As extensions for the atomistic spin model, Langevin

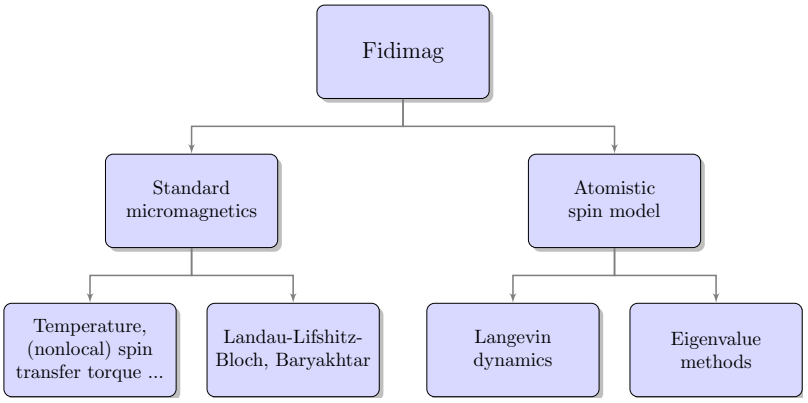

Figure 3.1: The basic structure of Fidimag.

dynamics and an eigenvalue method are implemented. The underlying code is written in C and Cython is used to expose it to Python. In Fidimag, we have used the FFTW library to speed up the calculation of dipolar interactions and the Cvode from Sundials library to solve the LLG equation. Cvode is a solver for stiff and nonstiff ordinary differential equation (ODE) systems.

3.2 Fast Summation of Dipolar interactions

In the micromagnetic part of Fidimag we use the finite difference method (FDM) rather than the finite element method (FEM) to discretize the sample. An advantage to use FDM is that, the demagnetizing field can be computed with the help of fast Fourier transformation (FFT) techniques, the complexity is scaled with $O(N \log N)$ since the main cost is FFT itself which can be achieved within $O(N \log N)$ operations [72]. This is very useful since in both the atomistic spin and micromagnetic models, the long-range dipolar interactions are the most time-consuming part among the various interactions.

There are two methods to compute the effective field in numerical micromagnetics [72]: energy-based and field-based approaches. In Fidimag we use the energy-based approach. A cuboidal volume element with edge length Δx, Δy and Δz is employed to discretize the demagnetization energy (3.1) directly

$$\begin{aligned} E_{\text{demag}} &\approx -\frac{\mu_0}{2} \sum_i |V_i| \mathbf{M}(\mathbf{r}_i) \cdot \mathbf{H}_{\text{d,i}} \\ &\approx \frac{\mu_0}{2} \sum_{i,j} |V_i| \mathbf{M}(\mathbf{r}_i) \cdot \mathcal{N}(\mathbf{r}_i, \mathbf{r}_j) \cdot \mathbf{M}(\mathbf{r}_j), \end{aligned} \tag{3.1}$$

where $|V_i| = \Delta x \Delta y \Delta z$ and $N(\mathbf{r}_i, \mathbf{r}_j)$, the demagnetization tensor, is a 3×3 matrix [72]. The computation details can be found in Newell's original paper [73]. The demagnetization tensor has symmetry properties and only related to the distance between $\mathbf{r}_i$ and $\mathbf{r}_j$

$$\mathcal{N}(i, j) = \mathcal{N}(\mathbf{r}_i - \mathbf{r}_j) = \mathcal{N}(\mathbf{r}_i, \mathbf{r}_j). \tag{3.2}$$

As a result, one arrives at a discrete convolution for the demagnetizing field

$$\mathbf{H}_{\text{d},i} = -\sum_j \mathcal{N}_{i-j} \mathbf{M}_j, \tag{3.3}$$

which is a cell-average field. Note that in this manner the magnetization is defined in the center of each cell. For a simple cubic lattice in the atomistic spin model, the dipolar interaction can be sped up using FFT techniques. The dipolar field [Eq. (2.26)] can be rewritten as,

$$\mathbf{H}_{\text{d},i} = -\sum_j \mathcal{N}^d_{i-j} \mathbf{m}_j, \tag{3.4}$$

where $\mathcal{N}^d_{i-j} = \mathcal{N}^d(\mathbf{r}_i - \mathbf{r}_j)$ and

$$\mathcal{N}^d(\mathbf{r}) = -\frac{3\mu_0\mu_s}{4\pi r^5} \begin{bmatrix} x^2 - r^2/3 & xy & xz \\ xy & y^2 - r^2/3 & yz \\ xz & yz & z^2 - r^2/3 \end{bmatrix}. \tag{3.5}$$

3.2.1 Fast Summation

As we can see, both cases [Eqs. (3.3) and (3.4)] lead to a summation problem. In a more general case, the summation problem for N_s source particles and N_t target particles is

$$f(x_j) = \sum_{k=0}^{N_s-1} \alpha_k \mathcal{K}(x_j - x_k) \qquad j = 0, \ldots, N_t - 1, \tag{3.6}$$

where $\mathcal{K}$ is a smooth symmetric function. In our case, α represents the magnetization components and $\mathcal{K}$ is one entry of the demagnetization tensor $\mathcal{N}$. The definitions of the discrete Fourier transform and inverse Fourier transform are

$$X_k = \sum_{n=0}^{N-1} x_n \omega_N^{nk}, \qquad x_n = \frac{1}{N} \sum_{k=0}^{N-1} X_k \omega_N^{-nk}, \tag{3.7}$$

where $\omega_N = e^{-2\pi i/N}$. Apply the transformations to the kernel function $\mathcal{K}$, we obtain

$$\mathcal{K}(x_k) = \frac{1}{L} \sum_{n=0}^{L-1} b_n \omega_L^{-nk}, \qquad b_n = \sum_{k=0}^{L-1} \mathcal{K}(x_k) \omega_L^{nk}, \tag{3.8}$$

where $L = N_s + N_t - 1$ is the total range number that $x_j - x_k$ spans. Substitute Eq. (3.8) into Eq. (3.6), the summation can be rewritten as

$$\begin{aligned} f(x_j) &= \sum_{k=0}^{N_s-1} \alpha_k \mathcal{K}(x_j - x_k) = \sum_{k=0}^{N_s-1} \alpha_k \frac{1}{L} \sum_{n=0}^{L-1} b_n \omega_L^{-n(j-k)} \\ &= \frac{1}{L} \sum_{n=0}^{L-1} b_n \left(\sum_{k=0}^{N_s-1} \alpha_k \omega_L^{nk} \right) \omega_L^{-nj}. \end{aligned} \tag{3.9}$$

If we extend the length of the sequence $\{\alpha_k\}$ to L by padding zeros, the sum in the inner bracket can be computed by the FFT algorithm, followed with an inverse FFT operation for the remainder. This is the basic principle behind using the FFT method to compute the summation [Eq. (3.6)] rapidly.

3.2.2 Dipolar interaction in triangular lattice

Triangular lattices are also very common in the classical spin model [74, 75]. For example, a skyrmion lattice could be formed on a triangular lattice antiferromagnet [74]. Figure 3.2 shows a 2D triangular lattice using black dots. In this situation, we can still use the FFT techniques to compute the dipolar interactions between magnetic moments. To do this we create a rectangular mesh based on the original triangular lattice. The rectangular mesh is shown in Fig. 3.2 with dashed lines and the white nodes represent the magnetic moments with $|\mathbf{m}| = 0$. The cost of using this method is that we have extended the size of the system from N to $2N$.

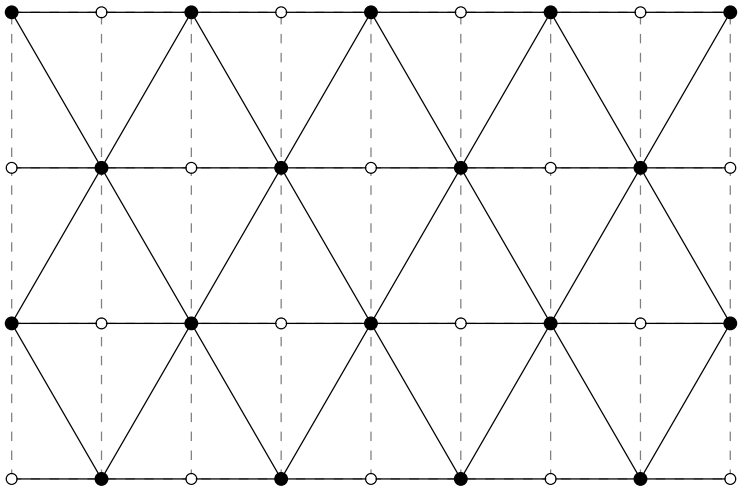

Figure 3.2: A rectangular mesh is created based on the triangular lattice, which is represented by black points.

3.3 Landau-Lifshitz-Baryakhtar equation

In Chapter 4, the Landau-Lifshitz-Baryakhtar (LLBar) equation will be discussed in more detail. Here we briefly show the equations that have been implemented in Fidimag. The implemented LLBar equation is

$$\frac{\partial \mathbf{M}}{\partial t} = -\gamma \mathbf{M} \times \mathbf{H}_e + \lambda_r \mathbf{H}_e - \lambda_e \nabla^2 \mathbf{H}_e, \tag{3.10}$$

where λ_r and λ_e are two damping constants. The effective field $\mathbf{H}_e$ is given by

$$\mathbf{H}_e = -\frac{1}{\mu_0}\frac{\delta w}{\delta \mathbf{M}} = \mathbf{H}_{\text{eff}} + \frac{1}{2\chi}(1 - n^2)\mathbf{M}, \tag{3.11}$$

where $\mathbf{H}_{\text{eff}}$ is the effective field in standard micromagnetics, χ is the longitudinal magnetic susceptibility and $\mathbf{n} = \mathbf{M}/M_e$ with M_e the equilibrium magnitude of the magnetization vector $\mathbf{M}$. In the limit of $\chi \to 0$, the LLBar equation (3.10) reduced to

$$\frac{\partial \mathbf{m}}{\partial t} = -\gamma \mathbf{m} \times \mathbf{H}_{\text{eff}} - \gamma \mathbf{m} \times (\mathbf{m} \times \mathbf{H}^{\text{B}}_{\text{eff}}), \tag{3.12}$$

where

$$\mathbf{H}^{\text{B}}_{\text{eff}} = \alpha \mathbf{H}_{\text{eff}} - \sigma \nabla^2 \mathbf{H}^{\perp}_{\text{eff}}, \tag{3.13}$$

and $\mathbf{H}^{\perp}_{\text{eff}}$ is the transverse component of the effective field, i.e., $\mathbf{H}^{\perp}_{\text{eff}} = \mathbf{H}_{\text{eff}} - (\mathbf{m} \cdot \mathbf{H}_{\text{eff}})\mathbf{m}$. The parameter $\alpha = \gamma M_e \lambda_r$ is the Gilbert damping and $\sigma = \gamma M_e \lambda_e$. The simplified LLBar (sLLBar) equation (3.12) also has been implemented in Fidimag.

3.4 Eigenvalue Method

An effective method to compute the natural frequencies and the normal oscillation of a magnetic system is the so called eigenvalue method [76]. Traditionally, the resonance frequencies of the magnetic system can be extracted from the standard micromagnetic/atomistic simulations by running the dynamics for a certain time. Compared with the traditional one, in eigenvalue method the dynamics is not needed [76]. In Fidimag, we implemented a simple version of the eigenvalue method for the atomistic model [77]. We start from the Hamiltonian

$$\mathcal{H} = \mathcal{H}_{\text{ex}} + \mathcal{H}_{\text{dmi}} + \mathcal{H}_{\text{an}} + \mathcal{H}_{\text{a}}, \tag{3.14}$$

where we have considered the exchange interaction, DMI, anisotropies and static external fields. For a given ground state or metastable spin configuration

$$\mathbf{m}_0 = (\sin\theta\cos\phi, \sin\theta\sin\phi, \cos\theta)^T, \tag{3.15}$$

one can construct a local coordinate system such that

$$\mathbf{m} = w\mathbf{m}_0 + u\mathbf{e}_\theta + v\mathbf{e}_\phi, \tag{3.16}$$

where $\mathbf{e}_\theta = (\cos\theta\cos\phi, \cos\theta\sin\phi, -\sin\theta)^T$ and $\mathbf{e}_\phi = (-\sin\phi, \cos\phi, 0)^T$. In matrix form, Eq. (3.16) can be written as

$$\begin{bmatrix} m_x \\ m_y \\ m_z \end{bmatrix} = \begin{bmatrix} \cos\phi\cos\theta & -\sin\phi & \sin\theta\cos\phi \\ \sin\phi\cos\theta & \cos\phi & \sin\theta\sin\phi \\ -\sin\theta & 0 & \cos\theta \end{bmatrix} \begin{bmatrix} u \\ v \\ w \end{bmatrix}. \tag{3.17}$$

Under this transformation, the unperturbed spin configuration $\mathbf{m}_0$ corresponds to $u = 0, v = 0$ and $w = 1$. In this local coordinate, the effective fields are given by

$$\mathbf{H}_{\text{eff}} = -\frac{1}{\mu_s}\frac{\partial\mathcal{H}}{\partial\mathbf{m}} = -\frac{1}{\mu_s}\left(\frac{\partial\mathcal{H}}{\partial w}\mathbf{m}_0 + \frac{\partial\mathcal{H}}{\partial u}\mathbf{e}_\theta + \frac{\partial\mathcal{H}}{\partial v}\mathbf{e}_\phi\right). \tag{3.18}$$

Substituting Eqs. (3.16) and (3.18) into the LLG equation, we obtain

$$\begin{aligned} \dot{u} &= -\gamma(-wH_v + vH_w) + \alpha(-w\dot{v} + v\dot{w}), \\ \dot{v} &= -\gamma(wH_u - uH_w) + \alpha(w\dot{u} - u\dot{w}), \end{aligned} \tag{3.19}$$

where H_w, H_u and H_v are effective fields along $\mathbf{m}_0$, $\mathbf{e}_\theta$ and $\mathbf{e}_\phi$, respectively. To linearize the LLG equation, we assume $|u| \ll 1$, $|v| \ll 1$ and thus $w \approx 1 - (1/2)(u^2 + v^2)$. Moreover, we look for the solutions such that $u = \tilde{u}e^{-i\omega t}$ and $v = \tilde{v}e^{-i\omega t}$. Therefore, we

arrive at

$$\begin{aligned} -i\omega\mu_s(1+\alpha^2)\tilde{u} &= \gamma(\tilde{h}_v - \tilde{v}\tilde{H}_w) + \alpha\gamma(\tilde{h}_u - \tilde{u}\tilde{H}_w), \\ -i\omega\mu_s(1+\alpha^2)\tilde{v} &= \alpha\gamma(\tilde{h}_v - \tilde{v}\tilde{H}_w) - \gamma(\tilde{h}_u - \tilde{u}\tilde{H}_w), \end{aligned} \tag{3.20}$$

where we have ignored the higher-order terms. In addition, Eq. (3.20) can be rewritten in a matrix form [77]

$$(1+\alpha^2)\frac{i\omega\mu_s}{\gamma}\begin{bmatrix}\mathbf{u}\\ \mathbf{v}\end{bmatrix} = \mathbf{A}\begin{bmatrix}\mathbf{u}\\ \mathbf{v}\end{bmatrix}, \tag{3.21}$$

where we have introduced two vectors $\mathbf{u} = (\tilde{u}_1, \tilde{u}_2, ..., \tilde{u}_n)^T$ and $\mathbf{v} = (\tilde{v}_1, \tilde{v}_2, ..., \tilde{v}_n)^T$. Therefore, the normal modes of the system can be obtained through solving the eigenvalues of the matrix $\mathbf{A}$. For $\alpha = 0$ case, the eigenvalues are pure imaginary numbers since ω is real. The related effective fields are given by

$$\tilde{H}_w = -(\partial\mathcal{H}^{(0)}/\partial w)\big|_{w=1} \tag{3.22}$$

$$\tilde{h}_u = -(\partial\mathcal{H}^{(2)}/\partial u)\big|_{w=1,u=\tilde{u},v=\tilde{v}} \tag{3.23}$$

$$\tilde{h}_v = -(\partial\mathcal{H}^{(2)}/\partial v)\big|_{w=1,u=\tilde{u},v=\tilde{v}}. \tag{3.24}$$

For exchange interaction [Eq. (2.12)], one has

$$\begin{aligned} \tilde{H}^{\text{ex}}_{w,i} &= J\textstyle\sum_j \left[\cos\theta_i\cos\theta_j + \sin\theta_i\sin\theta_j\cos(\phi_i-\phi_j)\right], \\ \tilde{h}^{\text{ex}}_{u,i} &= J\textstyle\sum_j \left[\tilde{u}_j\cos(\phi_i-\phi_j)\cos\theta_i\cos\theta_j + \tilde{u}_j\sin\theta_i\sin\theta_j + \tilde{v}_j\cos\theta_i\sin(\phi_i-\phi_j)\right], \\ \tilde{h}^{\text{an}}_{v,i} &= J\textstyle\sum_j \left[-\tilde{u}_j\cos\theta_j\sin(\phi_i-\phi_j) + \tilde{v}_j\cos(\phi_i-\phi_j)\right]. \end{aligned} \tag{3.25}$$

For bulk DMI [Eq. (2.23)] with $\mathbf{D}_{ij} = D\hat{\mathbf{r}}_{ij}$, we obtain

$$\begin{aligned} \tilde{H}^{\text{dmi}}_{w,i} =& \textstyle\sum_{j\in X} D_{ij}\left(\sin\theta_j\sin\phi_j\cos\theta_i - \sin\theta_i\sin\phi_i\cos\theta_j\right) + \\ & \textstyle\sum_{j\in Y} D_{ij}\left(\sin\theta_i\cos\phi_i\cos\theta_j - \sin\theta_j\cos\phi_j\cos\theta_i\right) + \\ & \textstyle\sum_{j\in Z} D_{ij}\left[\sin\theta_i\sin\theta_j\sin(\phi_i-\phi_j)\right], \end{aligned} \tag{3.26}$$

where $D_{ij} = D\text{sgn}(j-i)$ with $\text{sgn}(x)$ the sign function. The sets X, Y and Z represent the neighbours of site i in x-, y- and z-axis. Meanwhile, $\tilde{h}^{\text{dmi}}_{u,i}$ and $\tilde{h}^{\text{dmi}}_{v,i}$ are given by

$$\begin{aligned} \tilde{h}^{\text{dmi}}_{u,i} =& \textstyle\sum_{j\in X} D_{ij}\left(\tilde{u}_j\sin\theta_j\sin\phi_i\cos\theta_i - \tilde{u}_j\sin\theta_i\sin\phi_j\cos\theta_j - \tilde{v}_j\sin\theta_i\cos\phi_j\right) + \\ & \textstyle\sum_{j\in Y} D_{ij}\left(\tilde{u}_j\sin\theta_i\cos\phi_j\cos\theta_j - \tilde{u}_j\sin\theta_j\cos\phi_i\cos\theta_i - \tilde{v}_j\sin\theta_i\sin\phi_j\right) + \\ & \textstyle\sum_{j\in Z} D_{ij}\cos\theta_i\left[\tilde{u}_j\cos\theta_j\sin(\phi_i-\phi_j) - \tilde{v}_j\cos(\phi_i-\phi_j)\right], \\ \tilde{h}^{\text{dmi}}_{v,i} =& \textstyle\sum_{j\in X} D_{ij}\tilde{u}_j\sin\theta_j\cos\phi_i + \sum_{j\in Y} D_{ij}\tilde{v}_j\sin\theta_j\sin\phi_i + \\ & \textstyle\sum_{j\in Z} D_{ij}\left[\tilde{u}_j\cos\theta_j\cos(\phi_i-\phi_j) + \tilde{v}_j\sin(\phi_i-\phi_j)\right]. \end{aligned} \tag{3.27}$$

For a static external field $\mathbf{H} = (H_x, H_y, H_z)$, the corresponding fields are $\tilde{h}_u = \tilde{h}_v = 0$ and $\tilde{H}^a_{w,i} = H_z \cos\theta_i + H_x \cos\phi_i \sin\theta_i + H_y \sin\phi_i \sin\theta_i$. For anisotropies with $\mathcal{H}_{\text{an}} = -\sum_i (K_x m^2_{x,i} + K_z m^2_{z,i})$, these fields are given by

$$\begin{aligned}
\tilde{H}^{\text{an}}_{w,i} &= 2K_x \cos^2\phi_i \sin^2\theta_i + 2K_z \cos^2\theta_i, \\
\tilde{h}^{\text{an}}_{u,i} &= 2K_x \cos\phi_i \cos\theta_i (\tilde{u}_i \cos\phi_i \cos\theta_i - \tilde{v}_i \sin\phi_i) + 2K_z \tilde{u}_i \sin^2\theta_i, \\
\tilde{h}^{\text{an}}_{v,i} &= 2K_x \sin\phi_i (-\tilde{u}_i \cos\phi_i \cos\theta_i + \tilde{v}_i \sin\phi_i).
\end{aligned} \tag{3.28}$$

3.5 Verification I

3.5.1 A magnetic moment under an external magnetic field

It is always useful to compare the simulation results with the analytical results. The simplest case is the precession motion of a magnetic moment under an external magnetic field. Assuming the external field is along with the z-axis and the initial state is $\mathbf{m}_0 = (1, 0, 0)$, then we have

$$\begin{aligned}
m_x(t) &= \cos(\tilde{\gamma} H_z t) / \cosh(\alpha \tilde{\gamma} H_z t), \\
m_y(t) &= \sin(\tilde{\gamma} H_z t) / \cosh(\alpha \tilde{\gamma} H_z t), \\
m_z(t) &= \tanh(\alpha \tilde{\gamma} H_z t),
\end{aligned} \tag{3.29}$$

where $\tilde{\gamma} = \gamma/(1+\alpha^2)$. Figure 3.3 shows the precessional motion of the macrospin under an external magnetic field with strength $H_z = 1 \times 10^5$ A/m. As expected, the macrospin ends at $M = (0, 0, 1)$ after dissipating its energy and aligning with the field.

3.5.2 Domain-wall motion under charge currents

For the domain-wall case, to date only few exact spatiotemporal solutions of the LLG equation have been reported in the literature. One example is the well known Walker solution [78], another example is that a domain wall moves in an external field with arbitrary time dependence [79]. In this example, we will show an exact spatiotemporal solution with spin transfer torque (Zhang-Li extension). We start from the LLG equation in the spherical form [Eq. (2.78)]

$$\begin{aligned}
\dot{\theta} + \alpha \sin\theta \dot{\phi} &= \gamma H_\phi + u\theta' - u\beta \sin\theta \phi', \\
\alpha\dot{\theta} - \sin\theta \dot{\phi} &= \gamma H_\theta + u\beta\theta' - u \sin\theta \phi'.
\end{aligned} \tag{3.30}$$

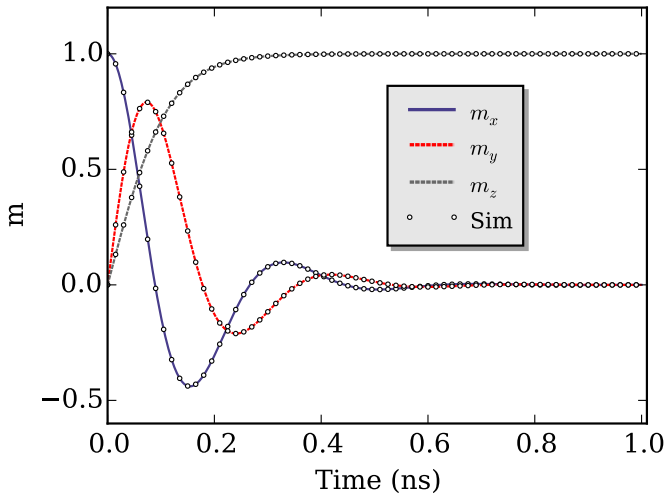

Figure 3.3: The precession motion of a magnetic moment under an external field with $H_z = 1 \times 10^5$ A/m. The macrospin starts with $(1, 0, 0)$ and ends with $(0, 0, 1)$. The parameters used are damping constant $\alpha = 0.5$ and gyromagnetic ratio $\gamma = 2.21 \times 10^5$ m/(A·s).

We consider a 1D system with exchange and anisotropy interactions, so the energy density of the system is given by

$$w = \frac{1}{2}\mu_0 M_s \Big[\tilde{A}(\theta'^2 + \sin^2\theta\phi'^2) + \tilde{K}\sin^2\theta\Big]. \tag{3.31}$$

Note that compared with the standard exchange constant A and anisotropy K, we have $A = (1/2)\mu_0 M_s \tilde{A}$ and $K = (1/2)\mu_0 M_s \tilde{K}$. The effective fields H_θ and H_ϕ read

$$\begin{aligned} H_\theta &= \tilde{A}\theta'' - \sin\theta\cos\theta(\tilde{A}\phi'^2 + \tilde{K}), \\ H_\phi &= 2\tilde{A}\theta'\phi'\cos\theta + \tilde{A}\phi''\sin\theta. \end{aligned} \tag{3.32}$$

We now look for a domain-wall solution with the form

$$\theta_*(z,t) = \theta_0(z - z_*(t)), \qquad \phi_*(z,t) = \phi_*(t), \tag{3.33}$$

where

$$\theta_0(z) = 2\arctan\exp(-z/\Delta), \qquad \Delta = (\tilde{A}/\tilde{K})^{1/2} = \sqrt{A/K} \tag{3.34}$$

describes a head-to-head domain wall. Note that $\theta_0' = \sin\theta_0/\Delta$, we have $\theta_*' = \theta_0' = \sin\theta_0/\Delta$, $\dot{\theta}_* = -\dot{z_*}\theta_0'$, and thus we obtain

$$\begin{aligned} -\dot{z_*} + \alpha\Delta\dot{\phi} &= u, \\ \alpha\dot{z_*} + \Delta\dot{\phi} &= -u\beta. \end{aligned} \tag{3.35}$$

The final solution is

$$\dot{\phi} = \frac{(\alpha - \beta)u(t)}{(1+\alpha^2)\Delta}, \qquad \dot{z}_* = -\frac{(1+\alpha\beta)u(t)}{(1+\alpha^2)}. \tag{3.36}$$

We add some remarks here. Firstly, the result is an exact solution for the Zhang-Li extension to the LLG equation, and because it's an exact solution we can confirm that the domain-wall mass exactly equals zero. Secondly, we haven't assumed the form of charge current u, so it could be an arbitrary function $u = u(t)$. And finally, this solution also holds in the presence of bulk DMI and/or external fields.

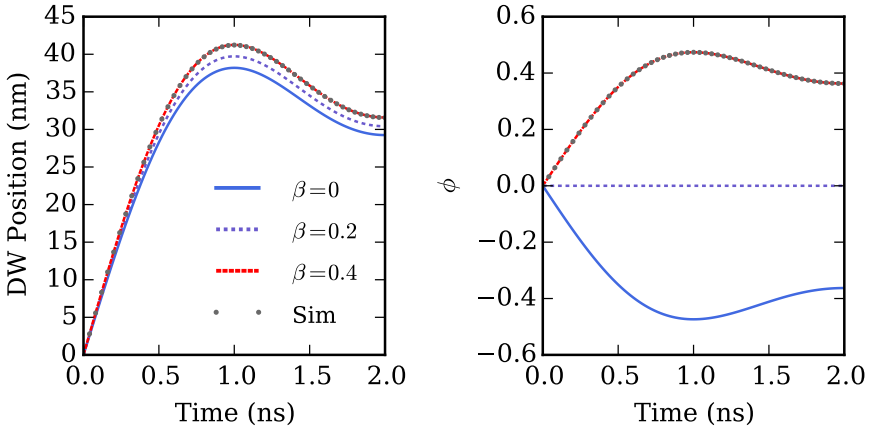

Figure 3.4: A comparison between the simulation and the analytical solution [Eq. (3.36)] for the motion of a head-to-head domain wall.

To compare with the analytical result [Eq. (3.36)], we apply a time-dependent charge current with the form $u(t) = u_0 \sin(\omega_0 t)/(\omega_0 t)$ to the system, where $\omega_0 = \pi \times 10^9$ is selected in the simulation. We make use of the parameters of Permalloy: the saturation magnetization $M_s = 8.6 \times 10^5\,\mathrm{A/m}$, the exchange constant $A = 1.3 \times 10^{-12}\,\mathrm{J/m}$ and an effective anisotropy $K = 5 \times 10^4\,\mathrm{J/m^3}$. In the simulation we fix the damping constant $\alpha = 0.2$ and vary β. Figure 3.4 shows the comparison between the simulation results and the analytical equation (3.36). It is shown that both the domain-wall position and the domain-wall tile angle ϕ agree with the simulation results very well.

In the presence of easy plane anisotropy, the total energy density of the system becomes

$$w = \frac{1}{2}\mu_0 M_s \left[\tilde{A}(\theta'^2 + \sin^2\theta\phi'^2) + \tilde{K}\sin^2\theta + \tilde{K}_\perp \sin^2\theta\sin^2\phi - 2H\cos\theta\right], \tag{3.37}$$

where we have assumed the easy plane anisotropy is in the xz-plane. The effective fields are thus given by

$$H_\theta = \tilde{A}\theta'' - \sin\theta\cos\theta(\tilde{A}\phi'^2 + \tilde{K} + \tilde{K}_\perp \sin^2\phi) - H\sin\theta, \tag{3.38}$$

$$H_\phi = 2\tilde{A}\theta'\phi'\cos\theta + \tilde{A}\phi''\sin\theta - \tilde{K}_\perp \sin\theta\sin 2\phi. \tag{3.39}$$

If we search for a solution with $\phi' = 0$, $\dot{\phi} = 0$ and $\dot{\theta} = -\dot{z}_*\theta'$ (the domain-wall profile is described by $\theta' = \sin\theta/\Delta$), we have

$$\begin{aligned} -\dot{z_*}\theta' &= -\gamma K_\perp \sin\theta\sin 2\phi, \\ -\alpha\dot{z_*}\theta' &= -\gamma H\sin\theta, \end{aligned} \tag{3.40}$$

i.e, $\dot{z}_* = \gamma H\Delta/\alpha$, $\sin 2\phi = H/(\alpha\tilde{K}_\perp)$ and $\Delta = \sqrt{A/(K + K_\perp \sin^2\phi)}$. Therefore, the corresponding solution for the Zhang-Li model is also exact for a constant u.

3.5.3 Magnetic skyrmions

Magnetic skyrmions are topological solitons, which are considered to be topological protected particles [47]. In magnetic systems, several mechanisms can be used to gener-

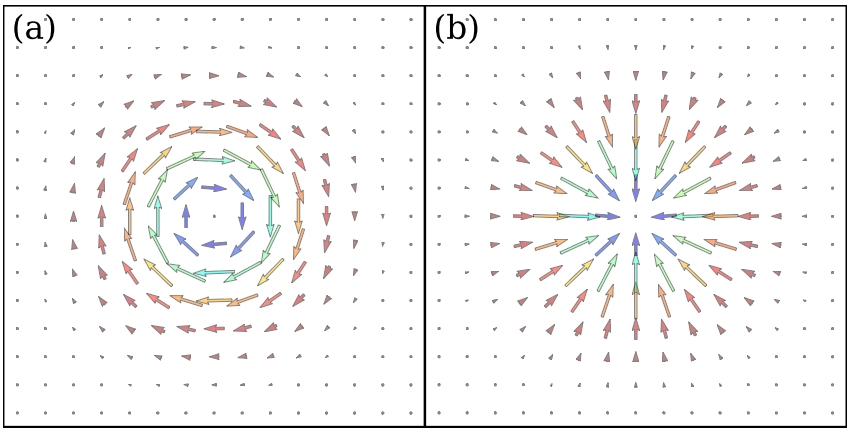

Figure 3.5: (a) A chiral (vortex-like) skyrmion. (b) A hedgehog (radial) skyrmion. The skyrmion number is -1.

ate a skyrmion state. For example, both the long-ranged magnetic dipolar interactions and the Dzyaloshinskii-Moriya interaction (DMI) can lead to skyrmion states. There are two types of DMI, i.e., bulk DMI and interfacial DMI. Figure 3.5(a) shows a vortex-like skyrmion with skyrmion number $q = -1$, where the bulk DMI is used. Meanwhile, a radial skyrmion is shown in Fig. 3.5(b) in which we have used the interfacial DMI.

We consider a 2D system with energy contributions from the exchange interaction, the bulk DMI, an uniaxial anisotropy and a Zeeman field. Therefore, the total micromagnetic energy density is given by

$$w = A(\partial \mathbf{m}/\partial x_\alpha)^2 + D\mathbf{m} \cdot (\nabla \times \mathbf{m}) - Km_z^2 - \mu_0 M_s \mathbf{H} \cdot \mathbf{m}. \tag{3.41}$$

The equilibrium magnetization configurations can be obtained from the Euler-Lagrange equations [80]

$$\frac{\delta w}{\delta \mathbf{m}} = \frac{\partial w}{\partial \mathbf{m}} - \frac{\partial}{\partial x_\alpha} \frac{\partial w}{\partial (\partial \mathbf{m}/\partial x_\alpha)} = 0. \tag{3.42}$$

Since the skyrmion solution is symmetric, we make use the cylindrical coordinates (r, ϕ) and parameterize the magnetization via the spherical angles $(\theta(r), \psi(\phi))$ with

$$\mathbf{m} = (\sin\theta\cos\psi, \sin\theta\sin\psi, \cos\theta), \tag{3.43}$$

that is, $m_r + i m_\varphi = \sin\theta \exp[i(\psi - \phi)]$. Skyrmions are thus can be characterized by the vorticity n_v and the helicity $n_h \pi/2$, and thus we define

$$\psi(\phi) = n_v \phi + n_h \pi/2. \tag{3.44}$$

It can be seen that the DMI energy depends on both the vorticity and the helicity [47]:

$$w_{\text{dmi}} = D\mathbf{m} \cdot (\nabla \times \mathbf{m}) = D \sin[(n_v - 1)\phi + \frac{n_h \pi}{2}] \left[\frac{d\theta}{dr} + \frac{n_v}{2r} \sin 2\theta\right]. \tag{3.45}$$

We look for the solutions with $n_v = 1$ and $n_h = \pm 1$, which results in $w_{\text{dmi}} = n_h D(\theta' + \sin\theta\cos\theta/r)$ where the prime represents the derivative with respect to r. Similarly, the exchange field can be computed by $w_{\text{ex}} = A[(\nabla\theta)^2 + \sin^2\theta(\nabla\psi)^2] = A(\theta'^2 + \sin^2\theta/r^2)$. Here, we consider the external field $\mathbf{H} = H\mathbf{e}_z$. In this situation, the energy density [Eq. (3.41)] is only a function of θ and the Lagrangian density in the cylindrical coordinates is given by

$$\tilde{w} = (w_{\text{ex}} + w_{\text{dmi}} + w_{\text{anis}} + w_{\text{h}})r. \tag{3.46}$$

Therefore, by using the Euler-Lagrange equation (3.42) we obtain

$$\theta'' + \frac{\theta'}{r} - \frac{\sin\theta\cos\theta}{r^2} + d\frac{\sin^2\theta}{r} - \kappa\sin\theta\cos\theta - h\sin\theta = 0, \tag{3.47}$$

where $d = n_h D/A$, $\kappa = K/A$ and $h = \mu_0 M_s H/(2A)$. This differential equation can be solved with standard numerical methods such as the shooting method [62, 81] and the finite difference method. For a magnetic skyrmion with its core pointing-down, the corresponding boundary conditions are

$$\theta(0) = \pi, \qquad \theta(\infty) = 0. \tag{3.48}$$

By making use of the assumption that $\theta' = \sin\theta/r + c(\cos\theta - 1)$, we find that $\theta = 2\text{arccot}\,(cr/2)$ is a solution of Eq. (3.47) if $d = 2c$, $h = c^2$ and $\kappa = -c^2$. Therefore, we obtain the so called Belavin-Polyakov solution [82]

$$\theta = 2\,\text{arccot}\left(\frac{r}{2\xi}\right), \tag{3.49}$$

where $\xi = 2A/D$ is the characteristic length. A Belavin-Polyakov skyrmion is a meta state in the isotropic ferromagnet, in which only the exchange interaction is included [82]. However, here it is a stable solution, and therefore we can use it to validate Fidimag.

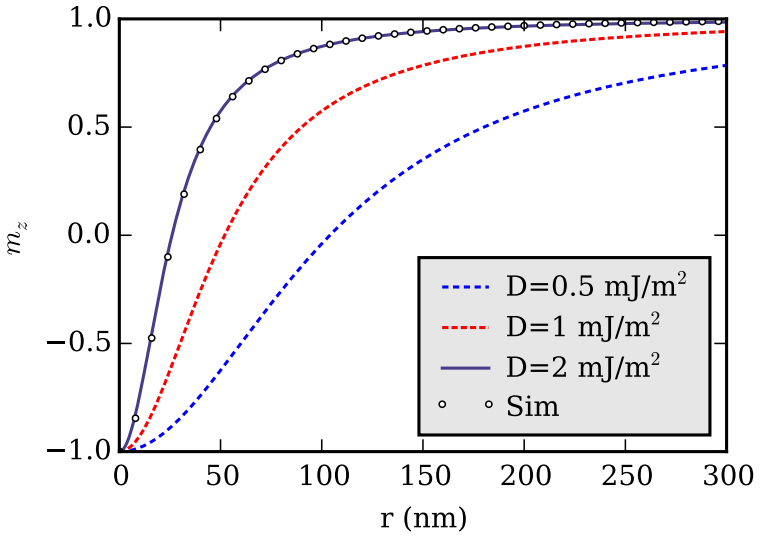

Figure 3.6: A Belavin-Polyakov skyrmion in the presence of easy plane anisotropy and Zeeman field.

Figure 3.6 shows the profiles of Belavin-Polyakov skyrmions for different DMI constants. The used parameters are $M_s = 8.6 \times 10^5\,\text{A/m}$, and $A = 1.3 \times 10^{-12}\,\text{J/m}$. The simulation result is obtained when the easy plane anisotropy ($\kappa < 0$) and external field satisfy $h = c^2$ and $\kappa = -c^2$. The sample size is $1001 \times 1001 \times 2\ \text{nm}^3$ and the cell size is $1 \times 1 \times 2\ \text{nm}^3$. It is found that the simulation results fit the Belavin-Polyakov profile [Eq. (3.49)] well.

3.5.4 Normal modes of a spin chain

We consider a 1D spin chain along the z axis including the exchange interaction, DMI and an anisotropy with its uniaxial axis in z-direction. If the DMI constant D is small, the ground state is uniform, such as $\mathbf{m}_0 = (0, 0, 1)$ or $\mathbf{m}_0 = (0, 0, -1)$. For the former

state, $\phi_i = 0$ and $\theta_i = 0$. Hence, for $\alpha = 0$ Eq. (3.20) reduces to

$$\begin{aligned} -i\omega(\mu_s/\gamma)\tilde{u}_i &= J(\tilde{v}_{i+1} + \tilde{v}_{i-1} - 2\tilde{v}_i) + D(\tilde{u}_{i+1} - \tilde{u}_{i-1}) - 2K\tilde{v}_i, \\ i\omega(\mu_s/\gamma)\tilde{v}_i &= J(\tilde{u}_{i+1} + \tilde{u}_{i-1} - 2\tilde{u}_i) - D(\tilde{v}_{i+1} - \tilde{v}_{i-1}) - 2K\tilde{u}_i, \end{aligned} \tag{3.50}$$

where the total Hamiltonian $\mathcal{H} = \mathcal{H}_{\text{ex}} + \mathcal{H}_{\text{dmi}} + \mathcal{H}_{\text{an}}$ has been used. By introducing a variable $\psi = \tilde{u} - j\tilde{v}$ with $j = \sqrt{-1}$, we arrive at

$$J(\psi_{i+1} + \psi_{i-1} - 2\psi_i) + jD(\psi_{i+1} - \psi_{i-1}) - 2K\psi_i = -\omega(\mu_s/\gamma)\psi_i. \tag{3.51}$$

The first term in Eq. (3.51) is the discrete Laplace operator for ψ. In the long-wave approximation, Eq. (3.51) can be cast into

$$\psi'' + k^2\psi + j\tilde{d}\psi' = 0, \tag{3.52}$$

where $\tilde{d} = 2D/Ja$, $k^2 = (\omega\mu_s/\gamma - 2K)/Ja^2$ and a is the lattice constant. The wavevector k needs to satisfy

$$k^2 = (n\pi/L)^2 - (D/Ja)^2, \tag{3.53}$$

where $L = Na$ is the length of the chain and $n = 0, 1, 2, ...$ are integers. Therefore, we get the frequencies of the normal modes,

$$\frac{\omega\mu_s}{\gamma} = 2K + J\left(\frac{n\pi}{N}\right)^2 - \frac{D^2}{J}. \tag{3.54}$$

Figure 3.7 shows the calculated frequencies for a spin chain using Fidimag, where we have used parameters $J = 1$, $K = 0.01$, $\gamma = 1$, and $\mu_s = 1$. We can find that the Eq. (3.54) agrees with simulation results very well.

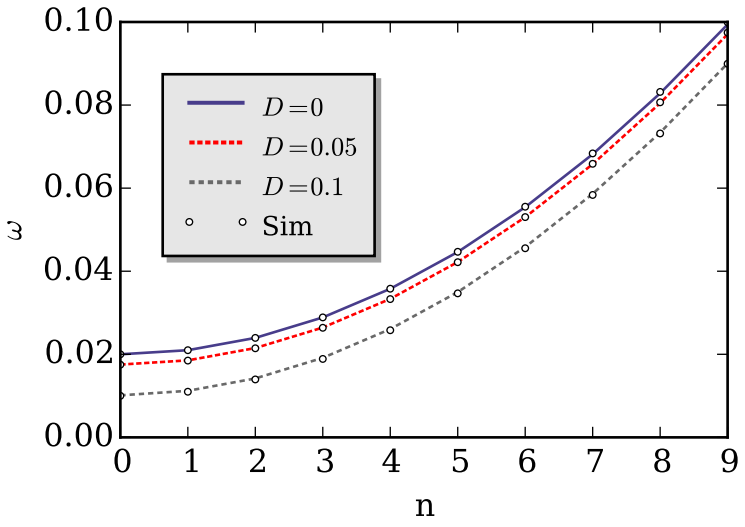

Figure 3.7: The frequencies of the normal modes for a spin chain with DMI.

0	0	0	0
h	0	J_1	0
$\frac{1}{2}h$	$\frac{1}{2}h$	$\frac{1}{2}J_1$	$\frac{1}{2}J_1$

Table 3.1: RK2a.

0	0	0	0
$\frac{2}{3}h$	0	$\frac{2}{3}J_1$	0
$\frac{1}{4}h$	$\frac{3}{4}h$	$\frac{1}{4}J_1$	$\frac{3}{4}J_1$

Table 3.2: RK2b.

0	0	0	0
$\frac{1}{2}h$	0	$\frac{1}{2}J_1$	0
0	h	0	J_1

Table 3.3: RK2c.

3.6 Stochastic LLG equation

For the atomistic spin model, the dynamics in the presence of temperature is governed by the stochastic LLG (SLLG) equation. In micromagnetics the thermal fluctuation effects also can be modeled by the SLLG equation [83, 84]. In this situation, the noise power D is given by

$$D = \frac{\alpha k_B T}{\mu_0 \gamma M_s \Delta V}. \tag{3.55}$$

Note the factor of μ_0; this is because the unit of effective field $\mathbf{H}_{\text{eff}}$ and saturation magnetization M_s is A/m while the unit of γ is m/(A·s). There are many numerical schemes to solve a general stochastic differential equation (SDE) [85–90] and some are developed to solve the SLLG [91, 92]. There are two well-known interpretations for a SDE, i.e., Stratonovich and Itô interpretation which are detailed in Appendix **??**. An s-stage stochastic Runge-Kutta method for an SDE is given by

$$X_i = x_n + \sum_{j=1}^{s} Z_{ij}^0 f(X_j) + \sum_{j=1}^{s} Z_{ij}^1 g(X_j), \quad i = 1, 2, ..., s \tag{3.56}$$

$$x_{n+1} = x_n + \sum_{j=1}^{s} z_{ij}^0 f(X_j) + \sum_{j=1}^{s} z_{ij}^1 g(X_j), \tag{3.57}$$

which can be represented with a table form,

$$\begin{array}{c|c} Z^0 & Z^1 \\ \hline z^0 & z^1 \end{array}. \tag{3.58}$$

In Fidimag, the implemented schemes are Henu scheme (RK2a) [93], Burrage scheme (RK2b) [89], EM1 scheme (RK2c) and EM2 scheme (RK3) [85], as shown in Tables 3.1-3.4. The Henu scheme is the default option in Fidimag.

0	0	0	0	0	0
$(2/3)h$	0	0	$(2/3)J_1$	0	0
$-h$	h	0	$-J_1$	J_1	0
0	$(3/4)h$	$(1/4)h$	0	$(3/4)J_1$	$(1/4)J_1$

Table 3.4: RK3 scheme.

3.7 Verification II

3.7.1 A magnetic moment

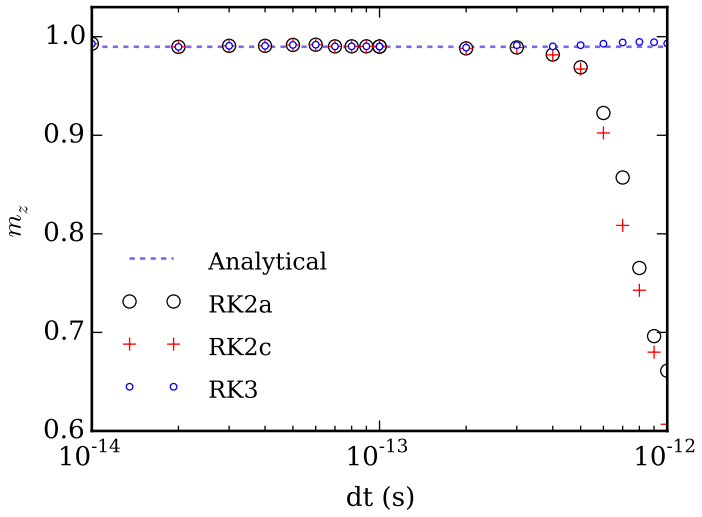

Figure 3.8: Average magnetization of a magnetic moment as a function of time step dt for different integration schemes. Temperature $T = 10$ K.

The size of time step is crucial in solving the SLLG equation. We will compare various integration schemes with different time steps. We consider a single magnetic moment with $\mu_s = M_s V$. In the presence of an uniaxial anisotropy along z-direction, there are two energy minima – pointing-up or pointing-down. The average magnetization in thermal equilibrium is given by [94]

$$\langle m_z \rangle = \frac{\int_0^1 \exp(\chi z^2) z dz}{\int_0^1 \exp(\chi z^2) dz} = \frac{1 - e^{-\chi}}{2\sqrt{\chi} F(\sqrt{\chi})} \tag{3.59}$$

where $\chi = KV/k_B T$ and $F(z)$ is the Dawson integral. Figure 3.8 depicts the average magnetization of the magnetic moment for different integration schemes. It is shown that the RK3 scheme has a larger convergence area. The used parameters are: V=1 nm^3, $M_s = 1281197$ A/m, $K = 6.9 \times 10^6$J/m^3 and damping constant $\alpha = 0.1$. Therefore, the typical time (a period of the precession) is $T \approx 3.2$ ps [94]. From Fig. 3.8 we can find that $dt = 0.1$ ps is a safe choice. In Ref. [94] the authors also give a rule on the discretization time dt, which should be at most 1/30th of the precession time.

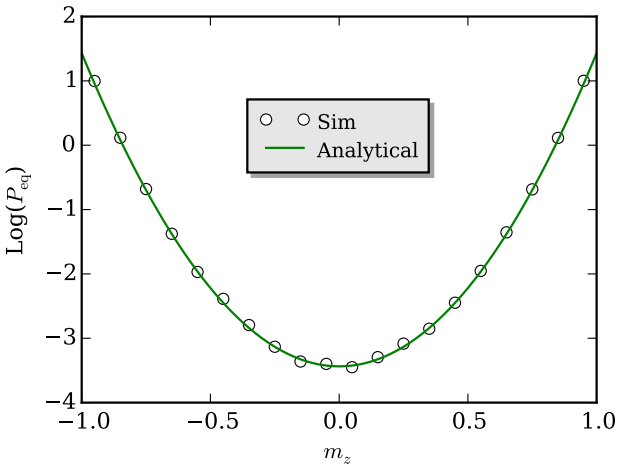

Figure 3.9: The equilibrium probability distribution $P_{\mathrm{eq}}(m_z)$ of a nanoparticle at $T = 300$ K.

3.7.2 Equilibrium distribution of a nanoparticle

As shown in Ref. [95], we consider a nanoparticle with an effective uniaxial anisotropy along z-direction,

$$u = -Km_z^2. \tag{3.60}$$

In the equilibrium state, the probability distribution function (PDF) $P_{\mathrm{eq}}(m_z)$ satisfies

$$P_{\mathrm{eq}}(m_z) \propto \exp(-\chi m_z^2), \tag{3.61}$$

where $\chi = KV/(k_B T)$. And thus, we have

$$P_{\mathrm{eq}}(m_z) = \frac{1}{Z} e^{-\chi m_z^2}, \tag{3.62}$$

where $Z = \int e^{-\chi m_z^2} \, dm_z$ is the partition function. Assume the volume V of the particle is $V = 2.8 \times 10^{-26}$ nm^3, $M_s = 1.42 \times 10^6$ A/m and $K = 7.2 \times 10^5$J/m^3. We obtain $Z = 31.07$ for $T = 300$ K. Figure 3.9 shows the equilibrium probability distribution $P_{\mathrm{eq}}(m_z)$ of a nanoparticle at $T = 300$ K, where the time step $dt = 0.5$ ps and $\alpha = 0.08$ are used in the simulation.

3.7.3 Magnon temperature

We consider a quasi-1D spin chain with exchange interaction and an uniaxial anisotropy

$$\mathcal{H} = -J \sum_{\langle i,j \rangle} \mathbf{m}_i \cdot \mathbf{m}_j - \sum_i K(\mathbf{e}_z \cdot \mathbf{m}_i)^2. \tag{3.63}$$

The typical period related to J is $T = 2\pi\hbar S/J$ which gives $T = 4.14 \times 10^{-12}$s for $S = 1$ and $J = 1$ meV, therefore the time step we have used in simulation is $dt = 5 \times 10^{-14}$s which is less than $T/60$. In the equilibrium state the magnon temperature T_m and the phonon temperature T_p are the same. Figure 3.10 describes the equilibrium

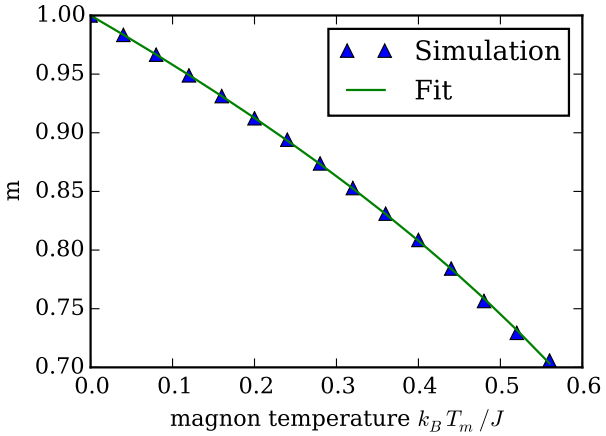

Figure 3.10: Equilibrium magnetization m_0 as a function of the magnon temperature T_m. The system size is $1024 \times 4 \times 4$.

magnetization as a function of the magnon temperature. It can be seen that the magnetization in the equilibrium state decreases as the magnon temperature increases. This behavior can be described by a function,

$$m_0 = (1 - T_m/T_c)^{\beta} \tag{3.64}$$

where T_c is the Curier temperature. The fitted parameters as shown in Fig. 3.10 are $\beta = 0.3683$ and $T_c = 0.91J/k_B$. However, in general both T_c and β are related to the system size.

Chapter 4

Phenomenological description of nonlocal damping

Preface

The work presented in this chapter has been published in [1], in which Prof. Volodymyr V. Kruglyak and Dr. Mykola Dvornik have rewritten the introduction part and some equations.

4.1 Introduction

The Landau-Lifshitz-Gilbert (LLG) equation is a fundamental equation that has been widely used in all areas related to magnetics. This is evidenced by its widespread implementation in various micromagnetic packages based on finite difference or finite element method. [24–26, 96, 97]. Initially, the software for such numerical micromagnetic simulations of magnetization dynamics is based on solving the Landau-Lifshitz equation [66] with a transverse magnetic relaxation term, either in the original (Landau) [66] or “Gilbert" [8] form. Over time, dictated by the experimental and technological needs, the solvers have been modified to include finite temperature effects [65] and additional contributions to the magnetic energy (and therefore to effective magnetic field) [98]. The recent advances in spintronics and magnonics have led to the implementation of various spin-transfer-torque terms [28, 69].

The LLG equation was explained by Thomas Gilbert as the Lagrange equation with a Rayleigh’s dissipation term [8], thus, the second term in the LLG equation is called Gilbert damping term. The Gilbert damping can be determined by ferromagnetic resonance (FMR) experiments. However, some results given by LLG equation are in contradiction with both experimental data and microscopic calculation. For example,

a microscopic calculation gives the dependence of spin-wave damping decrement for short-wave magnons proportional to $\sim k^4$ while the LLG equation shows a dependence proportional to $\sim k^2$, where k is the spin-wave wavevector [37]. Also, there is a deviation between damping parameter α_{FMR} obtained from FMR and α_{DW} calculated from the domain-wall resonance (DWR) for low-damping ferrimagnetic materials [99].

The magnonics of magnetic systems as a fundamental research topic have attracted great attention for its potential application [11, 100, 101]. The decay length of magnons (also called spin waves) is directly related to the damping mechanisms. Different forms of damping have been suggested, for example, a tensor form of magnetization damping was proposed to describe the magnetization relaxation processes of a uniformly magnetized film or particle [39]. In addition, enhanced damping phenomena are observed experimentally [38] and explained as the results of both the interlayer [42] and intralayer [41] spin pumping.

The intrinsic Gilbert damping is generally considered to have a relativistic origin [66, 102]. Indeed, the relativistic corrections to the Hamiltonian between the spin to the electric field leads to the Gilbert damping [102]. The nonlocal damping was predicted for strongly noncollinear magnetizations [40, 103, 104], However, different forms of nonlocal damping are derived using different theories, for example, the diffusion-type term $-\mathbf{m} \times \nabla^2 \partial_t \mathbf{m}$ has been obtained by taking into account the disorder and electron-electron scattering [103] or by expanding the dissipative terms to higher order in spatial derivatives [105], and the tensor form has been proposed by including the role of conduction electrons explicitly in magnetization dynamics [104, 106]. Phenomenologically, the theories operate with the magnetization (i.e. the magnetic moment density) and the effective magnetic field as generalized coordinates and forces respectively [66, 107]. The effective magnetic field is defined in terms of various magnetic material parameters, which are determined by fitting theoretical results to experimental data, and at least in principle, can be calculated using the quantum-mechanical or atomistic methods. A natural question is whether some phenomenological theories give these nonlocal damping terms.

In this chapter, we demonstrate how the phenomenological magnetic relaxation term derived by Baryakhtar to explain the discrepancy between magnetic damping constants obtained from ferromagnetic resonance (FMR) and magnetic domain-wall velocity measurements [108–110] in dielectrics can be applied to magnetic metallic samples. We show that the Landau-Lifshitz equation with the Baryakhtar relaxation term (the Landau-Lifshitz-Baryakhtar or simply LLBar equation) contains the Landau-Lifshitz-Gilbert equation as a special case, while also naturally including the contribution from the nonlocal damping in a tensor form. Here we focus primarily on the manifestations of the Baryakhtar relaxation in problems specific for magnonics [11] and domain-wall dynamics [111, 112]. This is achieved by incorporating the LLBar equation within Fidimag, and by comparing the results of simulations with those from simple analytical

models. Specifically, we demonstrate that the Baryakhtar relaxation leads to increased damping of short wavelength spin waves and to modification of the domain-wall mobility, the latter being also affected by the longitudinal relaxation strength.

This chapter is organized as follows. In Sec. 4.2, we review and interpret the Baryakhtar relaxation term. In Sec. 4.3, we calculate and analyze the spin-wave decay in a thin magnetic nanowire. In Sec. 4.4, we analyze the domain-wall motion driven by the external field and compare the relative strength of contributions from the longitudinal and nonlocal damping. In Sec. 4.5, we extract the damping from dynamic susceptibility. We conclude the discussion in Sec. 4.6.

4.2 Basic equations

In the most general case, the LLBar equation can be written as [108, 113]

$$\frac{\partial \mathbf{M}}{\partial t} = -\gamma \mathbf{M} \times \mathbf{H}_{\text{eff}} + \mathbf{R} \tag{4.1}$$

where $\gamma(>0)$ is the gyromagnetic ratio and the relaxation term $\mathbf{R}$ is

$$\mathbf{R} = \hat{\Lambda}_r \cdot \mathbf{H}_{\text{eff}} - \hat{\Lambda}_{e,sp} \frac{\partial^2 \mathbf{H}_{\text{eff}}}{\partial x_s \partial x_p}. \tag{4.2}$$

Here and in the rest of the chapter, the summation is automatically assumed for repeated indices. The two relaxation tensors $\hat{\Lambda}_r$ and $\hat{\Lambda}_e$ describe relativistic and exchange contributions, respectively, as originally introduced in Ref. [109].

To facilitate comparison with the Landau-Lifshitz-Bloch (LLB) equation as written in Ref. [114], the magnetic interaction energy of the sample is defined as

$$w = w_\mu + \frac{\mu_0}{8\chi} \frac{(M^2 - M_e^2)^2}{M_e^2}, \tag{4.3}$$

where M_e is the equilibrium magnitude of the magnetization vector at a given temperature and zero micromagnetic effective field, i.e. the effective field derived from the micromagnetic energy density w_μ, as used in standard simulations at constant temperature under condition $|\mathbf{M}| = M_e = \text{const}$ (i.e. with only the transverse relaxation included). The second term on the right-hand side of Eq. (4.3) describes the energy density induced by the small deviations of the magnetization length from its equilibrium value M_e at the given temperature, i.e., $|M^2 - M_e^2| \ll M_e^2$, and χ is the longitudinal magnetic susceptibility. Therefore, the associated effective magnetic field is

$$\mathbf{H}_{\text{eff}} = -\frac{1}{\mu_0} \frac{\delta w}{\delta \mathbf{M}} = \mathbf{H}_\mu + \frac{1}{2\chi}(1 - n^2)\mathbf{M} \tag{4.4}$$

where $\mathbf{n} = \mathbf{M}/M_e$, $\mathbf{H}_\mu$ is the effective magnetic field associated with w_μ. Hereafter we assume that our system is in contact with the heat bath, so that the equilibrium temperature and associated values of M_e and χ remain constant irrespective of the magnetization dynamics.

In accordance with the standard practice of both micromagnetic simulations and analytical calculations, to solve LLBar equations (4.1-4.4), one first needs the corresponding static equations obtained by setting the time derivatives to zero and thereby to derive the spatial distribution of the magnetization in terms of both its length and direction. We note that, in general (e.g. as in the case of a domain wall), the resulting distribution of the longitudinal effective field and therefore also of the equilibrium magnetization length is nonuniform, so that the length is not generally equal to M_e. With the static solution at hand, the dynamical problem is solved to find the temporal evolution of the magnetization length and direction following some sort of a perturbation. Crudely speaking, the effect of the relaxation terms is that, at each moment of time, the magnetization direction relaxes towards the instantaneous direction of the effective magnetic field, while the magnetization length relaxes towards the value prescribed by the instantaneous longitudinal effective magnetic field. The effective field itself varies with time, which makes the problem rather complex. However, this is the same kind of complexity as the one that has always been inherent in micromagnetics. One should note that the longitudinal susceptibility has a rather small value at low temperature, so its account is only required at temperatures of the order of the Curie temperature.

We neglect throughout the chapter any effects due to the anisotropy of relaxation, which could be associated with, e.g., the crystalline structure of the magnetic material [108, 113]. This approximation is justified for polycrystalline and amorphous soft magnetic metals, as has been confirmed by simulations presented in Ref. [113]. Hence, we represent the relaxation tensors as $\hat{\Lambda}_r = \lambda_r \hat{I}$ and $\hat{\Lambda}_e = \lambda_e \hat{I}$ where parameters λ_r and λ_e are the relativistic and exchange relaxation damping constants and $\hat{I}$ is the unit tensor. Then, Eq. (4.1) is reduced to

$$\partial_t \mathbf{M} = -\gamma \mathbf{M} \times \mathbf{H}_{\text{eff}} + \lambda_r \mathbf{H}_{\text{eff}} - \lambda_e \nabla^2 \mathbf{H}_{\text{eff}}. \tag{4.5}$$

We separate the equations describing the dynamics and relaxation of the length and direction of the magnetization vector. Representing the latter as a product of its magnitude and directional unit vector $\mathbf{M} = M\mathbf{m}$, we can write

$$M \frac{\partial \mathbf{m}}{\partial t} + \mathbf{m} \frac{\partial M}{\partial t} = -\gamma \mathbf{M} \times \mathbf{H}_{\text{eff}} + \mathbf{R}. \tag{4.6}$$

We multiply this equation by $\mathbf{m}$ to obtain,

$$\frac{\partial M}{\partial t} = \mathbf{m} \cdot \mathbf{R}. \tag{4.7}$$

Then, subtracting the product of Eq. (4.7) and $\mathbf{m}$ from Eq. (4.6), we obtain

$$\frac{\partial \mathbf{m}}{\partial t} = -\gamma \mathbf{m} \times \mathbf{H}_{\text{eff}} + \frac{1}{M}\mathbf{R}_{\perp} \tag{4.8}$$

where $\mathbf{R}_{\perp} = -\mathbf{m} \times (\mathbf{m} \times \mathbf{R})$. In the rest of the paper, we will use $\mathbf{A}_{\perp} \equiv (\mathbf{A})_{\perp} \equiv \mathbf{A} - (\mathbf{A} \cdot \mathbf{m})\mathbf{m}$ to represent the component of the vector $\mathbf{A}$ that is perpendicular (transverse) to vector $\mathbf{m}$. Note that only the perpendicular component of the torque contributes to $\partial_t \mathbf{m} \equiv \partial \mathbf{m}/\partial t$. For given temperature, M_e is constant and we can define $\alpha = \lambda_r/(\gamma M_e)$. In the limiting case of $\chi \to 0$, $M \to M_e$ and thus α is recognized as the Gilbert damping constant from the LLG equation. Let us now consider the case of $\hat{\Lambda}_e \neq 0$. The corresponding contribution to the relaxation term, which we denote here as $\mathbf{B}_{\text{Bar}}$, can be written as

$$\mathbf{B}_{\text{Bar}} = -\lambda_e \nabla^2 \mathbf{H}_{\text{eff}} \equiv -\partial_i \mathbf{j}_i, \tag{4.9}$$

where $\partial_i \equiv \partial/\partial x_i$ and the quantity $\mathbf{j}_i = -\lambda_e \partial_i \mathbf{H}_{\text{eff}}$ has the form of some magnetization current density (magnetization flux).

For the following, it is useful to split the effective field into its perpendicular (relative to $\mathbf{m}$) part ($\mathbf{H}_{\text{eff}}^{\perp}$, "perpendicular field") and parallel part ($\mathbf{H}_{\text{eff}}^{\parallel}$, "parallel field"), i.e., $\mathbf{H}_{\text{eff}} = \mathbf{H}_{\text{eff}}^{\perp} + \mathbf{H}_{\text{eff}}^{\parallel}$, and then to consider the associated magnetic fluxes and torques separately. The magnetic flux of $\mathbf{j}_{\parallel,i} = -\lambda_e \partial_i \mathbf{H}_{\text{eff}}^{\parallel}$ and then the contribution of the associated torque $\boldsymbol{\tau}_{\parallel} = -\partial_i \mathbf{j}_{\parallel,i}$ onto $\mathbf{m}$ is

$$(\boldsymbol{\tau}_{\parallel})_{\perp} = -2\lambda_e \partial_i \mathbf{H}_{\text{eff}}^{\parallel} \partial_i \mathbf{m} - \lambda_e \mathbf{H}_{\text{eff}}^{\parallel} (\nabla^2 \mathbf{m})_{\perp}. \tag{4.10}$$

The perpendicular field can be represented as

$$\mathbf{H}_{\text{eff}}^{\perp} = \frac{1}{\gamma M^2}\left[\mathbf{M} \times \frac{\partial \mathbf{M}}{\partial t}\right] + O(\mathbf{R}) \approx \frac{1}{\gamma}\left[\mathbf{m} \times \partial_t \mathbf{m}\right]. \tag{4.11}$$

So, we can write for the magnetization flux associated with the perpendicular field

$$\mathbf{j}_{\perp,i} = -(\lambda_e/\gamma)\partial_i(\mathbf{m} \times \partial_t \mathbf{m}). \tag{4.12}$$

The right-hand side of Eq. (4.12) is the dissipative spin current [105], which can be interpreted as the dynamically driven spin pumping [105]. For the associated perpendicular torque $\boldsymbol{\tau}_{\perp}$, we obtain,

$$\boldsymbol{\tau}_{\perp} = -\partial_i \mathbf{j}_{\perp,i} = -\sigma M_e \partial_i \partial_i (\mathbf{m} \times \partial_t \mathbf{m}), \tag{4.13}$$

where we have introduced a variable $\sigma = \lambda_e/(\gamma M_e)$. We show that the torque $(\boldsymbol{\tau}_{\perp})_{\perp}$ could be written as (see Appendix A.1 for details)

$$(\boldsymbol{\tau}_{\perp})_{\perp} = M_e\left[\mathbf{m} \times (\mathcal{D} \cdot \partial_t \mathbf{m}) - \sigma \mathbf{m} \times \nabla^2 \partial_t \mathbf{m}\right], \tag{4.14}$$

where $\mathcal{D}$ is a 3×3 tensor [104, 106],

$$\mathcal{D}_{\alpha\beta} = 2\sigma(\mathbf{m} \times \partial_i \mathbf{m})_\alpha (\mathbf{m} \times \partial_i \mathbf{m})_\beta - \sigma(\partial_i \mathbf{m} \cdot \partial_i \mathbf{m})\delta_{\alpha\beta}. \tag{4.15}$$

In the limit of $\chi \to 0$, we assume $\mathbf{H}_{\text{eff}}^{\parallel} = 0$ and therefore obtain

$$\partial_t \mathbf{m} = -\gamma \mathbf{m} \times \mathbf{H}_{\text{eff}} - \gamma\alpha \mathbf{m} \times (\mathbf{m} \times \mathbf{H}_{\text{eff}}) + \mathbf{m} \times (\mathcal{D} \cdot \partial_t \mathbf{m}) - \sigma \mathbf{m} \times \nabla^2 \partial_t \mathbf{m}. \tag{4.16}$$

At the same time, Eq. (4.8) can then be written as

$$\frac{\partial \mathbf{m}}{\partial t} = -\gamma \mathbf{m} \times \mathbf{H}_{\text{eff}} - \gamma \mathbf{m} \times (\mathbf{m} \times \mathbf{H}_{\text{eff}}^{\text{B}}), \tag{4.17}$$

where

$$\mathbf{H}_{\text{eff}}^{\text{B}} = \alpha \mathbf{H}_{\text{eff}} - \sigma \nabla^2 \mathbf{H}_{\text{eff}}^{\perp}, \tag{4.18}$$

and $\mathbf{H}_{\text{eff}}^{\perp}$ is the transverse component of the effective field. The first term in Eq. (4.18) is kept as $\mathbf{H}_{\text{eff}}$ since $\mathbf{m} \times \mathbf{H}_{\text{eff}} = \mathbf{m} \times \mathbf{H}_{\text{eff}}^{\perp}$. In practice, we use the simplified LLBar (sLLBar) equation (4.17) rather than Eq. (4.16) for numerical implementation. As shown in Eq. (4.16) the damping terms contain both the form $-\mathbf{m} \times \nabla^2 \partial_t \mathbf{m}$ [103, 105] and tensor form $\mathbf{m} \times (\mathcal{D} \cdot \partial_t \mathbf{m})$ [106]. Hence, we conclude that the exchange damping can be explained as the nonlocal damping, and Eq. (4.17) is the phenomenological equation to describe the nonlocal damping.

Phenomenologically, the Gilbert damping is local and the damping due to the nonuniform magnetization dynamics being ignored [8]. The exchange relaxation term in the LLBar equation describes the nonlocal damping due to the nonuniform effective field. Despite the complexity of various damping mechanisms, the spin current $\mathbf{j}$ in conducting ferromagnets can be calculated, e.g. using the time-dependent Pauli equation within the s-d model. The spin current is then given by $\mathbf{j}_i = (g\mu_B \hbar G_0 / 4e^2)(\partial_t \mathbf{m} \times \partial_i \mathbf{m})$, where G_0 is the conductivity [106], and thus the nonlocal damping of the tensor form can be obtained [104, 106]. As we can see from Appendix A.1, this spin current densities $\mathbf{j}_i$ and $\mathbf{j}_i^a$ have the same form, and therefore, we can establish that $\sigma \sim g\mu_B \hbar G_0 / 4e^2 M_e$. The spin current component $\mathbf{j}_i^b$ (see Appendix A.1) gives the term $-\mathbf{m} \times \nabla^2 \partial_t \mathbf{m}$ [105], and the value of σ can therefore be interpreted as $\sigma \sim (\gamma / \mu_0 M_e)(\hbar/2)^2 n_e \tau_{\text{sc}} / m^*$, where n_e is the conduction electron density, m^* is the effective mass and τ_{sc} is the transverse spin scattering time [41].

It is of interest to compare Eq. (4.5) with the LLB equation [114], which could be written as

$$\frac{\partial \mathbf{n}}{\partial t} = -\gamma \mathbf{n} \times \mathbf{H}_{\text{eff}} + \frac{\gamma \alpha_{\parallel}}{n^2} [\mathbf{n} \cdot \mathbf{H}_{\text{eff}}] \mathbf{n} - \frac{\gamma \alpha_{\perp}}{n^2} \mathbf{n} \times (\mathbf{n} \times \mathbf{H}_{\text{eff}}), \tag{4.19}$$

where $\mathbf{n} = \mathbf{M}/M_e(T)$ is the reduced magnetization and $M_e(T)$ is the equilibrium magnetization value at temperature T. The effective field $\mathbf{H}_{\text{eff}}$ contains the usual

micromagnetic contributions $\mathbf{H}_{\text{int}}$ as well as the contribution from the temperature,

$$\mathbf{H}_{\text{eff}} = \mathbf{H}_{\text{int}} + \frac{m_e}{2\tilde{\chi}_{\parallel}}(1 - n^2)\mathbf{n}, \tag{4.20}$$

where $m_e = M_e(T)/M_e(0)$ and $\tilde{\chi}_{\parallel} = \partial m/\partial H$ with $m = M/M_e(0)$ [114]. By substituting Eq. (4.20) into Eq. (4.19), one arrives at

$$\frac{\partial \mathbf{n}}{\partial t} = -\gamma \mathbf{n} \times \mathbf{H}_{\text{int}} + \gamma\alpha_{\parallel}(\mathbf{H}_{\text{int}})_{\parallel} + \gamma\alpha_{\perp}(\mathbf{H}_{\text{int}})_{\perp} + \frac{\alpha_{\parallel}\gamma m_e}{2\tilde{\chi}_{\parallel}}(1 - n^2)\mathbf{n}. \tag{4.21}$$

Meanwhile, if we neglect the λ_e term in Eq. (4.5) and insert the effective field equation (4.3) into Eq. (4.5), we obtain

$$\frac{\partial \mathbf{n}}{\partial t} = -\gamma \mathbf{n} \times \mathbf{H}_{\text{int}} + \gamma\lambda_r \mathbf{H}_{\text{int}} + \frac{\lambda_r \gamma}{2\chi}(1 - n^2)\mathbf{n}. \tag{4.22}$$

As we can see, Eq. (4.22) is a special case of the LLB equation with the assumption that $\alpha_{\perp} = \alpha_{\parallel} = \lambda_r/(\gamma M_e)$ and $\chi = M_e(0)\tilde{\chi}_{\parallel}$. However, the LLB equation does not contain the λ_e-term (nonlocal damping term) which is the main focus in this work.

4.3 Spin-wave decay

To perform the micromagnetic simulation for the spin-wave decay, we have implemented the sLLbar equation (4.17) in Fidimag. A new variable β for the exchange damping is introduced with $\sigma = \beta G$, where G is a coefficient to scale β to the same order as α. In practice, G was chosen to be $G = A/(\mu_0 M_e^2)$.

The simulation geometry has dimensions $L_x = 2002\,\text{nm}$, $L_y = 2\,\text{nm}$ and $L_z = 2\,\text{nm}$, and the cell size is $1 \times 2 \times 2\,\text{nm}^3$. The magnetization aligns along the $\mathbf{e}_x$ direction for the equilibrium state and the parameters are typical of Permalloy: the exchange constant $A = 1.3 \times 10^{-11}\,\text{J/m}$, the saturation magnetization $M_e = 8.6 \times 10^5\,\text{A/m}$ and the Gilbert damping damping coefficient $\alpha = 0.01$. The spin waves are excited locally in the region $0 \leq x \leq 2\,\text{nm}$, and to prevent the spin-wave reflection the damping coefficient is increased linearly [115] from 0.01 at $x = 1802\,\text{nm}$ to 0.5 at $x = 2002\,\text{nm}$.

Figure 4.1 illustrates the spin-wave amplitude decay along the rod. The y component of magnetization unit vector m_y data for $30 \leq x \leq 1800$ nm was fitted using (4.23) to extract the wave vector k and the decay constant λ, and good agreement is observed due to the effective absence of spin-wave reflection. We use data after having computed the time development of the magnetization for 4 ns to reach a steady state. The injected spin-wave energy is absorbed efficiently enough within the right 200 nm of the rod due to the increased damping.

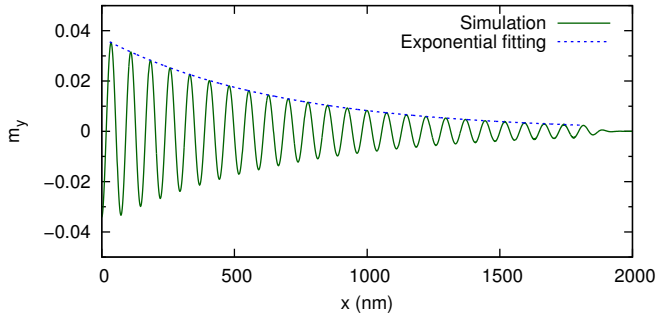

Figure 4.1: The spin-wave amplitude decay along the rod, for a spin wave was excited locally by applying a microwave $\mathbf{H} = H_0 \sin(2\pi f t)\mathbf{e}_y$ of frequency $f = 30\,\mathrm{GHz}$ and amplitude $H_0 = 1000\,\mathrm{Oe}$ in the region $0 \leq x \leq 2\,\mathrm{nm}$. The data were fitted using Eq. (4.23) with $\beta = 0.02$ and $\alpha = 0.01$.

To analyze the simulation data, we exploit the uniform plane-wave assumption with its exponential amplitude decay due to energy dissipation, i.e. magnetization with the form $e^{i(\mathrm{k}x-\omega t)}e^{-\lambda x}$, where λ is the characteristic parameter of the spin-wave damping. For a small-amplitude spin-wave propagation we have [100]

$$\mathbf{m} = \mathbf{e}_\mathrm{x} + \mathbf{m}_0 e^{i(kx-\omega t)}e^{-\lambda x}, \tag{4.23}$$

where $|\mathbf{m}_0| \ll 1$, and the effective field of the long rod can be expressed as

$$\mathbf{H}_\mathrm{eff} = H_s m_x \mathbf{e}_x + D\nabla^2\mathbf{m}, \tag{4.24}$$

where the 'easy axis' anisotropy field $H_s m_x \mathbf{e}_x$ originates from the demagnetizing field, and the constant D measures the strength of the exchange field,

$$H_s = \frac{2K}{\mu_0 M_e} = \frac{1}{2}M_e, \qquad D = \frac{2A}{\mu_0 M_e}. \tag{4.25}$$

To test the spin-wave decay for this system, a sinusoidal field $\mathbf{H} = H_0 \sin(2\pi f t)\mathbf{e}_y$ was applied to the rod in the region $0 \leq x \leq 2\,\mathrm{nm}$ to generate spin waves.

Figure 4.2 shows the product of the spin-wave-decay constant λ and wave vector k as a function of the frequency. The dependence is linear for the $\beta = 0$ case, which is in agreement with the case with the zero adiabatic spin torque [100]. The addition of a nonzero β term leads to a nonlinear relation, and the amplitude of the spin-wave-decay constant that is significantly larger than that given by the linear dependence. We also performed the simulation for the $\chi > 0$ case by using Eq. (4.5) which shows that the β term is the leading factor for this nonlinearity (the relative error is less than 1% for $\chi = 1 \times 10^{-3}$). To analyze the nonlinear dependence, we introduce the complex wave vector $\widetilde{k}$,

$$\widetilde{k} = k + \lambda i. \tag{4.26}$$

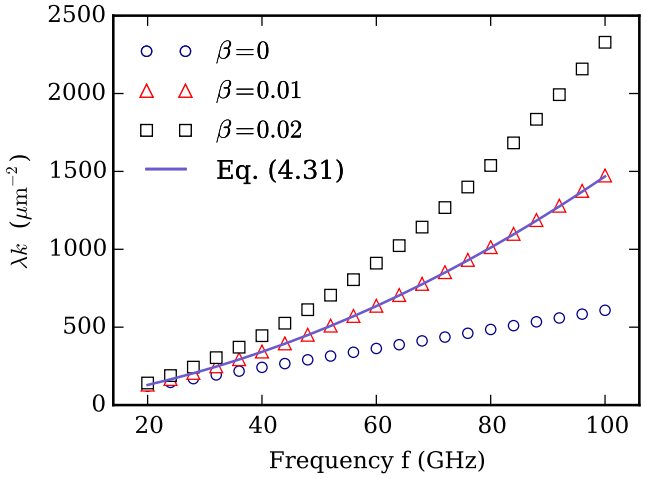

Figure 4.2: The spin-wave decay constant–wave vector product λk as a function of the frequency for different β values. The slateblue line was drawn using Eq. (4.31) for the case $\beta = 0.01$.

By linearizing Eq. (4.17) and setting the determinant of the matrix to zero we obtained (see Appendix A.2 for details):

$$(\omega + \tilde{\omega}_0 + i\tilde{\omega}_1)(\omega - \tilde{\omega}_0 + i\tilde{\omega}_1) = 0, \tag{4.27}$$

where $\tilde{\omega}_0 = \gamma(H_s + D\tilde{k}^2)$ and $\tilde{\omega}_1 = \alpha\tilde{\omega}_0 + \beta G\tilde{k}^2\tilde{\omega}_0$. The second term in Eq. (4.27) is expected to be equal to zero, i.e., $\tilde{\omega}_1 - i\omega + i\tilde{\omega}_0 = 0$. There are two scenarios to consider: the first is the $\beta = 0$ case, in which $k\lambda$ could be extracted by taking the imaginary part of $\tilde{k}^2$ in Eq. (4.26):

$$k\lambda = \frac{1}{2}\,\mathrm{Im}\left\{\tilde{k}^2\right\} = \frac{\alpha\omega}{2(1+\alpha^2)\gamma D}. \tag{4.28}$$

The linear dependence of $k\lambda$ as a function of frequency matches the data plotted in Fig. 4.2. For the $\beta > 0$ case, solving (4.27) directly gives

$$\tilde{k}^2 = -\frac{b}{2a}\left(1 - \sqrt{1 - \frac{4c}{b^2}a}\right), \tag{4.29}$$

where $a = \beta\gamma DG$, $b = (i+\alpha)\gamma D + \beta G\gamma H_s$ and $c = (i+\alpha)\gamma H_s - i\omega$. Taking a Taylor expansion of (4.29) about $a = 0$ yields

$$\tilde{k}^2 \approx -\frac{c}{b} - \frac{c^2}{b^3}a. \tag{4.30}$$

By neglecting the higher order terms such as α^2, $\alpha\beta$ and β^2, we obtained

$$k\lambda \approx \frac{\omega}{2\gamma D}(\alpha + \beta G k^2), \tag{4.31}$$

where the dispersion relation for the rod is $\omega = \gamma(H_s + Dk^2)$. Equation (4.31) shows

there is an extra k^2 term associated with the exchange-damping term in addition to the linear dependence between $k\lambda$ and ω. The slateblue line in Fig. 4.2 is plotted using Eq. (4.31) with $\beta = 0.01$ and $\alpha = 0.01$, which shows a good approximation for the simulation data. This exchange damping could be important in determining the nonadiabatic spin torque. We could establish the value of β using the existing experimental data, for example, the transverse spin current data [41] gives $\beta \sim 0.1$ which hints that the lifetime and propagation length of short-wavelength magnons could be much shorter than those given by the LLG equation [116].

4.4 Domain-wall motion

We implemented the LLBar equation (4.5) in FIDIMAG to study the effect of parallel relaxation process on domain-wall motion. The simulated system for the domain-wall motion is a one-dimensional (1D) mesh with a length of 20000 nm and a discretization size of 4 nm. A head-to-head domain wall is initialized with its center near $x = 500$ nm. In this section, the demagnetizing fields are simplified as $\mathbf{H}_\mathrm{d} = -N\mathbf{M}$ and the demagnetizing factors are chosen to be $N_x = 0$, $N_y = 0.2$ and $N_z = 0.8$, respectively. The domain wall moves under the applied field for 50 ns and the domain-wall velocities at different external field strengths are computed. Figure 4.3 shows the simulation results of domain-wall motion under external fields for different susceptibilities without consideration of exchange damping, i.e., $\beta = 0$. The longitudinal susceptibility is around 10^{-4} at room temperature and increases with the temperature [114]. We find that the longitudinal susceptibilities have no influence on the maximum velocity but change the Walker breakdown field H_w significantly. The domain-wall velocity in the limit $\chi \to 0$ is almost the same as in the case of $\chi = 10^{-4}$, which could be explained by the difference proportional to the ratio of $(\chi/\alpha)^2$ in Eq. (4.54).

To investigate the effect of longitudinal magnetic susceptibility χ and exchange relaxation damping σ on the domain-wall motion, we use the remainder of this section for analytical studies. We start from the constant saturation magnetization of a one-dimensional domain-wall model, such as the 1D head-to-head wall [117]. The static 1D domain-wall profile can be expressed as

$$m_x = -\tanh\left(\frac{x-q}{\Delta}\right), \quad m_t = \operatorname{sech}\left(\frac{x-q}{\Delta}\right) \tag{4.32}$$

where m_t is the perpendicular component of the unit magnetization vector, Δ is the wall width parameter and q is the position of the domain-wall center.

We consider the case in which the system is characterized by two anisotropies, easy uniaxial anisotropy K and hard plane anisotropy $K_\perp$, which originate from demagnetization. The aim is to analyze the impact of the longitudinal magnetic susceptibility

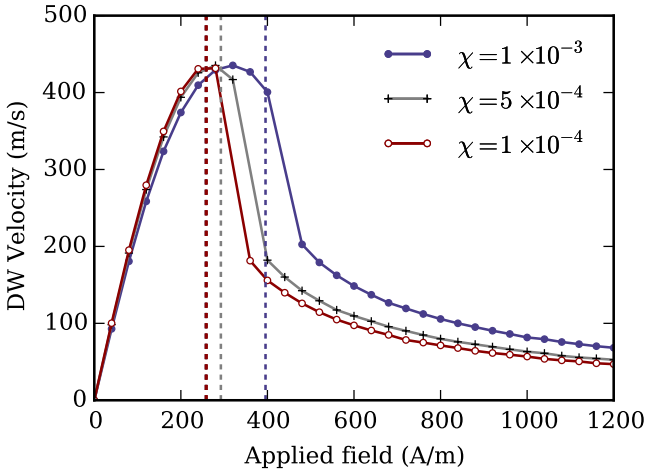

Figure 4.3: Simulations results of domain-wall velocities for various susceptibilities. The parameters used are: $\alpha = 0.001$, $\beta = 0$, $N_y = 0.2$ and $N_z = 0.8$. The vertical dashed lines are the breakdown fields computed using Eq. (4.54).

under the 1D domain-wall model, the demagnetization energy density can be written as

$$E_{\text{an}} = -\frac{K}{M_e^2} M_x^2 + \frac{K_\perp}{M_e^2} M_z^2, \tag{4.33}$$

where $K = (1/2)(N_y - N_x)\mu_0 M_e^2$ and $K_\perp = (1/2)(N_z - N_y)\mu_0 M_e^2$. In the limit case $\chi \to 0$ case, the effective anisotropy energy density E_{an} can be rewritten as

$$E'_{\text{an}} = K \sin^2\theta(1 + \kappa \sin^2\varphi), \tag{4.34}$$

where $\mathbf{m} = (\cos\theta, \sin\theta\cos\varphi, \sin\theta\sin\varphi)$ is used and $\kappa = K_\perp/K$ is the ratio between hard plane anisotropy strength and easy uniaxial anisotropy strength.

The dynamics of the domain wall with the 1D profile can be described using three parameters [118]: the domain-wall width Δ, the domain wall position q and the domain-wall tilt angle ϕ. In this domain-wall model, one can assume that $\varphi(x,t) = \phi(t)$ is only a function of time. Thus, the magnetization profile for the head-to-head domain wall is given by

$$\theta(x,t) = 2\tan^{-1}\exp\left(\frac{x - q(t)}{\Delta(t)}\right), \quad \varphi(x,t) = \phi(t). \tag{4.35}$$

Using the magnetization unit vector to calculate the exchange energy is a good approximation for the case $\chi \ll 1$, thus, the total energy density can be rewritten as

$$E_{\text{tot}} = \frac{\mu_0}{8\chi}\frac{(M^2 - M_e^2)^2}{M_e^2} + M^2 w_\mu(\mathbf{m}), \tag{4.36}$$

where

$$w_\mu(\mathbf{m}) = \frac{A}{M_e^2}(\nabla\mathbf{m})^2 - \frac{K}{M_e^2}m_x^2 + \frac{K_\perp}{M_e^2}m_z^2. \tag{4.37}$$

Within the 1D domain-wall profile, H_{m}, the longitudinal component of the effective field is obtained:

$$H_{\mathrm{m}} = \mathbf{m} \cdot \mathbf{H}_{\mathrm{eff}} = \frac{M}{2\chi M_e^2}(M_e^2 - M^2) - 2MP\sin^2\theta, \tag{4.38}$$

where P is defined as

$$P = \frac{1}{\mu_0 M_e^2}\left[\frac{A}{\Delta^2} + K(1 + \kappa\sin^2\phi)\right]. \tag{4.39}$$

As we can see, P is a function of the tilt angle ϕ and the domain-wall width Δ. At the static state, H_m should equal zero, i.e., $dM/dt = 0$, which gives

$$M^2 = (1 - 4\chi P\sin^2\theta)M_e^2. \tag{4.40}$$

Equation (4.40) shows that the difference between magnetization length M and M_e reaches its maximum at the center of the domain wall due to the effect of the exchange field, which also peaks in the center of the domain wall. According to Eq. (4.40), we can estimate that the magnetization length difference is $\delta M \approx -2\chi P\sin^2\theta$ for the $\chi \ll 1$ case. Figure 4.4 shows the magnetization length differences of a 1D domain wall for various χ, it can be seen that this approximation for δM agrees very well with the simulation results.

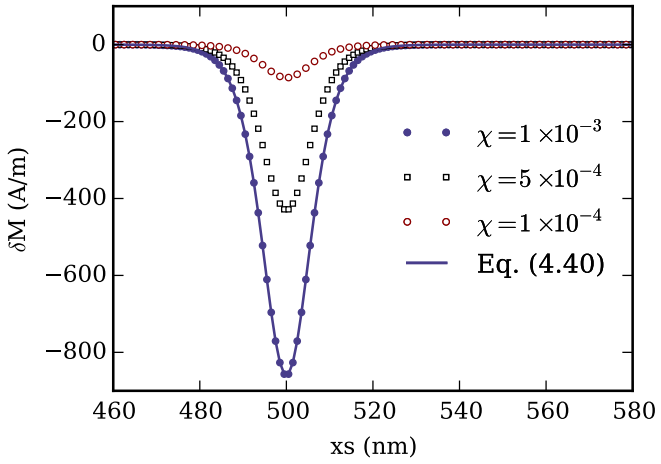

Figure 4.4: Simulation results of the magnetization length difference δM for a 1D domain wall located at $x = 500$ nm with $M_e = 8.6 \times 10^5$ A/m. The demagnetizing factors are selected to be $N_x = 0$ and $N_y = N_z = 0.5$.

In the dynamic case, H_m is not equal to zero. If we wrote Eq. (4.38) as $H_{\mathrm{m}} = FM$, we would find that the nontrivial term that contributes to H_m is

$$F = \frac{1}{2\chi}(1 - M^2/M_e^2) - 2P\sin^2\theta. \tag{4.41}$$

As an approximation for H_{m}, we expect $dF/dt = 0$ [119], which gives

$$H_{\mathrm{m}} = \frac{4P}{\Delta}\frac{\chi}{\alpha}\frac{\dot{q}}{\gamma}m_t^2 m_x. \tag{4.42}$$

In this approximation, we have ignored the terms containing dP/dt and thus the amplitude of H_{m} is influenced by only the domain-wall velocity. We employ the Lagrangian equation combined with dissipation function $\mathcal{F}$ to compute the domain-wall dynamics [111]. The Lagrange equations are

$$\frac{\partial \mathcal{L}}{\partial X} - \frac{d}{dt}\left(\frac{\partial \mathcal{L}}{\partial \dot{X}}\right) + \frac{\partial \mathcal{F}}{\partial \dot{X}} = 0, \tag{4.43}$$

where X refers to q, ϕ and Δ. The dissipation function is defined by $\mathcal{F} = \int F\, dx$ where

$$F = \frac{1}{2}\mu_0 M_e \gamma[\alpha \mathbf{H}_{\mathrm{eff}}^2 + \sigma(\nabla \mathbf{H}_{\mathrm{eff}})^2], \tag{4.44}$$

is the dissipation density function.

4.4.1 Parallel relaxation

We neglect the exchange damping term with assumption that $\sigma \ll \alpha\Delta^2$ and arrive at

$$F = \frac{1}{2}\alpha\mu_0 M_e \gamma \mathbf{H}_{\mathrm{eff}}^2 = \frac{1}{2}\alpha\mu_0 M_e \gamma(\mathbf{H}_{\perp}^2 + \mathbf{H}_m^2), \tag{4.45}$$

where $\mathbf{H}_{\perp}$ and $\mathbf{H}_m$ are the perpendicular and parallel components of the effective field. If we also assume that $\alpha \sim \chi \ll 1$, $\mathbf{H}_{\perp}^2$ can be approximated by Eq. (4.11),

$$\mathbf{H}_{\perp}^2 = \frac{1}{\gamma^2}\dot{\mathbf{m}}^2 = \frac{1}{\gamma^2}(\dot{\theta}^2 + \sin^2\theta\dot{\phi}^2). \tag{4.46}$$

Substituting Eqs. (4.42) and (4.46) into Eq. (4.45) and integrating over space, we obtain

$$\mathcal{F} = \frac{\alpha\mu_0 M_e}{\gamma}\left[\dot{\phi}^2\Delta + \frac{\dot{q}^2}{\Delta}(1+Q)\right], \tag{4.47}$$

where we have ignored the $\dot{\Delta}$ term. This term leads to the optimal domain-wall width [111]:

$$\Delta = \sqrt{A/(K + K_{\perp}\sin^2\phi)}, \tag{4.48}$$

and for $\kappa = 0$ the optimal domain-wall width reduces to $\Delta_0 = \sqrt{A/K}$. In what follows, the domain-wall-width parameter $\Delta(t)$ is approximated by the optimal wall width. The parameter P is then

$$P = \frac{2K(1+\kappa\sin^2\phi)}{\mu_0 M_e^2} = \frac{2}{\mu_0 M_e^2}\frac{A}{\Delta^2}, \tag{4.49}$$

and it is straightforward to find its minimum $P_0 = 2K/(\mu_0 M_e^2)$, which corresponds to $\Delta = \Delta_0$.

The introduced parameter Q in Eq. (4.47) is given by $Q = (32/15)P^2(\chi/\alpha)^2$ and its value is determined by the ratio of χ and α, which could be ~ 1 although we assume $\chi \sim \alpha \ll 1$. Following the treatment of Ref. [111], the integrated Lagrangian action $\mathcal{L}$ is given by

$$\begin{aligned}\mathcal{L} &= \int (E_{\text{tot}} + \frac{\mu_0 M_e}{\gamma}\dot{\phi}\cos\theta)\, dx \\ &= \frac{2A}{\Delta} + 2\Delta K(1+\kappa\sin^2\phi)(1-V) - 2\mu_0 M_e H_a q + \frac{2\mu_0 M_e}{\gamma}\dot{\phi}q,\end{aligned} \tag{4.50}$$

where $\mu_0 M_e \dot{\phi}\cos\theta/\gamma$ is the Berry phase term [120], and $V = 8\chi P/3$ is a result of the varying magnetization that introduced a pinning potential. However, the potential is fairly small and therefore is negligible since $V \ll Q$. By substituting Eqs. (4.50) and (4.45) into Eq. (4.43),

$$\begin{aligned}\dot{\phi} + \alpha\frac{\dot{q}}{\Delta}(1+Q) &= \gamma H_a, \\ \frac{\dot{q}}{\Delta} - \alpha\dot{\phi} &= \gamma\frac{H_k}{2}\sin 2\phi.\end{aligned} \tag{4.51}$$

where $H_k = 2K_\perp/(\mu_0 M_e)$. The domain-wall dynamics is governed by Eq. (4.51), by eliminating $\dot{q}$ we obtain an equation about ϕ,

$$\dot{\phi} = \frac{\gamma}{1+\alpha^2(1+Q)}\left[H_a - H_w(1+Q)\sin 2\phi\right] \tag{4.52}$$

where $H_w = \alpha H_k/2$ is the Walker breakdown field. From Eq. (4.52) we can find that the critical value of ϕ is approximately equal to $\pi/4$ if $Q \ll 1$, which leads to the maximum value of P being $P_1 = 2K(1+\kappa/2)/(\mu_0 M_e^2)$. There exists an equilibrium state ϕ^* such that $\dot{\phi} = 0$ if $H_a < H_w(1+Q)$,

$$\sin(2\phi^*) = h \equiv \frac{H_a}{H_w(1+Q)}, \tag{4.53}$$

which means the Walker breakdown field H_w' for the $\chi > 0$ case is increased to $H_w(1+\max\{Q\})$, i.e.,

$$H_w' = H_w\left[1 + \frac{32}{15}P_1^2\left(\frac{\chi}{\alpha}\right)^2\right], \tag{4.54}$$

where P_1 is the maximum value of P. For this steady-state wall motion, the domain-wall velocity is

$$\dot{q} = \frac{\gamma H_a}{\alpha}\frac{\Delta^*}{1+Q(\Delta^*)}, \tag{4.55}$$

where

$$\Delta^* = \Delta_0/\sqrt{1+\frac{\kappa}{2}(1-\sqrt{1-h^2})}. \tag{4.56}$$

Therefore, $\Delta^* \to \Delta_0$ in the limit case $H_a \to 0$, and the domain-wall mobility μ is given by

$$\mu = \frac{\gamma\Delta}{\alpha}\left[1 + \frac{32}{15}P_0^2(\frac{\chi}{\alpha})^2\right]^{-1}, \tag{4.57}$$

where P_0 is the minimum value of P. In Fig. 4.3 the corresponding Walker breakdown fields are plotted as vertical dashed lines, which gives a good approximation for the $\chi = 5 \times 10^{-4}$ and $\chi = 1 \times 10^{-4}$ cases. The simulation results show that the Walker breakdown field H_w could be changed significantly if the longitudinal susceptibility is comparable to the damping constant.

4.4.2 Nonlocal damping

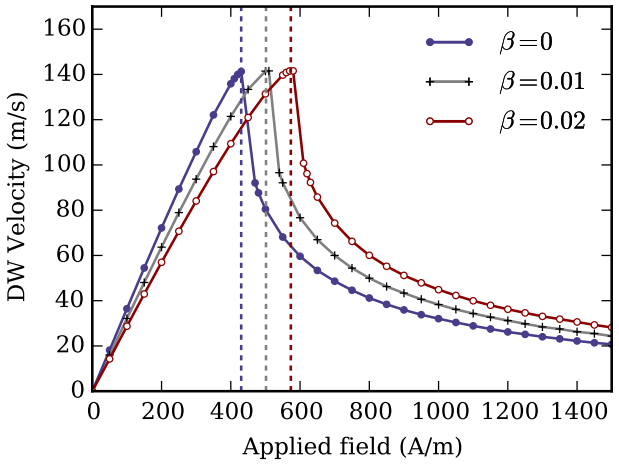

Figure 4.5: Simulation results of domain-wall velocities for the limit case that $\chi \to 0$ with various exchange dampings. The parameters used are: $\alpha = 0.005$, $N_y = 0.4$ and $N_z = 0.6$. The vertical dashed lines are the breakdown fields computed with Eq. (4.61).

In this part we consider the domain-wall motion influenced by exchange damping for the case that $\chi \to 0$. The dissipation density function (4.44) thus becomes

$$F = \frac{1}{2}\mu_0 M_e \gamma \left[\alpha \mathbf{H}_\perp^2 + \sigma(\nabla H_\theta)^2 + \sigma(\nabla H_\phi)^2\right], \tag{4.58}$$

where H_θ and H_ϕ are the two components of the effective field, and $\mathbf{H}_\perp$ is computed using Eq. (4.46). After performing the calculation we obtain

$$\mathcal{F} = \frac{\mu_0 M_e}{\gamma}\left[\dot{\phi}^2(\alpha\Delta + \frac{1}{3}\frac{\sigma}{\Delta}) + \frac{\dot{q}^2}{\Delta}(\alpha + \frac{1}{3}\frac{\sigma}{\Delta^2})\right]. \tag{4.59}$$

We take the same Lagrangian action (4.50) for $\chi = 0$ and arrive at

$$\begin{aligned} \dot{\phi} + (\alpha + \frac{\sigma}{3\Delta^2})\frac{\dot{q}}{\Delta} &= \gamma H_a, \\ \frac{\dot{q}}{\Delta} - (\alpha + \frac{\sigma}{3\Delta^2})\dot{\phi} &= \gamma \frac{H_k}{2} \sin 2\phi. \end{aligned} \tag{4.60}$$

Similarly, the corresponding Walker breakdown field changes to

$$H'_w = \frac{1}{2} H_k \left(\alpha + \frac{1}{3} \frac{\sigma}{\Delta_1^2} \right), \tag{4.61}$$

where $\Delta_1 = \Delta_0 \sqrt{1/(1+\kappa/2)}$. The domain-wall mobility is given by

$$\frac{1}{\mu} = \frac{1}{\gamma \Delta_0} \left(\alpha + \frac{1}{3} \frac{\sigma}{\Delta_0^2} \right). \tag{4.62}$$

As we can see, the nonlocal damping term σ influences the domain-wall motion as well, and we can establish that $\sigma/\Delta^2 = \beta(1+\kappa/2)K/(\mu_0 M_e^2) \propto \beta$. Therefore, for the scenarios that $K \sim \mu_0 M_e^2$, the contributions from the Gilbert and nonlocal damping are of the order of magnitude for both the domain-wall mobility and Walker breakdown field.

Figure 4.5 shows the domain-wall velocities for domain-wall motion driven by external fields in the limiting case of $\chi \to 0$. The simulation results are based on a one-dimensional mesh with a length of 10000 nm and a cell size of 2 nm. The damping α is set to 0.005 and the demagnetizing factors are chosen to be $N_x = 0$, $N_y = 0.4$ and $N_z = 0.6$. As predicted by Eq. (4.61), the nonlocal damping β leads to an increment of the Walker breakdown field, and Eq. (4.61) fits the simulation results very well.

4.5 Ferromagnetic resonance (FMR)

The nonlocal damping effect can be measured from Ferromagnetic resonance (FMR) [41]. In what follows, we compute the magnetic absorption spectra for the given systems and then extract the damping α from the magnetic spectra. The magnetic spectra are calculated by applying a sinc-function pulse in the form $\mathbf{h} = h_0 \mathrm{sinc}(\omega_0 t)\mathbf{e}_z$ to the stable states, we collect the average magnetization evaluation and thus the dynamical susceptibility χ can be computed by means of the Fourier transformation. For an ellipsoidal magnet the xy-component of susceptibility χ_{xy} is given by

$$\chi_{xy}(\omega) = \frac{-i\omega_m \omega}{(\omega_x + i\alpha\omega)(\omega_y + i\alpha\omega) - \omega^2}, \tag{4.63}$$

where α is the Gilbert damping, $\omega = \gamma M_s$, $\omega_x = \gamma H_x$ and $\omega_y = \gamma H_y$. The effective fields in x- and y- directions are H_x and H_y, respectively.

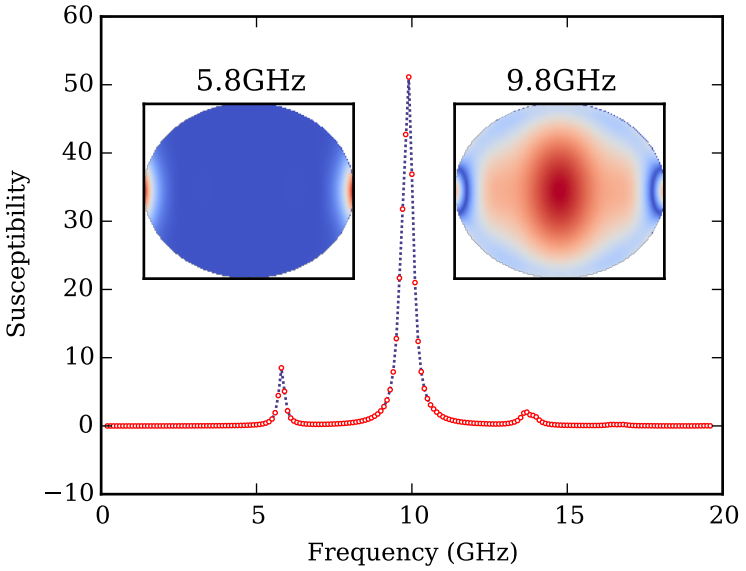

Figure 4.6: Real part of dynamic susceptibility χ_{xy} for an elliptical-shaped nanomagnet. Inset: Power plotting of the "End mode" and the "Center mode".

Next, we consider the elliptical-shaped nanomagnets with the nominal dimensions are $240 \times 200 \times 10\,\mathrm{nm}^3$, $360 \times 300 \times 10\,\mathrm{nm}^3$ and $480 \times 400 \times 10\,\mathrm{nm}^3$, respectively. Figure 4.6 shows the magnetic spectra for the ellipsoidal magnet with a width of 300 nm, and a cell size of $2.5 \times 2.5 \times 5\,\mathrm{nm}^3$ has been used. In addition, an external field $H_e = 500$ mT is applied in the x-direction. Three peaks are found from the dynamic susceptibility. The first two peaks are found at frequencies $f = 5.9$ GHz and $f = 9.9$ GHz, and lowest frequency is the so called "End mode", as we can see from the Insert of Fig. 4.6. The second mode is the "Center mode" with frequency $f = 9.9$ GHz.

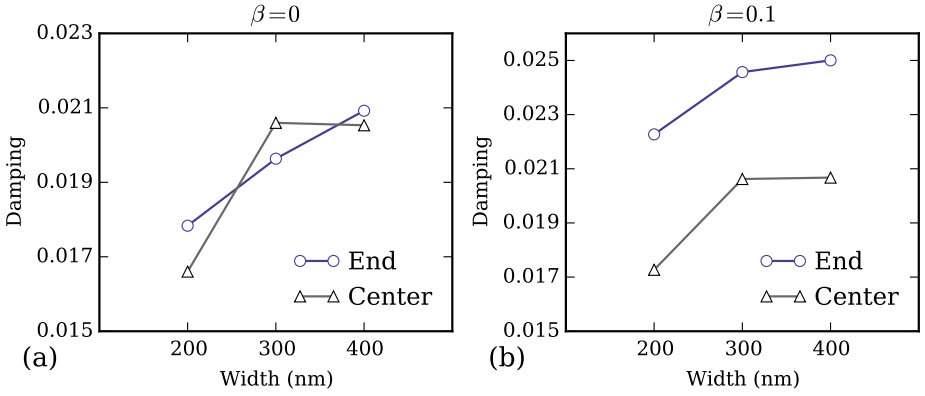

Figure 4.7: (a) The extracted damping as a function of the nanomagnet width using LLG equation. (b) The corresponding damping using the LLBar equation with $\beta = 0.1$. The Gilbert damping $\alpha = 0.01$ is used.

Figure 4.7 shows the fitted damping using Eq. (4.63) from the simulation data for

different samples. In the simulation, the Gilbert damping is fixed at $\alpha = 0.01$. The extracted damping is larger than the inputted Gilbert damping. For the "End mode", the largest sample (its width is 480 nm) has the highest fitted damping while the second sample has the highest fitted damping for the "Center mode". In the presence of exchange damping, i.e, $\beta > 0$, all the fitted dampings are increased. However, the increment for the "End mode" is much larger than that for the "Center mode".

4.6 Summary

We explain the "exchange damping" in the Landau-Lifshitz-Baryakhtar (LLBar) equation as nonlocal damping by linking it to the spin current pumping, and therefore the LLBar equation (4.17) can be considered as a phenomenological equation to describe the nonlocal damping. In the presence of nonlocal damping, the lifetime and propagation length of short-wavelength magnons could be much shorter than those given by the LLG equation. Our simulation results show that the spin-wave amplitude decays much faster in the presence of nonlocal damping when spin waves propagate along a single rod. The analytical result shows that there is extra nonlinear dependence scaling with k^2 between λk (the product of spin-wave decay constant λ and wave vector k) and frequency ω due to the nonlocal damping. Using the micromagnetic simulation based on the LLBar equation, we show that the difference between magnetization length M and M_e reaches its maximum at the center of the domain wall. For the cases that $\chi \sim \alpha$ where χ is the longitudinal magnetic susceptibility and α is the Gilbert damping, the Walker breakdown field will increase significantly. By using a 1D domain-wall model, we also show that both the domain-wall mobility and the Walker breakdown field are strongly influenced by the nonlocal damping as well.

Chapter 5

Magnon-driven domain-wall motion with Dzyaloshinskii-Moriya interaction

Preface

In this chapter, we have used the parameters of Permalloy in the micromagnetic simulations, the work presented in this chapter with parameters of material FeGe has been published in [2].

5.1 Introduction

A magnetic domain wall (DW) is a topological soliton in magnetic materials. The manipulation of domain-wall motion has been extensively studied in the past few years due to potential applications in logic devices and data storage technology [121–125]. A DW can be driven by an applied field [78], microwaves [126], spin transfer torque [28] and spin waves (magnons) [30, 115, 127]. Spin waves can drive the DW effectively since they carry magnonic spin current. In general, when the spin waves travel through a DW, the DW acquires a negative velocity – relative to the propagation direction of the spin waves – due to conservation of angular momentum [127], although positive velocities have been observed in micromagnetic simulations at special frequencies [36, 115, 128, 129].

Angular momentum conservation plays a crucial role in spin wave induced DW motion: when the spin wave passes through the DW, the magnonic spin current changes its sign, which generates a torque and the DW moves in order to absorb this torque. Magnons

can be considered as particles with angular momentum $\pm\hbar$ and linear momentum $\hbar k$ [127]. When the spin wave is reflected, linear momentum is transferred to the DW which results in DW motion [36, 130]. The difference between these two mechanisms is that the DW moves in opposite directions [130, 131].

The Dzyaloshinskii-Moriya interaction (DMI) is an anti-symmetric interaction induced by spin-orbit coupling due to broken inversion symmetry in lattices or at the interface of magnetic films [61]. The DMI can lead to chiral magnetic orders such as skyrmions and spin spirals [61, 62, 132, 133]. In addition, the DMI has brought new phenomena for DW dynamics driven by fields [45] or charge currents [46]. The DMI has been found both for magnetic interfaces [62] and bulk materials such as MnSi [63] and FeGe [64]. It is well known that DMI leads to nonreciprocal spin-wave propagation [133]. So it is very natural to ask what will happen when magnons pass through a DW in the presence of DMI.

In this chapter, we perform the micromagnetic simulation for a one-dimensional (1d) system with DMI and anisotropies. We demonstrate that spin waves passing through a domain wall in the presence of DMI and an easy-plane anisotropy drive the domain wall very effectively. We attribute this to linear momentum transfer and show that this effect can be an order of magnitude more efficient than the better known angular momentum transfer.

5.2 The system

In this work we focus on bulk DMI with micromagnetic energy density $\varepsilon_{\text{dmi}} = D\mathbf{m}\cdot(\nabla\times\mathbf{m})$ where D is the DMI constant and $\mathbf{m}$ is the normalized magnetization. We consider a quasi-1D nanowire with exchange interaction, DMI and two effective anisotropies. One anisotropy K is the uniaxial anisotropy along the x-axis, and the other effective $K_\perp$ is an easy xy-plane anisotropy. The combined anisotropies can be considered as a model of overall effect including the demagnetization field, surface or magnetoelastic anisotropy [64, 134]. The total free energy for the wire along the x-axis is

$$E = S\int \left[A(\nabla\mathbf{m})^2 - Km_x^2 + K_\perp m_z^2 + \varepsilon_{\text{dmi}}\right] \mathrm{d}x, \tag{5.1}$$

where S is the cross-sectional area of the wire and A is the exchange constant. The dynamics of the magnetization $\mathbf{m}$ is governed by the Landau-Lifshitz-Gilbert (LLG) equation

$$\frac{\partial\mathbf{m}}{\partial t} = -\gamma\mathbf{m}\times\mathbf{H}_{\text{eff}} + \alpha\mathbf{m}\times\frac{\partial\mathbf{m}}{\partial t}, \tag{5.2}$$

where γ (>0) is the gyromagnetic ratio and α is the Gilbert damping. The effective field $\mathbf{H}_{\text{eff}}$ is calculated as the functional derivative $\mathbf{H}_{\text{eff}} = -1/(\mu_0 M_s)\delta E/\delta\mathbf{m} =$

$2/(\mu_0 M_s)[A\nabla^2\mathbf{m} - D\nabla\times\mathbf{m} + Km_x\mathbf{e}_x - K_\perp m_z\mathbf{e}_z]$ with M_s the saturation magnetization and μ_0 the vacuum permeability.

5.3 Domain-wall profile and Spin-wave excitation

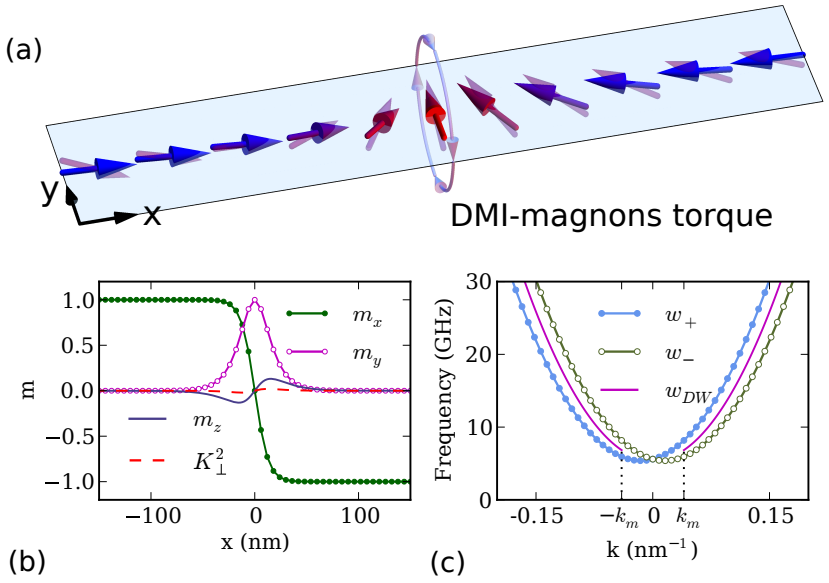

Figure 5.1: (a) Illustration of the head-to-head DW in the nanowire using red-blue opaque arrows, the translucent purple arrows represent a spin-wave excitation. The DMI exerts a torque to change the DW tilt angle when spin waves pass through the DW. (b) DW profile using Eq. (5.7) with parameters $A = 1.3\times10^{-11}\,\mathrm{J/m}$, $K = 8\times10^4\,\mathrm{J/m^3}$, $D = 4\times10^{-4}\mathrm{J/m^2}$ and $M_s = 8.0\times10^5\,\mathrm{A/m}$ for $K_\perp = 0$. The red dashed line shows the simulation data for m_z with $K_\perp^2 = 6\times10^5\,\mathrm{J/m^3}$: the easy-plane anisotropy favours a reduced m_z. (c) The dispersion relations inside and outside the DW.

The typical DW structures described by the energy [Eq. (5.1)] for the case $D = 0$ are head-to-head and tail-to-tail DWs, and the former is shown in Fig. 5.1(a). By using spherical coordinates $\theta = \theta(x)$ and $\phi = \phi(x)$, the magnetization unit vector $\mathbf{m}$ is expressed as $\mathbf{m} = (\cos\theta, \sin\theta\cos\phi, \sin\theta\sin\phi)$, and the total micromagnetic energy [Eq. (5.1)] reads

$$E = S\int\left[A(\theta'^2 + \sin^2\theta\phi'^2) - D\phi'\sin^2\theta + K\sin^2\theta(1+\kappa\sin^2\phi)\right]\mathrm{d}x, \tag{5.3}$$

where $\kappa = K_\perp/K$ and $'$ represents the derivative with respect to x. In equilibrium state, the energy (5.3) must be minimal, i.e., the Lagrangian density $\mathcal{L} = \mathcal{H}$ satisfies the Euler-Lagrange equation,

$$\frac{\partial L}{\partial f} - \frac{d}{dx}\frac{\partial L}{\partial f'} = 0, \tag{5.4}$$

where $f = \theta, \phi$ and $\mathcal{H} = A(\theta'^2 + \sin^2\theta\phi'^2) - D\phi'\sin^2\theta + K\sin^2\theta(1+\kappa\sin^2\phi)$. Therefore, we arrive at two coupled differential equations for θ and ϕ,

$$\begin{aligned} 2A\theta'' &= \sin 2\theta(A\phi'^2 + K(1+\kappa\sin^2\phi) - D\phi'), \\ \sin\theta(2A\phi'' - K_\perp \sin 2\phi) &= 2\cos\theta(D - 2A\phi')\theta'. \end{aligned} \tag{5.5}$$

The corresponding boundary conditions are $\theta' = 0$ and $(\phi' - 1/\xi)\sin^2\theta = 0$ for $x = \pm\infty$ where $\xi = 2A/D$ is the characteristic length [62]. These boundary conditions are given by

$$\frac{\partial L}{\partial f'} = 0 \quad \text{at the boundary.} \tag{5.6}$$

We now search for the head-to-head DW solution, therefore the ansatz $\cos\theta = -\tanh[(x-x_0)/\Delta]$ is used, where Δ is the DW width and x_0 is the DW center. Initially, we consider the case of $\kappa = 0$ (i.e. $K_\perp = 0$) which preserves the rotational symmetry. We assume that ϕ is a linear function of space x, i.e., $\phi(x) = (x-x_0)/\xi + \Phi$ where Φ is the DW tilt angle. Inserting it back to Eq. (5.5) we obtain $\Delta = \sqrt{A/(K - A/\xi^2)}$. In the absence of DMI, the DW width reduces to $\Delta_0 = \sqrt{A/K}$ which is the well known Bloch wall width. Therefore the static one-dimensional head-to-head DW profile can be expressed as [46]

$$\begin{aligned} m_x &= -\tanh(x/\Delta), \\ m_y &= \operatorname{sech}(x/\Delta)\cos(x/\xi + \Phi), \\ m_z &= \operatorname{sech}(x/\Delta)\sin(x/\xi + \Phi), \end{aligned} \tag{5.7}$$

where we have chosen $x_0 = 0$. Fig. 5.1(b) shows the DW profile using Eq. (5.7) for $K_\perp = 0$ with lines, and the red dashed line depicts the micromagnetic simulation result of m_z for $K_\perp^2 = 6\times10^5\,\mathrm{J/m^3}$. The rotational symmetry breaks for $K_\perp > 0$ and the z-component of the magnetization m_z is suppressed by the easy plane anisotropy. The DW configuration (5.7) is not stable if the DMI constant is larger than the critical value $D_c = 2\sqrt{AK}$ [46], and the presence of $K_\perp > 0$ increases this threshold.

We assume that the spin wave can be described by a small fluctuation $u = u(x)$ and $v = v(x)$ around $\mathbf{m}_0$, where $\mathbf{m}_0 = (\cos\theta_0, \sin\theta_0\cos\phi_0, \sin\theta_0\sin\phi_0)$ is the static domain-wall profile Eq.(5.7),

$$\mathbf{m} = \mathbf{m}_0 + [u(x)\mathbf{e}_\theta + v(x)\mathbf{e}_\phi]e^{-iwt}, \tag{5.8}$$

where $\sqrt{u^2+v^2} \ll 1$ and ω is the spin-wave frequency. The unit vectors $\mathbf{e}_\phi$ and $\mathbf{e}_\theta$ are defined as $\mathbf{e}_\phi = (0, -\sin\phi_0, \cos\phi_0)$ and $\mathbf{e}_\theta = (-\sin\theta_0, \cos\theta_0\cos\phi_0, \cos\theta_0\sin\phi_0)$. By following the treatment in Ref. [127], we obtain for the $K_\perp = 0$ case,

$$\begin{aligned} Av'' - \tilde{K}v\cos(2\theta_0) &= -iu\omega/\gamma_0, \\ Au'' - \tilde{K}u\cos(2\theta_0) &= iv\omega/\gamma_0, \end{aligned} \tag{5.9}$$

where we define $\tilde{K} = K - D^2/4A$ and $\gamma_0 = 2\gamma/(\mu_0 M_s)$. By introducing the complex variable $\psi = u - iv$, Eq. (5.9) can be written as a time-independent Schrödinger-type equation with reflectionless potential [135, 136],

$$\hat{H}\psi(\zeta) = (1+q^2)\psi(\zeta), \tag{5.10}$$

where $\zeta = x/\Delta$ and the operator is $\hat{H} = -d^2/d\zeta^2 + 1 - 2\,\mathrm{sech}^2(\zeta)$. The eigenvalues $1 + q^2 = \omega/(\gamma_0\tilde{K})$ define the spin-wave dispersion relation inside the DW, which is plotted in Fig. 5.1(c) (magenta line) with wavevector $k = q/\Delta$. The above discussion is only valid for wavelengths smaller than the domain-wall size, which corresponds to wavevectors greater than $k_m \sim 1/(2\Delta)$. The propagating wave excitations can be expressed as $\psi(\zeta, t) = \rho_k e^{i\Omega}(\tanh(\zeta) - iq)$ where $\Omega = \zeta q - \omega t$ represents the sine or cosine type waves and ρ_k the wavevector-dependent spin-wave amplitude [137]. The reflectionless property for spin waves holds even in the presence of the easy plane anisotropy [138]. Interestingly, the dispersion relation inside the DW is symmetric in the reduced wavevector q even though the wall is twisted by the DMI. However, due to the exponential decay of the DW profile when moving away from the DW center, the magnetization is uniform in the domains and the dispersion relations become asymmetric outside the DW [133, 139],

$$\omega_\pm = \gamma_0(K + Ak^2 \pm Dk). \tag{5.11}$$

Fig. 5.1(c) shows the asymmetric dispersion relations outside the DW. The dispersion relation [Eq. (5.11)] also suggests that the wave vector changes by D/A when the spin wave passes through the DW if the frequency of the spin wave remains the same. The spin wave becomes elliptical rather than circular if $K_\perp > 0$ and the corresponding dispersion relation outside the DW becomes [133]

$$\omega_\pm = \gamma_0[\sqrt{(K + Ak^2)(K + K_\perp + Ak^2)} \pm Dk]. \tag{5.12}$$

5.4 Domain-wall motion

To study the DW dynamics, micromagnetic simulations have been performed using a 1D mesh with length 2000 nm and cell size 2 nm. The parameters used are typical of Permalloy: the exchange constant $A = 1.3 \times 10^{-11}\,\mathrm{J/m}$, the saturation magnetization $M_s = 8.0 \times 10^5\,\mathrm{A/m}$ and the damping coefficient $\alpha = 0.01$. The spin waves are excited locally in the region $-1000 \leq x \leq -998\,\mathrm{nm}$ by a linearly polarized microwave $\mathbf{h}(t) = h_0 \sin(\omega t)\mathbf{e}_y$ with $h_0 = 1 \times 10^5\,\mathrm{A/m}$. The initial domain wall is located at $x_0 = -50\,\mathrm{nm}$, and to prevent spin wave reflection the damping coefficient is increased linearly [115] from 0.01 to 0.5 in the region $800 \leq x \leq 1000\,\mathrm{nm}$.

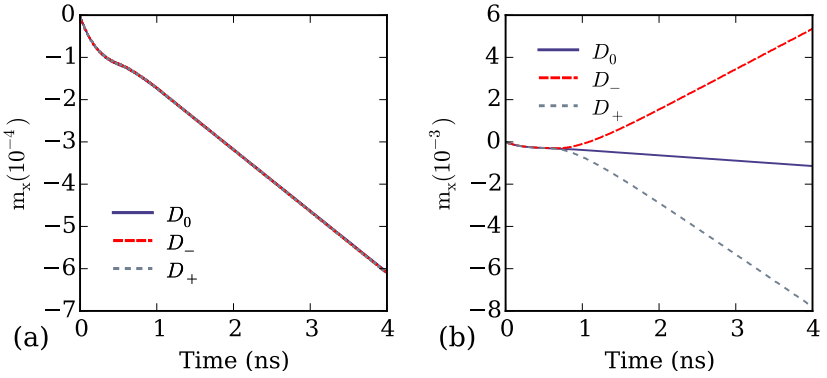

Figure 5.2: The domain-wall displacement for (a) $K_\perp = 0$ at frequency $f = 32$ GHz, and (b) $K_\perp = 6 \times 10^5\,\mathrm{J/m^3}$ at frequency $f = 32$ GHz. The DMI constants employed in the simulation are $D_0 = 0$ and $D_\pm = \pm 4 \times 10^{-4}\mathrm{J/m^2}$.

The spin-wave traveling in the $+x$ direction induces DW motion. Figure 5.2 shows the domain-wall displacements with and without easy plane anisotropy for various DMI constants. As shown in Fig. 5.2(a), it is found that both negative and positive DMI constants lead to identical domain-wall motion when $K_\perp = 0$. The domain-wall velocity is obtained by fitting the displacement of the domain wall (m_x as a function of time) and thus is calculated by $v = (L/2)(dm_x/dt)$ where L is the length of the wire.

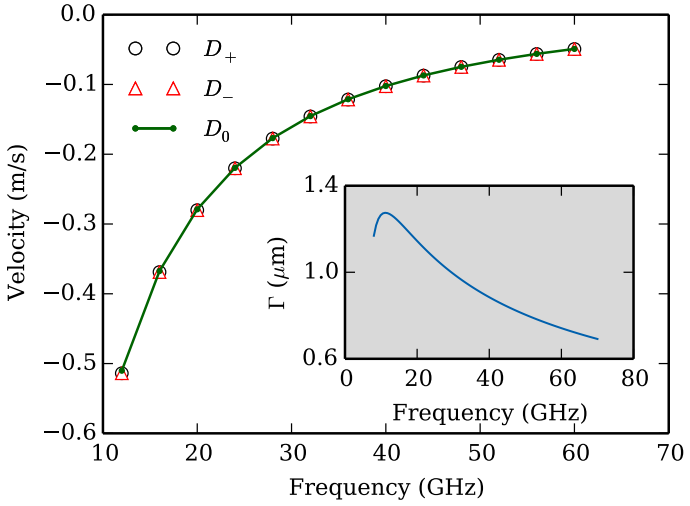

Figure 5.3: Simulation results of the DW velocity as a function of spin-wave frequency with different DMI constants for the case of $K_\perp = 0$. The DMI parameters are $D_0 = 0$ and $D_\pm = \pm 4 \times 10^{-4}\mathrm{J/m^2}$. Inset: Plot of spin-wave amplitude decaying characteristic length Γ versus frequency.

Figure 5.3 shows the DW velocity as a function of frequency with different DMI constants for $K_\perp = 0$. The DW velocity is negative, which is explained by conservation of angular momentum, and the DW velocity is $v_e = -(\rho^2/2)V_g$ [127], where $V_g = \partial\omega_k/\partial k$ is the group velocity and ρ is the spin-wave amplitude. For a circular spin wave,

i.e. for $K_\perp = 0$, by using the dispersion relation inside the DW or Eq. (5.11) we have $V_g = 2\gamma_0 Ak = 2\sqrt{\gamma_0 A(\omega - \gamma_0 \tilde{K})}$. The magnitude of the DW velocity first increases, and then decreases as the frequency of the spin wave increases. The reason for this is that the spin-wave amplitude decays exponentially as the spin wave propagates. To quantify this, we assume the magnetization has the form $\mathbf{m} = \pm\mathbf{e}_x + \boldsymbol{\rho_0} e^{i(kx-\omega t)} e^{-x/\Gamma}$ with $|\boldsymbol{\rho_0}| \ll 1$ [100, 133], and obtain $\Gamma_\pm = (2/\alpha\omega)[\gamma_0 Ak \pm D(\omega \mp D\gamma_0 k)/(K_\perp + 2K + 2Ak^2)]$, which is plotted in the inset of Fig. 5.3 with $K_\perp = 0$. The predicted DW velocity v_e is plotted in Fig. 5.3 as well, which fits the simulation results very well. From Fig. 5.3 we can see that the DMI has only a small influence on the DW velocity, in this case where $K_\perp = 0$ and the spin waves are circular.

We now repeat the study for Fig. 5.3 above with $K_\perp > 0$ and where the spin waves are elliptical. From Fig. 5.2(b) we can find that for the scenario of $K_\perp = 6 \times 10^5\,\mathrm{J/m^3}$, the sign of DMI constant influences the domain-wall motion significantly. Fig. 5.4 shows the DW velocity as a function of spin-wave frequency for $K_\perp = 6 \times 10^5\,\mathrm{J/m^3}$. As in the $K_\perp = 0$ case, the DW velocity is negative if the DMI constant D is > 0, and is enhanced by the DMI. The DW velocity is zero if the frequency is less than the cut-off frequency $f_{\mathrm{cut}} \sim 16.3\,\mathrm{GHz}$. The DW velocity first increases, and then decreases with the frequency due to the spin-wave amplitude decaying. However, for the $D < 0$ case the DW velocity is positive in a large frequency range, which is different from the reports in previous studies [36, 115, 129].

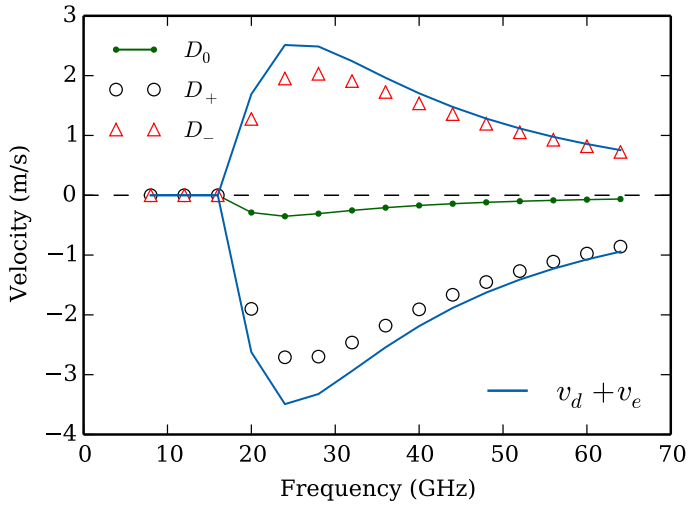

Figure 5.4: The DW velocity as the function of the spin-wave frequency with $K_\perp = 6 \times 10^5\,\mathrm{J/m^3}$. The DMI constants employed in the simulation are $D_0 = 0$ and $D_\pm = \pm 4 \times 10^{-4}\mathrm{J/m^2}$.

To understand this novel DMI induced linear momentum transfer phenomenon, we recall the dispersion relation [Eq. (5.11)] outside the DW and assume the wavevector of a magnon before and after passing through the DW to be k_1 and k_2, respectively. When

spin waves travel though the DW, they jump from branch ω_+ to ω_- in the dispersion relation, as depicted in Fig. 5.1(c). By assuming the frequency keeps the same, the change in wavevector $\delta k = k_2 - k_1$ can be calculated. The change in wavevector δk leads to a momentum change $\delta p = \hbar \delta k$ for each magnon.

The excited magnon density is $n = \rho^2 M_s/(2\hbar\gamma)$ [36] and for elliptical spin waves we choose $\rho^2 = u_0 v_0$ where u_0, v_0 are fluctuation amplitudes in $\mathbf{e}_\theta$ and $\mathbf{e}_\phi$. The linear momentum of a DW is $P_{\mathrm{DW}} = (M_s/\gamma)\int \phi \sin\theta(\partial\theta/\partial x)\mathrm{d}x = 2\Phi M_s/\gamma$ [140] and conservation of linear momentum [130] gives $dP_{\mathrm{DW}}/dt = -dP_{\mathrm{magnons}}/dt = -nV_g\delta p$, i.e., $\dot{\Phi} = -(1/4)\rho^2 V_g \delta k$. To describe the domain-wall motion, we introduce an effective field along the x direction by using the spherical form of the LLG equation,

$$H_x = \dot{\Phi}/\gamma = -\frac{1}{4}\rho^2 \delta k V_g/\gamma. \tag{5.13}$$

For circular spin waves $\delta k = D/A$, and thus the corresponding effective field is computed as $H_x^0 = -(\rho^2/2)Dk\gamma_0/\gamma$. In the $\kappa > 0$ case (i.e. for $K_\perp > 0$), the spin wave is elliptical and δk is a function of the frequency, as shown in Fig. 5.5(a). The presence of a non-zero $K_\perp$ suppresses the wavevector change, especially for low frequency spin waves. The DW velocity v_d induced by this effective field H_x in the presence of damping can be obtained using the rigid DW model [111],

$$v_d = \frac{\gamma \Delta H_x}{\alpha} \Big/ \sqrt{1 + \frac{\kappa}{2}\left(1 - \sqrt{1-h^2}\right)}, \tag{5.14}$$

where $h = H_x/(\alpha H_{K_\perp})$ and $H_{K_\perp} = 2K_\perp/(\mu_0 M_s)$. The total velocity is the sum of the established v_d and v_e, which correspond to the linear and angular momentum conservation, respectively.

To estimate the total velocity $v_e + v_d$, we have extracted the spin wave amplitude ρ at $x = 0$ (the initial position of the domain wall) from the simulation and the constant DW width Δ_0 is used. This total velocity is shown as lines in Fig. 5.4 and shows a good agreement with the simulation results shown as circle and triangle symbols. The DW can rotate freely if $K_\perp = 0$ and the DW velocity induced by the field H_x is $v_0 = \alpha\Delta\gamma_0 H_x/(1+\alpha^2)$. We can establish that $v_0 \sim 10^{-4}$ m/s, which could explain why the linear momentum exchange is not significant for the DW motion shown in Fig. 5.3.

So far the effective field is introduced by linear momentum conservation. In the following section we cross-check this using the LLG equation. The LLG equation (5.2) with zero damping is rewritten to describe the spin conservation law [57],

$$\frac{\partial \mathbf{m}}{\partial t} + \frac{\partial \mathbf{j}_e}{\partial x} = \boldsymbol{\tau}_a + \boldsymbol{\tau}_d \tag{5.15}$$

where $\mathbf{j}_e = \gamma_0 A \mathbf{m} \times \nabla \mathbf{m}$ is the exchange spin current associated with localized spin. The spin source or sink $\boldsymbol{\tau}_a = -\gamma_0 \mathbf{m} \times [K m_x \mathbf{e}_x - K_\perp m_z \mathbf{e}_z]$ and $\boldsymbol{\tau}_d = \gamma_0 D \mathbf{m} \times (\nabla \times$

m) come from the anisotropy and DMI, respectively. The average DW velocity can be computed as the overall magnetization, $v = (1/2)\int \langle \partial m_x/\partial t \rangle \, \mathrm{d}x$ where $\langle f(t) \rangle$ represents the temporal average for the function $f(t)$. For magnons we keep this average to the square of the amplitude of the spin waves and ignore the higher-order ones. By integrating over space for the x-component of the spin current $\mathbf{j}_e$, the velocity v_e can be recovered.

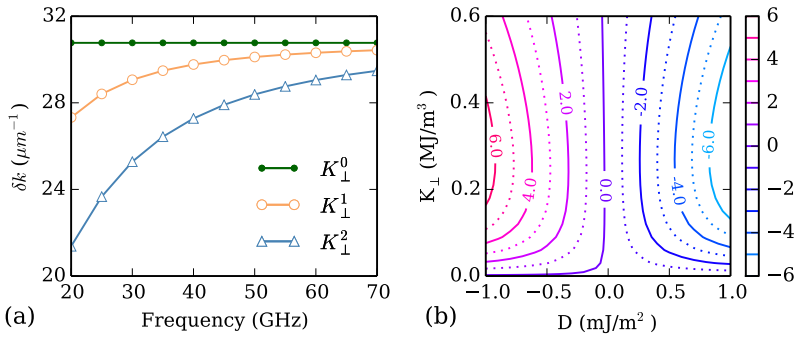

Figure 5.5: (a) Plot of δk as a function of the frequency for $K_\perp^0 = 0$, $K_\perp^1 = 3 \times 10^5\,\mathrm{J/m^3}$ and $K_\perp^2 = 6 \times 10^5\,\mathrm{J/m^3}$ with $D = 4 \times 10^{-4}\,\mathrm{J/m^2}$. (b) The contour plot of the simulated DW velocity for different $K_\perp$ and DMI constants, the frequency of the external ac field is fixed at 30GHz with the amplitude 500A/m, and the damping α is 0.01.

By using the DW profile (5.7) it is found that the overall contributions of the x-component torques $\boldsymbol{\tau}_a$ and $\boldsymbol{\tau}_d$ are zero, i.e., $\int \langle \boldsymbol{\tau}_a^x \rangle dx = \int \langle \boldsymbol{\tau}_d^x \rangle dx = 0$. However, the contribution of the z-component of the DMI is nonzero, i.e., $\int \langle \boldsymbol{\tau}_d^z \rangle dx = -\int (\rho^2/2)\gamma_0 D k \, m_y dx$, represents an additional torque rotating the DW plane. By introducing an effective field H_x^0 in the x direction such that the total torque on the DW equals the torque $\boldsymbol{\tau}_d^z$, we obtain $H_x^0 = \int \langle \boldsymbol{\tau}_d^z/\gamma \rangle dx \Big/ \int m_y dx = -(\rho^2/2) D k \gamma_0/\gamma$, which is in exact agreement with the analysis above.

Fig. 5.5(b) shows a contour plot of the DW velocity as a function of $K_\perp$ and DMI constant D. The figure is approximately symmetric in the DMI constant, with a biased velocity originating from the angular momentum exchange between the spin wave and the DW. The DW velocity is always negative if $D > 0$. There exist some optimal areas in which the DW has the highest velocity, and this area depends on the frequency of the spin wave.

5.5 Two types of domain walls

In Section 5.3 we discussed the domain-wall profile for the $K_\perp = 0$ case. By assuming the constant DW width Δ and the linear dependence of ϕ we obtain $\Delta =$

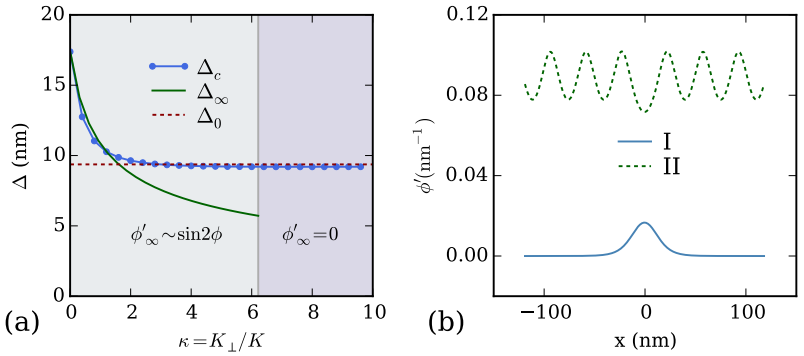

Figure 5.6: (a) Plot of two types of domain walls, Δ_c is obtained by fitting the simulation data with $\cos\theta = -\tanh(x/\Delta_c)$. (b) Two types of domain walls obtained from simulation data of type I with $K_\perp = 8\times10^5\,\mathrm{J/m^3}$ and type II with $K_\perp = 8\times10^4\,\mathrm{J/m^3}$. The used parameters are FeGe [2].

$\sqrt{A/(K-A/\xi^2)}$ where $\xi = 2A/D$ is the characteristic length. However, these assumptions are not true for $K_\perp > 0$ case. To estimate the DW width in general case we start with Eq. (5.5). Assuming that the DW profile can be described by,

$$\cos\theta = -\tanh f(x), \qquad \sin\theta = \operatorname{sech} f(x), \tag{5.16}$$

where $f(x)$ is an unknown function of space and thus the DW width is related to $f'(x)$, we expect $f(x)$ is a monotonic non-decreasing function. From Eq. (5.7) we know that $\theta' = \sin\theta f'(x)$ and $\theta'' = \sin\theta[\cos\theta f'(x)^2 + f''(x)]$, and by considering the first equation of Eq. (5.5) we assume $f''(x) = g(x)\cos\theta$ since $f''(x) = 0$ leads to a constant DW width. Therefore, we arrive at,

$$A(f'^2 + g) = A\phi'^2 + K + K_\perp \sin^2\phi - D\phi' \tag{5.17}$$

Note that for the $K_\perp = 0$ case $f'^2 + \phi'^2 = K/A$ and by combining it with the second equation of Eq. (5.5), we assume

$$A(f'^2 + \phi'^2) = K + K_\perp \sin^2\phi, \tag{5.18}$$

which leads to $Ag = (2A\phi' - D)\phi'$ and further more,

$$Af'' = -(2A\phi' - D)\phi' \tanh f. \tag{5.19}$$

We can check that Eq. (5.18) and Eq. (5.19) are the solutions of Eq. (5.5). The asymptotic behavior of f'' can be obtained from Eq. (5.19) by making use of the fact that $\tanh f \to 1$ in the limit of $x \to +\infty$. We can distinguish two types of domain walls according to the value of $f''_\infty = \lim_{x\to+\infty} f''(x)$.

The first case is that $f''_\infty = 0$, which requires $\phi'_\infty = D/(2A)$ or $\phi'_\infty = 0$. Note that

$\phi'_\infty = D/(2A)$ corresponds to the DW profile obtained in the main content, which is only valid for $K_\perp = 0$ case. Therefore, we identify the first type of the DW with $\phi'_\infty = 0$. As an approximation, we assume $\phi = a\tanh(\nu x)$ for this type of wall, so we have $f'_0 = \sqrt{K/A - a^2\nu^2}$ and $f'_\infty = \sqrt{(K + K_\perp \sin^2 a)/A}$. As we can see, the DW width is bounded by f'_0 and f'_∞. By using $\nu \sim \sqrt{K/A}$ we find that $a \to 0$ in the limit of $\kappa \to \infty$ and thus $\Delta \to \sqrt{A/K}$.

The second case is that f''_∞ does not converge and $\phi(x)$ is a monotonic function. From Eq. (5.18) one can deduce that at least one of f' and ϕ' oscillates, and combining Eq. (5.19) we conclude that both of them oscillate. In this scenario, we take the following approximation forms for $f \gg 1$,

$$\begin{aligned} \phi' &= \eta - c\cos(2\phi - \phi_0), \\ f' &= \lambda + c\sin(2\phi - \phi_0), \end{aligned} \tag{5.20}$$

where $\eta = 1/\xi = D/(2A)$. We can find that this assumption satisfies Eq. (5.19). Substitute Eq. (5.20) into Eq. (5.18) and to eliminate the term $\sin 2\phi$ one obtains $\sin\phi_0 = \lambda/\sqrt{\lambda^2+\eta^2}$ and $\cos\phi_0 = \eta/\sqrt{\lambda^2+\eta^2}$. Finally, we arrive at,

$$\lambda^2 = \frac{K}{A}\frac{1 + \kappa/2 + \sqrt{1+\kappa}}{2} - \eta^2, \tag{5.21}$$

and thus the domain-wall width $\Delta_\infty = 1/\lambda$ can be established. The oscillation amplitude is given by $c = K_\perp/(4A\sqrt{\eta^2+\lambda^2})$. This solution is only valid for weak easy plane anisotropy case that requires $c < \eta$. And thus the critical κ_c can be obtained by solving the equation $K\kappa_c = 2D\sqrt{\eta^2+\lambda^2}$, i.e., $AK\kappa_c^2 = 2D^2(1 + \kappa_c/2 + \sqrt{1+\kappa_c})$. Figure 5.6(a) shows the DW width of the two types of domain walls, and the corresponding ϕ' is shown in Fig. 5.6(a) using the data extracted from simulation.

5.6 Summary

In this chapter, we have studied the DW motion induced by spin waves in the presence of DMI. We found that the DMI exerts an extra torque which rotates the DW plane when the spin wave passes through the DW. This torque represents a linear momentum exchange between the spin wave and the DW. The effect of the linear momentum is equivalent to an effective field and the direction of the field depends on the sign of DMI constant and DW profile. This linear momentum exchange between spin waves and DW exists in addition to the angular momentum exchange, and is more efficient in moving the DW.

Chapter 6

Driving magnetic skyrmions with microwave fields

Preface

The work presented in this chapter has been published in [3].

6.1 Introduction

Magnetic skyrmions are topologically stable magnetization textures with particle-like properties. As proposed by Skyrme [141], the skyrmions are considered to be topologically protected, in the sense they can not be changed by a continuous deformation of the field configuration. Magnetic skyrmions have been found experimentally [63, 142–145] in various materials, such as MnSi, FeGe as well as the ultrathin transition metal films.

Magnetic skyrmions have recently attracted great attention [47, 61, 63, 146] due to the novel transport properties and the potential use in future spintronic devices [144]. The manipulation of skyrmions is of great importance and interest: skyrmions can be driven using spin-polarized current [48, 49, 132, 147], magnetic or electric field gradients [32, 50], temperature gradients [33, 148, 149] and magnons [51, 81, 150]. Microwaves, on the other hand, have been broadly used in studying various magnetic phenomena, such as the ferromagnetic resonance (FMR) and spin wave excitations in skyrmion crystals [151–154]. However, the possibility of creating translational motion of skyrmions has not been explored in these experiments [152–154].

In this Chapter, by using a classical spin model on a two-dimensional system with Dzyaloshinskii-Moriya Interaction (DMI), we show that both a single skyrmion and a

skyrmion lattice can be moved by microwave fields if the axial symmetry of skyrmions is slightly broken by a static in-plane external field.

6.2 The system and asymmetric skyrmions

We employ skyrmions stabilized by the Dzyaloshinskii-Moriya Interaction (DMI) [43, 44]. More precisely, the bulk DMI is considered so that a chiral skyrmion (vortex-like) rather than a hedgehog (radial) skyrmion configuration emerges [63, 155, 156]. We start with a classical Heisenberg model on a two-dimensional regular square lattice with nearest-neighbor symmetric exchange interaction, the bulk-type DMI, and the Zeeman field [33, 151, 157]. In addition, a time-dependent magnetic field $\mathbf{h}(t)$ is applied in the $+z$-direction. Accordingly, the system's Hamiltonian can be written as

$$\mathcal{H} = -J \sum_{\langle i,j \rangle} \mathbf{m}_i \cdot \mathbf{m}_j + \sum_{\langle i,j \rangle} \mathbf{D}_{ij} \cdot [\mathbf{m}_i \times \mathbf{m}_j] - \sum_i |\boldsymbol{\mu}_i| (\mathbf{H} + \mathbf{h}(t)) \cdot \mathbf{m}_i, \tag{6.1}$$

where $\langle i,j \rangle$ represents a unique pair of lattice sites i and j, $\mathbf{m}_i$ is the unit vector of the magnetic moment $\boldsymbol{\mu}_i = -\hbar\gamma \mathbf{S}_i$ with $\mathbf{S}_i$ being the atomic spin and $\gamma(>0)$ the gyromagnetic ratio, and J is the symmetric exchange energy constant. In the case of bulk DMI, the DMI vector $\mathbf{D}_{ij}$ can be written as $\mathbf{D}_{ij} = D\hat{\mathbf{r}}_{ij}$, where D is the DMI constant and $\hat{\mathbf{r}}_{ij}$ is the unit vector between $\mathbf{S}_i$ and $\mathbf{S}_j$. We use the DMI value with $D/J = 0.18$, which results in the spiral period $\lambda \sim 2\pi Ja/D \sim 25\,\text{nm}$ for a typical lattice constant $a = 0.5$ nm [49]. We consider two nonzero components for the static external field $\mathbf{H}$: an in-plane component H_y and a perpendicular component H_z, i.e., $\mathbf{H} = (0, H_y, H_z)$. A nonzero H_z is essential for stabilizing the skyrmion crystal [151].

The spin dynamics at lattice site i is governed by the Landau-Lifshitz-Gilbert (LLG) equation,

$$\frac{\partial \mathbf{m}_i}{\partial t} = -\gamma \mathbf{m}_i \times \mathbf{H}_{\text{eff}} + \alpha \mathbf{m}_i \times \frac{\partial \mathbf{m}_i}{\partial t} \tag{6.2}$$

where α is the Gilbert damping and $\mathbf{H}_{\text{eff}}$ is the effective field that is computed as $\mathbf{H}_{\text{eff}} = -(1/|\boldsymbol{\mu}_i|)\partial\mathcal{H}/\partial\mathbf{m}_i$. The Hamiltonian (6.1) associated with the LLG equation (6.2) can be understood as a finite-difference-based micromagnetic model. Therefore, our simulation results are reproducible by setting the saturation magnetization $M_s = \hbar\gamma S/a^3$, exchange constant $A = J/2a$ and DMI constant for continuum form $D_a = -D/a^2$ [corresponding to the energy density $\varepsilon_{\text{dmi}} = D_a \mathbf{m} \cdot (\nabla \times \mathbf{m})$] in micromagnetic simulation packages such as OOMMF [24]. We have carried out simulations with and without dipolar interactions, and the results are qualitatively the same. We report results without dipolar interactions for clarity of the model assumptions.

A two-dimensional system of size $N = 160 \times 160$ sites with periodic boundary conditions is selected to study the dynamics of a single skyrmion, Fig. 6.1(a), and

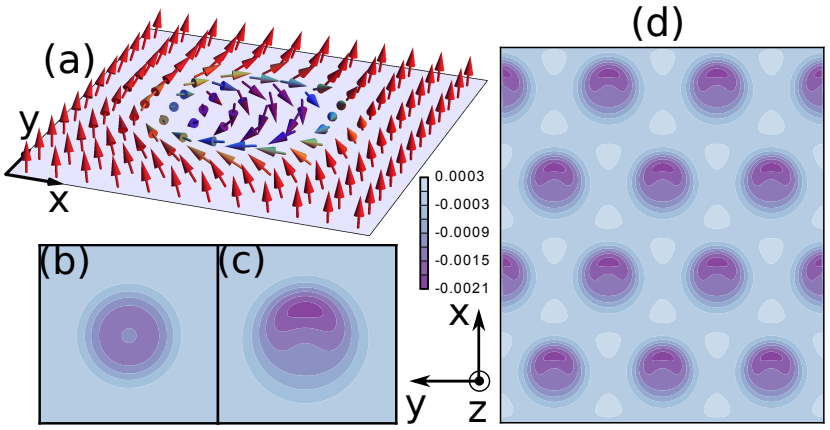

Figure 6.1: (a) Skyrmion configuration in the presence of an in-plane field $H_y = 0.006$ with $D = 0.18$, $J = 1$ and $H_z = 0.02$. (b) The symmetric topological charge density distribution of a skyrmion when $H_y = 0$. (c) The corresponding topological charge density for the skyrmion shown in (a) when $H_y > 0$. (d) The skyrmion lattice with 12 skyrmions in a sample of size $N = 174 \times 150$ sites, with an in-plane field $H_y = 0.004$.

$N = 174 \times 150$ sites for the skyrmion lattice, as shown in Fig. 6.1(d). We have chosen $J = \hbar = \gamma = S = a = 1$ as simulation parameters [151, 158], therefore, the coefficients to convert the external field H, time t, frequency ω and velocity v to SI units are $\hat{H} = J/\hbar\gamma S$, $\hat{t} = \hbar S/J$, $\hat{\omega} = J/\hbar S$ and $\hat{v} = Ja/\hbar S$, respectively. Table 6.1 shows the expressions, and particular values for the case of $J = 1$ meV, $S = 1$ and $a = 0.5$ nm. We use simulation units throughout the paper. The perpendicular component H_z is fixed as $H_z = 0.02$ which corresponds to 0.173 T for $S = 1$ and $J = 1$ meV. We use Gilbert damping $\alpha = 0.02$ for all simulations except for the magnetic spectra shown in Fig. 6.2 where $\alpha = 0.04$ is chosen. For the single skyrmion dynamics, we apply the absorbing boundary conditions for damping [2] by setting $\alpha = 1.0$ for the 20 spins at the edges of a simulated domain.

The configuration of a skyrmion in the presence of an in-plane field $H_y = 0.006$ is shown in Fig. 6.1(a). It is found that the radial symmetry is broken. Indeed, as shown in Fig 6.1(c), the corresponding distribution of the topological charge density $q(x, y) = (1/4\pi)\mathbf{m} \cdot (\partial_x \mathbf{m} \times \partial_y \mathbf{m})$ is asymmetric. However, the total topological charge of a single skyrmion remains constant $Q = \int q dx dy = -1$. As a comparison, Fig. 6.1(b) shows the topological charge density q for a skyrmion with radial symmetry when $H_y = 0$. Similar to the vortex [159], the distortion of the skyrmion is along the x-axis when an external field is applied in the y-direction.

Table 6.1: Unit conversion table for $J = 1$ meV, $S = 1$ and $a = 0.5$ nm.

Distance x	$\hat{x} = a$	$= 0.5$ nm
Time t	$\hat{t} = \hbar S/J$	≈ 0.66 ps
Velocity v	$\hat{v} = Ja/(\hbar S)$	$\approx 7.59 \times 10^2$ m/s
Frequency ω	$\hat{\omega} = J/(\hbar S)$	$\approx 1.52 \times 10^3$ GHz
Magnetic field H	$\hat{H} = J/(\hbar\gamma S)$	≈ 8.63 T

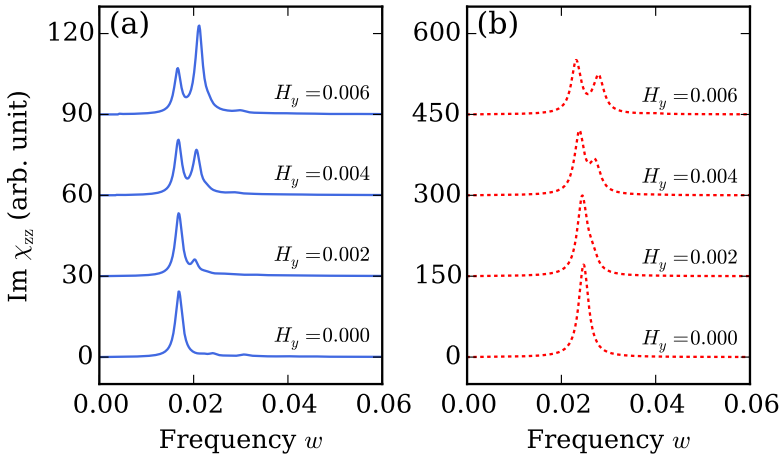

Figure 6.2: Imaginary parts of the H_y-dependent dynamical susceptibility χ_{zz} as a function of frequency for (a) a single skyrmion, and (b) a skyrmion lattice. The spectra are obtained by applying a sinc-field pulse $h = h_0\text{sinc}(\omega_0 t)$ to the system with $h_0 = 1 \times 10^{-5}$ and $\omega_0 = 0.1\pi$ in the z-axis, the magnetization dynamics is recorded every $dt = 5$ for 8000 steps.

6.3 Spin waves modes

The excitation of internal modes depends on the static external field H_z as well as the frequency and direction of microwaves [77, 151]. The typical excited modes are the clockwise/counterclockwise rotation and breathing modes [151–153]. To study how the in-plane applied field H_y affects the excitation mode of a skyrmion, we calculate the magnetic absorption spectrum of the skyrmion. After applying a sinc-function field pulse $h = h_0\text{sinc}(\omega_0 t) = h_0 \sin(\omega_0 t)/(\omega_0 t)$ to the stable skyrmion state we record the spatially averaged magnetization evolution and from that we compute the dynamic susceptibility χ via a Fourier transformation [160, 161]. For instance, the component χ_{zz} is computed using m_z when the pulse is parallel to the z-axis.

Figure 6.2 shows the imaginary part of the dynamical susceptibility χ_{zz} for a single skyrmion (a) and a skyrmion lattice (b); each calculated for different in-plane fields H_y. We see in (b) for the skyrmion lattice and $H_y = 0$ that the mode with frequency $\omega \approx 0.0246$ is dominant. This is the so-called breathing mode [151, 152]. The resonance angular frequency $\omega \approx 0.0246$ in simulation units corresponds to the frequency $f = \omega/2\pi \approx 5.95$ GHz (using $\hat{\omega}$ from Table 6.1). The breathing mode frequency decreases

slightly as the in-plane field H_y increases. A second peak emerges with increasing H_y, and the frequency of the new mode is $\omega \approx 0.0278$ when $H_y = 0.006$. Similar to the skyrmion lattice, a breathing mode with $\omega \approx 0.0168$ is found for a single skyrmion, as shown in Fig. 6.2(a). In general, the resonance frequency of a single skyrmion is lower than that for the skyrmion lattice. As for the skyrmion lattice, a new mode with frequency around 0.02 emerges for the single skyrmion case as H_y is increased. This second mode is the uniform mode with frequency $\omega = \gamma H$ where $H \simeq (H_y^2 + H_z^2)^{1/2}$ is the amplitude of the external field.

6.4 Skyrmion motion

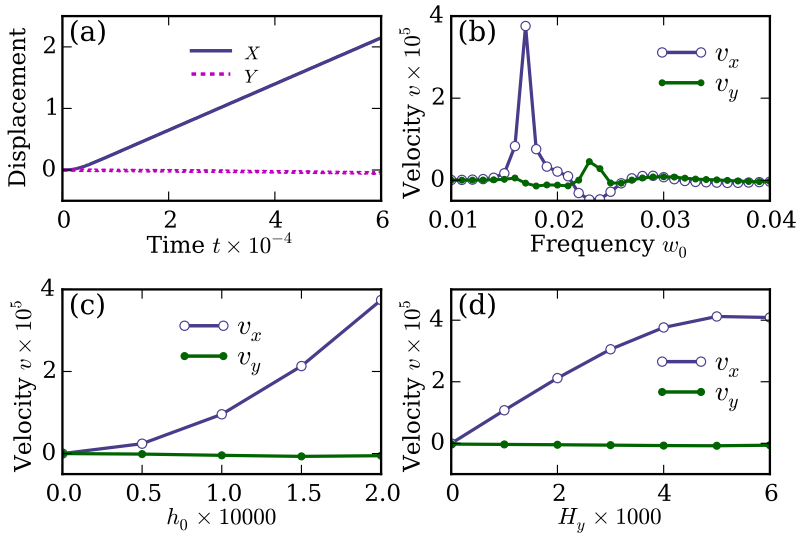

Figure 6.3: (a) The displacements of the guiding center (X, Y) for a single skyrmion. The simulation parameters are $\omega_0 = 0.017$, $h_0 = 2 \times 10^{-4}$ and the in-plane field $H_y = 0.004$. (b-d) The velocities v_x and v_y as functions of (b) the microwave frequency ω_0, (c) the microwave amplitude h_0, and (d) the in-plane field H_y. The fixed simulation parameters are the same as in (a).

In the presence of an in-plane applied field H_y, the skyrmion is deformed, as shown in Figs. 6.1(a) and 6.1(c). Therefore, instead of the geometric center we measure the so-called guiding center [162] $\mathbf{R} = (X, Y)$ of a skyrmion: $X = \int xqdxdy / \int qdxdy$ and $Y = \int yqdxdy / \int qdxdy$, where q is the topological charge density. For a symmetric skyrmion, the guiding center is the same as its geometric center. In the rest of this work, we consider the scenario that a linearly polarized microwave is applied in the z-direction, i.e., $\mathbf{h}(t) = h_0 \sin(\omega_0 t)\mathbf{e}_z$, where h_0 and ω_0 are the amplitude and frequency of the microwave, respectively.

Figure 6.3(a) shows the displacement of the guiding center for a single skyrmion with $\omega_0 = 0.017$ and in-plane field $H_y = 0.004$. The microwave amplitude is $h_0 = 2 \times 10^{-4}$,

which corresponds to 1.73 mT for $J = 1$ meV and $S = 1$. It can be seen that the x-component of the guiding center, X, changes significantly as a function of time, while the displacement of Y is relatively small. Figure 6.3(b) plots the frequency-dependent skyrmion velocity and shows that a single skyrmion has maximum velocity when $\omega_0 = 0.017$, which is the breathing mode resonance frequency. Therefore, exciting the breathing mode can move the skyrmion effectively in the presence of an in-plane field H_y. Using the conversions presented in Table I, the maximum velocity is $v_x \approx 2.8$ cm/s. While v_x is positive for frequency $\omega_0 = 0.017$, it is negative for $\omega_0 = 0.023$, where the former corresponds to the breathing mode, and the latter to coherent rotation. The relation between the velocities and the amplitude of the microwave is shown in Fig. 6.3(c), and the dependence of v_x on h_0 is nonlinear: $v_x \propto h_0^2$ which is proportional to the power of the microwaves.

Figure 6.3(d) describes the relation between the skyrmion velocity and the in-plane field H_y. The velocity is zero if $H_y = 0$, which is expected due to the symmetry of the skyrmion. The velocity of the skyrmion also depends on the direction of the in-plane field H_y: the velocity is reversed when the direction of the in-plane field is reversed. Similarly, a change in the sign of the DMI constant will also reverse the sign of the velocity, which is different from the case of driving skyrmions with spin-polarized currents, where the sign of perpendicular velocity (with respect to the current direction) of the skyrmion motion is related to the sign of topological charge rather than the DMI constant sign.

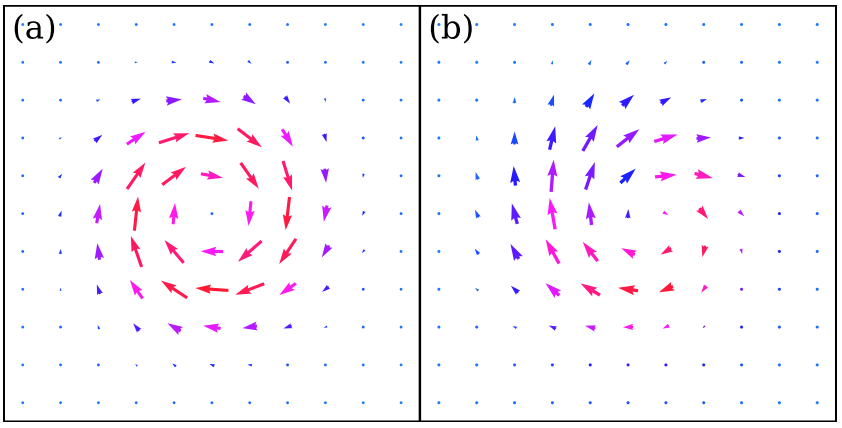

Figure 6.4: The total spatial force density $f_i = \tilde{\mathbf{m}}_s \cdot [\partial_i \tilde{\mathbf{m}}_s \times \langle \mathbf{m} \times \mathbf{H}_{\text{eff}} \rangle]$ for (a) $H_y = 0$, and (b) $H_y = 4 \times 10^{-3}$, where we have used $\tilde{\mathbf{m}}_s = \langle \mathbf{m} \rangle$. The microwave frequency is $\omega_0 = 0.017$.

To understand why the skyrmion moves in the presence of an in-plane field, we split the magnetization unit vector $\mathbf{m}$ into a slow part $\mathbf{m}_s$ and a fast part $\mathbf{n}$, i.e., $\mathbf{m} = \mathbf{m}_s + \mathbf{n}$, where the slow part represents the equilibrium profile of the skyrmion while the fast part is responsible for the excited spin wave mode [33, 163]. In the continuum approximation, the effective field is $\mathbf{H}_{\text{eff}} = \tilde{A}\nabla^2\mathbf{m} - \tilde{D}\nabla \times \mathbf{m} + \mathbf{H} + \mathbf{h}(t)$, where

$\tilde{A} = 2A/M_s$ and $\tilde{D} = 2D_a/M_s$. In the presence of the microwaves with specific frequency, bound spin-wave modes are excited, and thus we expect $\langle \dot{\mathbf{n}} \rangle = 0$ and $\langle \mathbf{n} \rangle = 0$ due to the microwave synchronization, where $T = 2\pi/\omega_0$ is the period of microwaves and the notation $\langle f \rangle = \langle f \rangle(t) \equiv T^{-1} \cdot \int_t^{t+T} f(t')dt'$ represents the time average of function $f(t)$ over a single period T. Furthermore, one obtains $\langle \mathbf{m}_s \times \dot{\mathbf{n}} \rangle \approx 0$ and $\langle \mathbf{n} \times \dot{\mathbf{m}}_s \rangle \approx 0$ since $\mathbf{m}_s$ is the slow part. Therefore, by averaging the LLG equation (6.2) over a period T we arrive at

$$\langle \dot{\mathbf{m}}_s \rangle = -\gamma \langle \mathbf{m} \times \mathbf{H}_{\text{eff}} \rangle + \alpha \langle \mathbf{m}_s \times \dot{\mathbf{m}}_s \rangle, \tag{6.3}$$

where $\langle \mathbf{n} \times \dot{\mathbf{n}} \rangle = 0$ is used since basically $\mathbf{n}$ is a sine or cosine function in time. We then consider the possible translational motion of the skyrmion such that $\mathbf{m}_s(\mathbf{r}, t) = \mathbf{m}_s(\mathbf{r} - \mathbf{v}_s t)$, i.e., $\dot{\mathbf{m}}_s = -(\mathbf{v}_s \cdot \nabla)\mathbf{m}_s$, where the skyrmion velocity $\mathbf{v}_s = d\mathbf{R}/dt$ is assumed to be a constant. If the skyrmion moves slowly, i.e., $v_s T \ll L$ (L is the typical skyrmion size), we have $\langle \dot{\mathbf{m}}_s \rangle \approx -(\mathbf{v}_s \cdot \nabla)\tilde{\mathbf{m}}_s$ (see Appendix A.3) where $\tilde{\mathbf{m}}_s = \langle \mathbf{m}_s \rangle$. Similarly, $\langle \mathbf{m}_s \times \dot{\mathbf{m}}_s \rangle \approx \tilde{\mathbf{m}}_s \times \langle \dot{\mathbf{m}}_s \rangle$, and thus Eq. (6.3) can be rewritten as

$$(\mathbf{v}_s \cdot \nabla)\tilde{\mathbf{m}}_s = \gamma \langle \mathbf{m} \times \mathbf{H}_{\text{eff}} \rangle + \alpha \tilde{\mathbf{m}}_s \times (\mathbf{v}_s \cdot \nabla)\tilde{\mathbf{m}}_s. \tag{6.4}$$

Following Thiele's approach in describing the motion of magnetic textures [164], we replace the dots in $\int \tilde{\mathbf{m}}_s \cdot (\partial_i \tilde{\mathbf{m}}_s \times \cdots) dxdy$ by Eq. (6.4) to obtain [32, 33, 163]

$$\mathbf{G} \times \mathbf{v}_s + \widehat{\mathcal{D}} \mathbf{v}_s = \mathbf{F}, \tag{6.5}$$

where $i = x, y$ and $\mathbf{G} = 4\pi Q \mathbf{e}_z$. The tensor $\widehat{\mathcal{D}}_{ij} = \alpha \eta_{ij}$ is the damping tensor in which $\eta_{ij} = \int (\partial_i \tilde{\mathbf{m}}_s \cdot \partial_j \tilde{\mathbf{m}}_s) dxdy = \delta_{ij}\eta$ is the shape factor of the skyrmion and η is close to 4π [163]. The force $\mathbf{F}$ is given by

$$F_i = -\gamma \int \tilde{\mathbf{m}}_s \cdot \left[\partial_i \tilde{\mathbf{m}}_s \times \langle \mathbf{m} \times \mathbf{H}_{\text{eff}} \rangle \right] dxdy. \tag{6.6}$$

Figure 6.4(a) and (b) depict the total spatial force density for $H_y = 0$ and $H_y = 4 \times 10^{-3}$, respectively, where we have used $\tilde{\mathbf{m}}_s = \langle \mathbf{m} \rangle$. The force density is symmetric if $H_y = 0$ and thus the total force $\mathbf{F}$ is zero. However, when H_y is nonzero the force distribution is asymmetric which results in the skyrmion motion due to the nonzero net force. For small damping $\alpha \ll 1$, we have $v_x \approx F_y/(4\pi Q)$. The total force calculated with parameters $\omega_0 = 0.017$, $H_y = 0.004$ and $h_0 = 2 \times 10^{-4}$ is $F_y = -4.7 \times 10^{-4}$, therefore, the established velocity is $v_x = 3.7 \times 10^{-5}$, which fits the simulation result ($\sim 3.8 \times 10^{-5}$) well. Similarly, for $\omega = 0.023$ using Eq. (6.6) we obtain $F_y = 5.7 \times 10^{-5}$ and find $v_x \approx -4.5 \times 10^{-6}$ from Eq. (6.5); in agreement with the simulation results (the minimum of v_x is -4.7×10^{-6}).

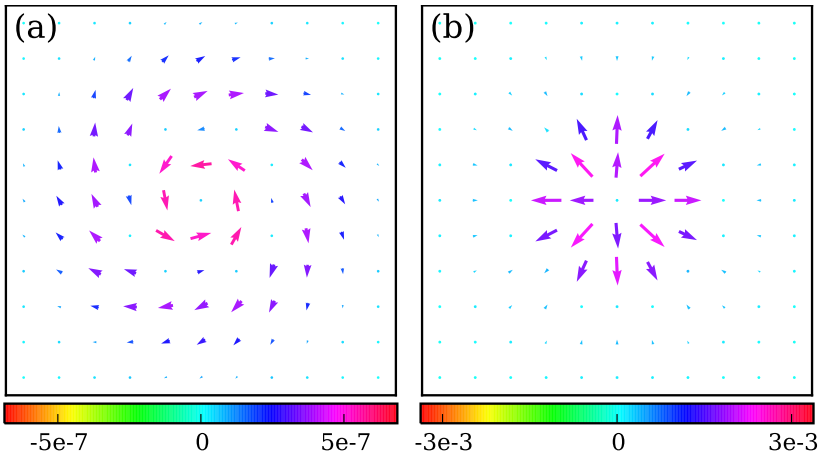

Figure 6.5: (a) The spatial force density $f_i = \tilde{\mathbf{m}}_s \cdot [\partial_i \tilde{\mathbf{m}}_s \times \langle \mathbf{m} \times \mathbf{h} \rangle]$ induced by the microwave field $\mathbf{h}$ for a symmetric skyrmion. (b) The force density $f_i = \tilde{\mathbf{m}}_s \cdot [\partial_i \tilde{\mathbf{m}}_s \times \langle \mathbf{m} \times \tilde{A} \nabla^2 \mathbf{m} \rangle]$ due the exchange interaction. The microwave frequency is $\omega_0 = 0.017$.

It is of interest to circumstantiate the contributions of the total force $\mathbf{F}$. In Appendix A.4 we show that there are three nontrivial terms

$$\langle \mathbf{m} \times \mathbf{H}_{\text{eff}} \rangle \approx \langle \mathbf{n} \times [\tilde{A} \nabla^2 \mathbf{n} - \tilde{D} \nabla \times \mathbf{n} + \mathbf{h}(t)] \rangle. \tag{6.7}$$

The exchange term $\mathbf{n} \times \tilde{A} \nabla^2 \mathbf{n}$ corresponds to magnon currents [33, 163]. Compared to the skyrmion motion induced by the temperature gradient, where the magnon current is generated by the temperature gradient, here the magnon current originates from the external microwave fields. Another difference is that in our case the contributions from DMI and microwave fields are also significant.

Figure 6.5 (a) and (b) show the spatial force densities of a symmetric skyrmion induced by the microwave field $\mathbf{h}$ and the exchange interaction, respectively. It can be found that the force density, due to the exchange interaction, is much higher than the one induced by the microwave field. Moreover, the force density due to the exchange interaction is localized at the skyrmion core, whereas it is relatively uniform for the microwave field case. However, both of them play significant roles in driving the skyrmion.

We repeat the velocity study for the skyrmion lattice. Fig. 6.6(a) plots the velocities v_x and v_y of the skyrmion lattice as functions of the in-plane external field H_y. The dependencies are similar to the single skyrmion case. The frequency-dependent velocities v_x and v_y are shown in Fig. 6.6(b). As for the single skyrmion case, the velocity peak coincides with the dominant dynamical susceptibility peak in Fig. 6.2(b).

In closing, we briefly comment on the importance of symmetry breaking in driving the skyrmions. The driving force originates from the microwave field, which is periodic in time and averages to zero. The symmetry-breaking field converts the periodic

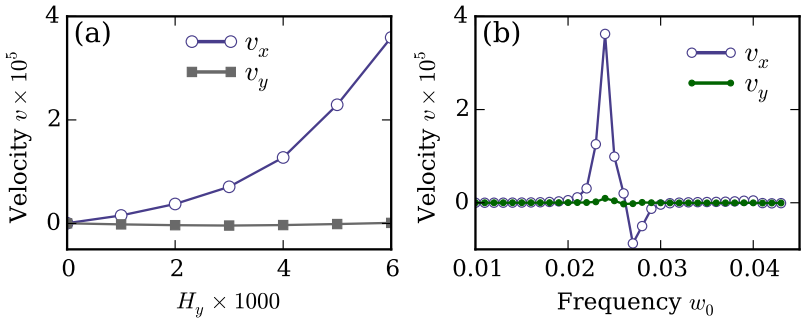

Figure 6.6: (a) The velocities v_x and v_y as a function of an in-plane field H_y for the skyrmion lattice at frequency $\omega_0 = 0.023$. (b) The velocities as a function of frequency ω_0 with $H_y = 4 \times 10^{-3}$. The microwave amplitude is $h_0 = 2 \times 10^{-4}$.

microwave field into a net force and thus moves skyrmions effectively. A related field with periodic driving forces is that of ratchet-like transport phenomena [165–167], where the net motion is obtained by breaking the spatial symmetry [165] or temporal symmetry [167]. We also note that preliminary simulation results suggest that for magnon-driven skyrmions [51, 81] the introduction of a symmetry-breaking in-plane field affects the skyrmion motion and changes the Hall angle significantly.

6.5 Summary

In summary, we have studied the skyrmion dynamics driven by microwaves in the presence of an in-plane external field. We found that both a single skyrmion and a skyrmion lattice can be moved by a linearly polarized microwave field if the axial symmetry of skyrmions is slightly broken. The net velocity of the skyrmion depends on the frequency and amplitude of the microwave fields as well as the strength of the in-plane field. The maximum velocity is found where the frequency of the microwave coincides with the resonance frequency of the breathing mode of the skyrmions. These results suggest a novel method for skyrmion manipulation using microwaves fields.

Chapter 7

Conclusion and Outlook

7.1 Conclusion

A phenomenological equation called the Landau-Lifshitz-Baryakhtar (LLBar) equation was derived by Baryakhtar. The LLBar equation could be viewed as the combination of Landau-Lifshitz (LL) equation and an extra “exchange damping" term. We explain the “exchange damping" in the LLBar equation as a nonlocal damping by linking it to the spin current pumping. Using the micromagnetic simulation based on the LLBar equation, we show that the difference between magnetization length M and M_e reaches its maximum at the domain-wall center. For the cases $\chi \sim \alpha$ where χ is the longitudinal magnetic susceptibility and α is the Gilbert damping, the Walker breakdown field increases significantly. By using a 1D domain-wall model, we show that both the domain-wall mobility and the Walker breakdown field are strongly influenced by the nonlocal damping as well.

Magnon-driven domain-wall (DW) motion was firstly investigated using micromagnetic simulations [115], and the DW motion direction is found to be the same as the propagation direction of spin waves. Later, the magnonic spin-transfer torque that drives a DW to the opposite direction of spin-wave propagation was studied [127]. We have studied the DW motion induced by spin waves in the presence of Dzyaloshinskii-Moriya Interaction (DMI). We found that the DMI exerts an extra torque which rotates the DW plane when the spin wave passes through the DW. This torque represents a linear momentum exchange between the spin wave and the DW. This linear momentum exchange between spin waves and DW exists in addition to the angular momentum exchange, and is more efficient in moving the DW.

Magnetic skyrmions can be moved by spin-polarized currents [48, 49, 132, 147], magnetic or electric field gradients [32, 50], magnons [51, 81, 150], and temperature gradients [33, 148, 149]. We have studied the skyrmion dynamics driven by microwaves in

the presence of an in-plane external field. We found that both a single skyrmion and a skyrmion lattice can be moved by a linearly polarized microwave field if the axial symmetry of skyrmions is broken. The net velocity of the skyrmion depends on the frequency and amplitude of the microwave field as well as the in-plane field strength. The maximum velocity is found where the frequency of the microwave coincides with the resonance frequency of the breathing mode of the skyrmions.

7.2 Outlook

We have started to use discontinuous Galerkin (DG) methods in micromagnetics. Typical energies such as the magnetocrystalline anisotropy and Zeeman field are straightforward to be implemented. We will develop new method based on DG space to compute the demagnetizing field. In addition, the current development on the magnonic crystals are mainly one- or two-dimensional, which suggests us to develop two-dimensional finite element tools based on the triangular prisms.

Both the LLBar and the simplified LLBar (sLLBar) equations are supported in Fidimag. Simulations based on Fidimag with extended nonlocal damping could be performed to study the related phenomena such as the FMR linewidth and dynamic magnetic susceptibility. We will try to do simulations about nonlocal damping to compare them with the recent experimental reports [41].

It is very interesting that both the magnetic domain wall and magnetic skyrmion move to the hotter side from the cooler side rather than the inversed direction. This phenomenon actually is consistent with the spin-transfer effect of magnons [31, 127]. More precisely, the temperature gradient yields a magnon flow from the hotter to the cooler side, when the magnons pass through the domain wall, the magnons transfer spin angular momentums to it and thus the domain wall moves to the hotter area. On the other hand, positive velocities of domain-wall motion have been found in micromagnetic simulations [115]. The positive velocities are explained by the spin-wave reflection which could happen when the domain-wall width is very thin [138] or in the presence of dipolar interactions [36]. Moreover, we have found that the domain-wall velocity also could be positive even without the spin-wave reflection in the presence of DMI. We will study whether a domain wall could move to the cooler area using Fidimag.

The relation between the Gilbert damping α and the stochastic field in the stochastic Landau-Lifshitz-Gilbert (SLLG) equation is determined by Eq. (2.33), which can be derived by comparing the SLLG equation and the Fokker-Planck equation in thermal equilibrium [65]. However, a more general case is the nonequilibrium problem, such as the ultrafast demagnetization [168]. A key ingredient to treat the system in the far-from-equilibrium regime is the fluctuation theorem (FT) [169, 170]. We will try to explore this area related to the SLLG equation using the fluctuation theorem.

Appendix A

A.1 Section A

In this section, we will show how the spin current is related to the tensor form [Eq. (4.15)]. We split the perpendicular spin current $\mathbf{j}_{\perp,i}$ into two components,

$$\mathbf{j}_{\perp,i} = \mathbf{j}_i^a + \mathbf{j}_i^b, \tag{A.1}$$

where we write λ_e/γ as $\tilde{\sigma}$, and

$$\mathbf{j}_i^a = -\tilde{\sigma}(\partial_i \mathbf{m} \times \partial_t \mathbf{m}), \qquad \mathbf{j}_i^b = -\tilde{\sigma}(\mathbf{m} \times \partial_i \partial_t \mathbf{m}). \tag{A.2}$$

The torque $\boldsymbol{\tau}_a$ generated by spin current $\mathbf{j}_i^a$ is given by $\boldsymbol{\tau}_a = (\partial_i \mathbf{j}_i^a)_\perp$, i.e.,

$$\boldsymbol{\tau}_a = \tilde{\sigma}\mathbf{m} \times [\partial_i \mathbf{m} \times (\partial_t \mathbf{m} \times \partial_i \mathbf{m})], \tag{A.3}$$

where we have used the identities $\mathbf{m} \cdot \partial_i \partial_t \mathbf{m} = -\partial_i \mathbf{m} \cdot \partial_t \mathbf{m}$ and $\mathbf{m} \cdot \partial_i \partial_i \mathbf{m} = -\partial_i \mathbf{m} \cdot \partial_i \mathbf{m}$. Meanwhile, the corresponding torque $\boldsymbol{\tau}_b$ can be computed by $\boldsymbol{\tau}_b = (\partial_i \mathbf{j}_i^b)_\perp$, which gives

$$\boldsymbol{\tau}_b = \boldsymbol{\tau}_a - \tilde{\sigma}(\partial_i \mathbf{m} \cdot \partial_i \mathbf{m})\mathbf{m} \times \partial_t \mathbf{m} - \tilde{\sigma}\mathbf{m} \times \nabla^2 \partial_t \mathbf{m}. \tag{A.4}$$

Note that $\boldsymbol{\tau}_a = \tilde{\sigma}\partial_i \mathbf{m}[(\partial_t \mathbf{m} \times \partial_i \mathbf{m}) \cdot \mathbf{m}]$ can be changed into the tensor form,

$$\boldsymbol{\tau}_a = \mathbf{m} \times (\mathcal{D}^0 \cdot \partial_t \mathbf{m}), \tag{A.5}$$

where

$$\mathcal{D}^0_{\alpha\beta} = \tilde{\sigma}(\mathbf{m} \times \partial_i \mathbf{m})_\alpha (\mathbf{m} \times \partial_i \mathbf{m})_\beta. \tag{A.6}$$

Therefore, we obtain for $\boldsymbol{\tau}_a + \boldsymbol{\tau}_b$,

$$\boldsymbol{\tau}_a + \boldsymbol{\tau}_b = \mathbf{m} \times (\mathcal{D} \cdot \partial_t \mathbf{m}) - \tilde{\sigma}\mathbf{m} \times \nabla^2 \partial_t \mathbf{m}, \tag{A.7}$$

where $\mathcal{D}$ is a 3×3 tensor,

$$\mathcal{D}_{\alpha\beta} = 2\tilde{\sigma}(\mathbf{m} \times \partial_i \mathbf{m})_\alpha (\mathbf{m} \times \partial_i \mathbf{m})_\beta - \tilde{\sigma}(\partial_i \mathbf{m} \cdot \partial_i \mathbf{m})\delta_{\alpha\beta}. \tag{A.8}$$

A.2 Section B

We introduce a new variable $\mathbf{s}$ to represent the second term in the (4.23), i.e., $\mathbf{s} = \mathbf{m}_0 e^{i(\tilde{k}x - \omega t)}$, so we have

$$\begin{aligned} &\mathbf{m} = \mathbf{e}_x + \mathbf{s}, \\ &\frac{d\mathbf{m}}{dt} = -i\,\omega\,\mathbf{s}, \\ &\mathbf{H}_{\text{eff}} = H_s(1 + s'_x)\mathbf{e}_x - D\tilde{k}^2\mathbf{s}, \end{aligned} \tag{A.9}$$

where $s'_x \approx (1/2)(s_x^2 - s^2)$. Considering the fact $|\mathbf{s}| \ll 1$ and neglect the high order term s^2, one obtains $\mathbf{H}^{\perp}_{\text{eff}} = -(H_s + D\tilde{k}^2)\mathbf{s}$ and thus

$$\mathbf{H}^{b}_{\text{eff}} = c\,\mathbf{e}_x + d\,\mathbf{s}, \tag{A.10}$$

where

$$c = \alpha H_s(1 + s'_x), \qquad d = -\beta G\tilde{k}^2(D\tilde{k}^2 + H_s) - \alpha D\tilde{k}^2. \tag{A.11}$$

Substituting the above equations into (4.17), we have

$$\frac{i\omega}{\gamma}\begin{bmatrix} s_x \\ s_y \\ s_z \end{bmatrix} = f\begin{bmatrix} 0 \\ s_z \\ -s_y \end{bmatrix} + (c - d)\begin{bmatrix} -(s_y^2 + s_z^2) \\ (1 + s_x)s_y \\ (1 + s_x)s_z \end{bmatrix}, \tag{A.12}$$

where $f = H_s(1 + s'_x) + D\tilde{k}^2$. Neglecting high order terms such as s_x^2 and $s_x s_y$ we obtained,

$$\begin{bmatrix} \gamma(\alpha H_s - d) - i\omega & \tilde{w}_0 \\ -\tilde{w}_0 & \gamma(\alpha H_s - d) - i\omega \end{bmatrix}\begin{bmatrix} s_y \\ s_z \end{bmatrix} = \begin{bmatrix} 0 \\ 0 \end{bmatrix}. \tag{A.13}$$

Therefore, Eq. (4.27) can be obtained by setting the determinant of the matrix in (A.13) to zero.

A.3 Section C

In this section, we will present an argument for the result $\langle \dot{\mathbf{m}}_s \rangle \approx -(\mathbf{v}_s \cdot \nabla)\tilde{\mathbf{m}}_s$. Assume that a well-behaved function $f(x,t) = f(x - vt)$ describes the dynamics of a soliton where v is a constant. As we can see, f satisfies $\dot{f} = -vf'$. For given time T, if $vT \ll L$ where L is the typical size of the soliton (for example, L could be the domain wall width

for a magnetic domain wall), we can find that

$$\langle \dot{f} \rangle(0) = \frac{1}{T}\int_0^T \dot{f} dt = \frac{1}{T}[f(x - vT) - f(x)] \approx -vf'(x - vT/2), \tag{A.14}$$

where we have used the Taylor series for $f(x)$ and $f(x - vT)$:

$$f(x) \approx f(x - vT/2) + f'(x - vT/2)vT/2 \tag{A.15}$$

$$f(x - vT) \approx f(x - vT/2) - f'(x - vT/2)vT/2. \tag{A.16}$$

Similarly, we can see that $\tilde{f}_0 \equiv \langle f \rangle(0) \approx f(x - vT/2)$ and thus we have $\langle \dot{f} \rangle(0) \approx -v\tilde{f}_0$. This relation actually holds for arbitrary t

$$\langle \dot{f} \rangle \approx -v\tilde{f}. \tag{A.17}$$

A.4 Section D

In this section we will show the three nontrivial terms of the total force. By using the effective field explicitly and noticing that $\mathbf{m} = \mathbf{m}_s + \mathbf{n}$, the term $\langle \mathbf{m} \times \mathbf{H}_{\text{eff}} \rangle$ can be split into four parts

$$\langle \mathbf{m} \times \mathbf{H}_{\text{eff}} \rangle = \langle T_1 + T_2 + T_3 + T_4 \rangle, \tag{A.18}$$

where $T_1 = \mathbf{n} \times [\tilde{A}\nabla^2\mathbf{n} - \tilde{D}\nabla \times \mathbf{n} + \mathbf{h}(t)]$ is shown in Eq. (6.7), $T_2 = \mathbf{m}_s \times (\tilde{A}\nabla^2\mathbf{m}_s - \tilde{D}\nabla \times \mathbf{m}_s + \mathbf{H})$, $T_3 = \mathbf{n} \times (\tilde{A}\nabla^2\mathbf{m}_s - \tilde{D}\nabla \times \mathbf{m}_s + \mathbf{H})$ and $T_4 = \mathbf{m}_s \times [\tilde{A}\nabla^2\mathbf{n} - \tilde{D}\nabla \times \mathbf{n} + \mathbf{h}(t)]$. We expect $T_2 = 0$ since $\mathbf{m}_s$ represents the equilibrium state of the skyrmion. For the slow skyrmion motion, replacing $\mathbf{m}_s$ by $\tilde{\mathbf{m}}_s$ and noticing that $\langle \mathbf{n} \rangle = 0$, we obtain $\langle T_3 \rangle \approx \langle \mathbf{n} \rangle \times (\tilde{A}\nabla^2\tilde{\mathbf{m}}_s - \tilde{D}\nabla \times \tilde{\mathbf{m}}_s) = 0$ and $\langle T_4 \rangle \approx \tilde{\mathbf{m}}_s \times \langle \tilde{A}\nabla^2\mathbf{n} - \tilde{D}\nabla \times \mathbf{n} + \mathbf{h}(t) \rangle = 0$. In this slow motion approximation, the fast part $\mathbf{n}$ can be computed as $\mathbf{n} \approx \mathbf{m} - \langle \mathbf{m} \rangle$.

Appendix B

Using discontinuous Galerkin Methods

B.1 Introduction

The exchange field in micromagnetics can be computed using

$$\mathbf{H}_{\text{exch}} = \frac{2A}{\mu_0 M_s} \nabla^2 \mathbf{m}, \tag{B.1}$$

where $\mathbf{m}$ is the magnetization unit vector field and A is the exchange stiffness. The key operator in Eq. (B.1) is the Laplacian (Laplace operator). Consequently, for the given unstructured mesh, we assume that the saturation magnetization M_s is constant through all cells for both the continuous Galerkin (CG) and discontinuous Galerkin (DG) methods. However, in the DG method, the problem is to how to compute the Laplace operator in a DG space of zero order (DG0). The lowest space (zero order, DG0 space) will be used since the LLG equation will be integrated at the center of cells.

B.2 Laplace operator using CG method

Let us start from the divergence theorem

$$\int_\Omega \nabla \cdot \mathbf{F} dx = \int_{\partial\Omega} \mathbf{F} \cdot \mathbf{n}\, dS. \tag{B.2}$$

Substituting $\mathbf{F} = v\nabla u$ into the divergence theorem one gets

$$\int_\Omega v\nabla^2 u\, dx = \int_{\partial\Omega} v\nabla u \cdot \mathbf{n}\, dS - \int_\Omega \nabla u \cdot \nabla v\, dx \tag{B.3}$$

where v is a test function, and at the boundary $v = 0$. Hence we have

$$\int_\Omega v\nabla^2 u\, x = -\int_\Omega \nabla u \cdot \nabla v\, dx. \tag{B.4}$$

The function u can be represented by the basis functions, namely, $u = \sum_i u_i\phi_i$. Thus, we obtain

$$\int_\Omega v\nabla^2 u\, dx = -\sum_i u_i \int_\Omega \nabla\phi_i \cdot \nabla v\, dx. \tag{B.5}$$

If we suppose that $\nabla^2 u$ is constant over the local elements and set $v = \phi_j$, we have

$$\nabla^2 u \int_\Omega \phi_j\, dx = -\sum_i u_i K_{ij}, \tag{B.6}$$

where $K_{ij} = \int_\Omega \nabla\phi_i \cdot \nabla\phi_j\, dx$. Note that $K_{ij} = K_{ji}$, therefore the right hand side of the Eq. (B.6) is the stiffness matrix K multiplying the coefficient of basis function U, and the left hand side in fact is the so-called load vector L. In the matrix form we have

$$\nabla^2 u = L^{-1}KU. \tag{B.7}$$

This is the so-called box method. This method scales with $O(h^2)$ for regular meshes but could be worse than $O(h)$ for unstructured meshes [27]. Before we start to use the DG method, we show some brief background about the Brezzi-Douglas-Marini (BDM) space.

B.3 Background

B.3.1 H(div) space

For an open domain $\Omega \in \mathbb{R}^n$, the Sobolev space $H^m(\Omega)$ is defined by [171]

$$H^m(\Omega) = \{v \in L^2(\Omega) : D^\alpha \in L^2(\Omega)\}, \tag{B.8}$$

where $L^2(\Omega)$ is the abbreviation of $L^2(\Omega, \mathbb{R}^n)$ which denotes the space of square-integrable vector fields on Ω, D^α is the standard differential operator on smooth v for multi-index α. The space $H(\mathrm{div}, \Omega)$ is defined by

$$H(\mathrm{div}, \Omega) = \{v \in (L^2(\Omega))^d : \mathrm{div}\ v \in L^2(\Omega)\}, \tag{B.9}$$

where $\mathrm{div}\, v = \sum_{i=1}^n \partial_{x_i} v_i$. The $H(\mathrm{div})$ space is particularly suitable for the partial differential equations in mixed formulations.

B.3.2 BDM space

Let us first have a look at the BDM space on triangles, which is defined by

$$V_h(K) = (P_r(K))^2, \tag{B.10}$$

where $V_h(K)$ is the restriction of V_h to triangle K and $P_r(K)$ is the space of polynomials of degree at most r on K. The lowest order of BDM space in triangles is,

$$V_h(K) = \{v : v = (a_1 + a_2x + a_3y, a_4 + a_5x + a_6y), a_i \in R\}. \tag{B.11}$$

So, its dimension is six. The degrees of freedom are the values of normal components at two points on each edge, such as in Dolfin the two points are chosen as $1/3$ and $2/3$.

B.3.3 Piola mapping

Suppose $K = F(\hat{K})$ is a smooth mapping and $DF(\hat{x})$ is the Jacobian matrix which is invertible, thus one has,

$$DF^{-1}(x) = (DF(\hat{x}))^{-1}. \tag{B.12}$$

A simple case is the affine mapping

$$F(\hat{x}) = x_0 + A\hat{x}, \tag{B.13}$$

where $DF(\hat{x}) = A$ is a constant matrix. For a function $\hat{v}(\hat{x})$ defined on $\hat{K}$, the corresponding function $v(x)$ on K can be obtained using the mapping $\mathcal{F}$

$$v = \mathcal{F}(\hat{v}) = \hat{v} \circ F^{-1}. \tag{B.14}$$

In general $\mathcal{F}$ does not preserve continuity of normal trace, that's why we need the Piola mapping. The contravariant Piola mapping $\mathcal{F}^{div}$ is defined by

$$\mathcal{F}^{div}(\hat{\sigma}) = \frac{1}{|\det J|} J\, \hat{\sigma} \circ F^{-1}, \tag{B.15}$$

where J denotes the Jacobian matrix $DF(\hat{x})$. Under the affine transformation, we can check that for any edge e the contravariant Piola mapping has

$$||e||\mathbf{v} \cdot \mathbf{n} = ||\hat{e}||\hat{\mathbf{v}} \cdot \hat{\mathbf{n}}. \tag{B.16}$$

Therefore, the $\mathcal{F}^{div}$ mapping preserves the normal trace up to edge length. Furthermore, there are two appropriate ways to define the basis functions. Suppose $\mathbf{v}$ is a basis function, one choice is using $||e||\mathbf{v} \cdot \mathbf{n} = 1$ and the other is $\mathbf{v} \cdot \mathbf{n} = 1$. Recall that we are going to assemble the matrix A and B [Eqs.(B.21) and (B.22)], both could be approached

```
import dofin as df

BDM = df.FunctionSpace(mesh, "BDM", 1)
DG = df.FunctionSpace(mesh, "DG", 0)

sigma = df.TrialFunction(BDM)
tau = df.TestFunction(BDM)

u = df.TrialFunction(DG)
v = df.TestFunction(DG)

a0 = df.dot(sigma, tau) * df.dx
A = df.assemble(a0)

a1 = - (df.div(tau) * u) * df.dx
K1 = df.assemble(a1)

a2 = (df.div(sigma) * v) * df.dx
K2 = df.assemble(a2)
```

Table B.1: Python codes to compute the matrices in BDM space.

by integration in a reference element,

$$\int_K \sigma \cdot \tau \, \mathrm{d}x = \int_{\hat{K}} \mathcal{K} \, \hat{\sigma} \cdot \hat{\tau} \, \mathrm{d}\hat{x}, \tag{B.17}$$

$$\int_K \nabla \cdot \sigma v \, \mathrm{d}x = \int_{\hat{K}} \nabla \cdot \hat{\sigma} \hat{v} \, \mathrm{d}\hat{x}, \tag{B.18}$$

where

$$\mathcal{K} = \frac{1}{|\mathrm{det} J|} J^T J. \tag{B.19}$$

B.4 Using BDM space

The BDM space provides a vector space so that the global divergences are well defined. As we have already seen, our task actually is to find an accurate flux, $\sigma = \nabla u$, where u is one component of magnetization $\mathbf{m}$. By multiplying the test function τ defined in the BDM space Σ we arrive at the following variational formulation:

$$\int_\Omega \sigma \cdot \tau \, dx = \int_\Gamma \tau \cdot n \, dS - \int_\Omega \nabla \cdot \tau \, u \, dx \quad \forall \tau \in \Sigma. \tag{B.20}$$

The boundary condition is the Neumann condition such that $\sigma \cdot n = 0$, and we need to apply the boundary condition in the function space which could be implemented using the Dirichlet boundary condition. Assembling the system results in the matrix form

$$A \, \sigma = K_1 m. \tag{B.21}$$

With known A, K_1 and m, σ this could be approached by solving linear equations. However, the computation of exchange fields is needed in each time step of the dynamics.

Therefore, it is better to inverse the matrix A and in general we will get a dense matix A^{-1}. In this case, the matrix form of Laplace operator D can be written as

$$D = K_2 A^{-1} K_1, \tag{B.22}$$

where K_2 is the matrix form of the divergence operator for BDM space, and the boundary condition could be achieved by modifying the product of A^{-1} and K_1. Table B.1 shows piece of code to compute the matrices. If we write the matrix K_2 as B, the matrix K_1 is the transpose of matrix B with a minus sign, so we have

$$D = -BA^{-1}B^T. \tag{B.23}$$

In practice, D is not a sparse matrix but in theory D should contain many fairly small entries so that we could abandon them. Although this is a possible way to sparse the matrix D, the whole process is not perfect – need to inverse the matrix A and in general A^{-1} is dense. If we keep in mind that our ultimate aim is to compute the Laplace operator which should be defined locally, we should be able to obtain a sparse inverse matrix A^{-1} using another methods.

B.5 MFMFE

We are looking for some methods that lead to a sparse A^{-1}. The multipoint flux mixed finite element method (MFMFE) [172] satisfy this condition and it is a superconvergence (second-order convergence) method. The MFMFE is related to the multipoint flux approximation (MPFA) method which has been developed as a finite volume method. The basic idea of MFMFE is using a quadrature rule to assemble the matrix A, rather than the inner product defined in BDM space. The quadrature rule is defined by,

$$(\sigma, \tau)_K = (\mathcal{K}\hat{\sigma}, \hat{\tau})_{\hat{K}} = \frac{|K|}{s} \sum_{i=1}^{s} \mathcal{K}(\hat{r}_i)\hat{\sigma}(\hat{r}_i) \cdot \hat{\tau}(\hat{r}_i), \tag{B.24}$$

where $s = 3$ for the unit triangle and $s = 4$ for the unit tetrahedron, $(\cdot, \cdot)$ represents the inner product and $\hat{\sigma}(\hat{r}_i)$ is the corner vector associated with vertex located at $\hat{r}_i$. The quadrature rule localizes the basis functions interaction and thus MFMFE could be reduced to the cell-centered stencil.

B.6 A Test

To check the performance of the implemented method and and the so-called "box method" (CG method), we compare them using an unstructured mesh. Figure B.1

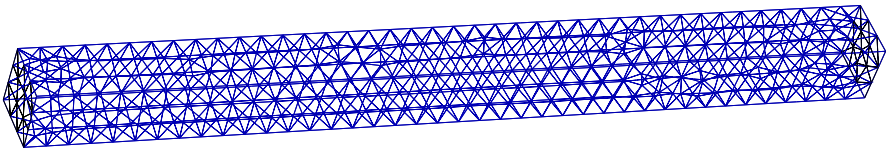

Figure B.1: The mesh used for comparison the exchange fields calculation for DG and CG methods.

presents an unstructured mesh with dimensions $100 \times 8 \times 8$ nm^3. The magnetization configuration is $\mathbf{m}_0 = (0, \sin(2\pi x/L), \cos(2\pi x/L))$ with $L = 100$ nm.

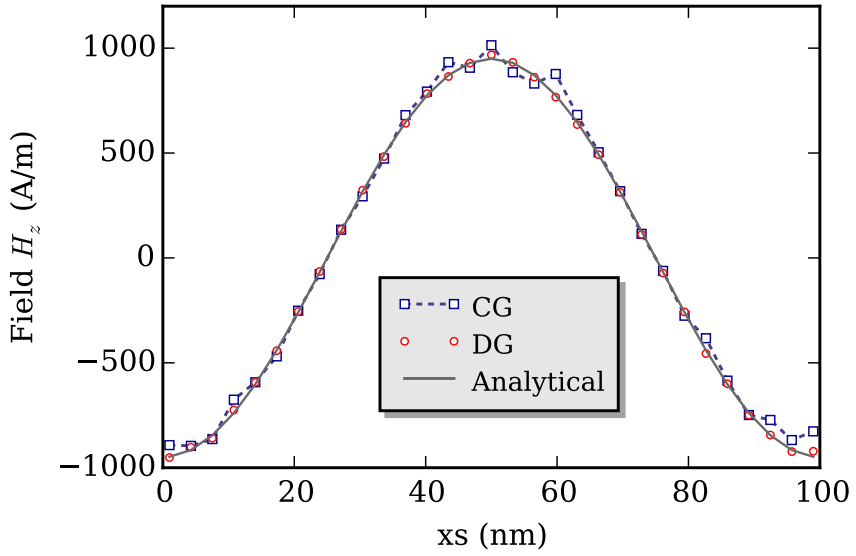

Figure B.2: The computed exchange fields using DG and CG methods. The shown data is extracted in a line with $y = z = 7$ nm.

Figure B.2 shows the z-component of the computed exchange fields for DG and CG methods. The used parameters are exchange constant $A = 1.3 \times 10^{-11}$ J/m and the saturation magnetization $M_s = 8.6 \times 10^5$ A/m. For comparison, we have mapped the data in DG space to CG space. As we can see, the DG method gives a better result.

Appendix C

Treecode for Boundary Element Method

C.1 General problem

The dipolar interaction is a long range interaction. A more general summation problem involving with interactions between N_s source particles $\{\mathbf{y}_i\}$ and N_t target particles $\{\mathbf{x}_j\}$ is

$$f(x_j) = \sum_{i=0}^{N_s-1} \alpha_i \phi(\mathbf{x}_j - \mathbf{y}_i), \tag{C.1}$$

where $j = 0, \ldots, N_t - 1$ and ϕ is a smooth radially symmetric function such that

$$\phi(\mathbf{x}_j - \mathbf{y}_i) = \frac{1}{|\mathbf{x}_j - \mathbf{y}_i|}. \tag{C.2}$$

A direct approach requires $O(N^2)$ computation time which is unacceptable for large system. A relatively easy and efficient method is the Treecode method, which scales with $O(N \log(N))$.

C.2 Treecode

The revolutionizing treecode method for the fast computation only requires $O(N \log(N))$ operations and it was first employed to speed up the n-body gravity force calculation [173]. The crucial idea is to replace the particle-particle interactions by particle-cluster interactions. To achieve this aim, a regular octree can be used to group the nearby bodies hierarchically, then a divide-and-conquer strategy can be applied to travel the tree from its root for every observation particle. Treecode method is easier than the fast multipole method (FMM), and the whole process can be done recursively.

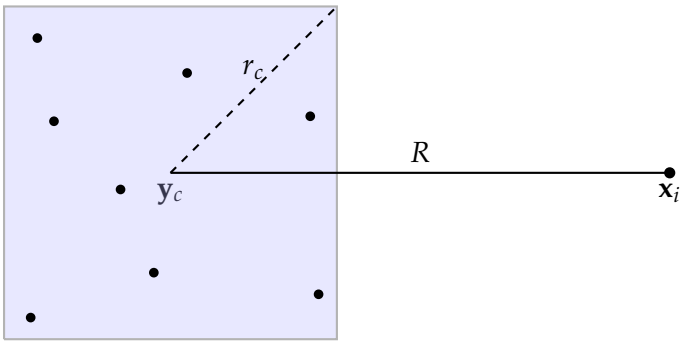

Figure C.1: The particle-cluster interaction between target particle $\mathbf{x}_i$ and cluster $c = \{\mathbf{y}_j\}$, where $\mathbf{y}_c$ is the cluster center, R is the distance between cluster and target particle, r_c is the radius of the cluster.

C.2.0.1 Particle-cluster interactions

In this part, we provide necessary equations to implement the treecode algorithm [174], where Cartesian multi-index notation is used to simplify the formalism:

$$\begin{aligned} \mathbf{k} &= (k_1, k_2, k_3), \qquad ||\mathbf{k}|| = k_1 + k_2 + k_3, \\ \mathbf{k}! &= k_1! k_2! k_3!, \qquad D_{\mathbf{y}}^{\mathbf{k}} = D_{y_1}^{k_1} D_{y_2}^{k_2} D_{y_3}^{k_3}. \end{aligned} \tag{C.3}$$

Suppose that the particles are already being divided into clusters, so the potential for target particle $\mathbf{x}_i$ induced by clusters is

$$V_i = \sum_c V_{i,c}, \tag{C.4}$$

where

$$V_{i,c} = \sum_{\mathbf{y}_j \in c} q_j \phi(\mathbf{x}_i - \mathbf{y}_j) \tag{C.5}$$

is the interaction between the target particle and cluster $c = \{\mathbf{y}_j\}$ [174]. As shown in Figure C.1, the target particle and the cluster are well separated with distance R, and r_c is the maximum radius of the cluster. Equation (C.5) is the direct sum of particle-particle interactions without any speedup. However, ϕ can be expanded in Taylor series with respect to $\mathbf{y}$ around $\mathbf{y}_c$ since target particle and cluster are well separated:

$$\phi(\mathbf{x}_i, \mathbf{y}_j) = \sum_{||\mathbf{k}||=0} \frac{1}{\mathbf{k}!} D_{\mathbf{y}}^{\mathbf{k}} \phi(\mathbf{x}_i, \mathbf{y}_c)(\mathbf{y}_j - \mathbf{y}_c)^{\mathbf{k}}, \tag{C.6}$$

where the notation (C.3) is used. The interval of convergence for Taylor series (Eq. (C.6)) is $R > r_c$, which is a far-field expansion that corresponds to the far-field spherical

multipole expansion in FMM [174]. Substituting Eq. (C.6) into Eq. (C.5), one obtains

$$\begin{aligned} V_{i,c} &= \sum_{||\mathbf{k}||=0} \frac{1}{\mathbf{k}!} D_{\mathbf{y}}^{\mathbf{k}} \phi(\mathbf{x}_i, \mathbf{y}_c) \sum_{\mathbf{y}_j \in c} q_j (\mathbf{y}_j - \mathbf{y}_c)^{\mathbf{k}} \\ &\approx \sum_{||\mathbf{k}||=0}^{p} a^{\mathbf{k}}(\mathbf{x}_i, \mathbf{y}_c) m_c^{\mathbf{k}}, \end{aligned} \tag{C.7}$$

where

$$a^{\mathbf{k}}(\mathbf{x}_i, \mathbf{y}_c) = \frac{1}{\mathbf{k}!} D_{\mathbf{y}}^{\mathbf{k}} \phi(\mathbf{x}_i, \mathbf{y}_c) \tag{C.8}$$

is the Taylor coefficient and

$$m_c^{\mathbf{k}} = \sum_{\mathbf{y}_j \in c} q_j (\mathbf{y}_j - \mathbf{y}_c)^{\mathbf{k}} \tag{C.9}$$

is the kth moment of the cluster and p is the truncation order.

C.2.0.2 Recurrence relations of Taylor coefficients

Recurrence relations are simple and efficient compared to the explicit formulas [174]. Let us start with

$$|\mathbf{x} - \mathbf{y}| \phi = 1, \tag{C.10}$$

which is the definition of the magnetic potential. By applying D_{y_1} we arrive at

$$|\mathbf{x} - \mathbf{y}|^2 D_{y_1} \phi - (x_1 - y_1)\phi = 0. \tag{C.11}$$

Next, applying the operator $D_{y_1}^{k_1 - 1}$ and using Leibnitz's rule for repeated differentiation of the product, which yields [174]

$$|\mathbf{x} - \mathbf{y}|^2 D_{y_1}^{k_1} \phi - (2k_1 - 1)(x_1 - y_1) D_{y_1}^{k_1 - 1} \phi + (k_1 - 1)^2 D_{y_1}^{k_1 - 2} \phi = 0 \tag{C.12}$$

where identities $D_{y_1} |\mathbf{x} - \mathbf{y}|^2 = 2(y_1 - x_1)$, $D_{y_1}^2 |\mathbf{x} - \mathbf{y}|^2 = 2$ and $D_{y_1}^k |\mathbf{x} - \mathbf{y}|^2 = 0$ if $k > 2$ are used. Then, applying the operator $D_{y_2}^{k_2} D_{y_3}^{k_3}$, dividing by $\mathbf{k}!$ and substituting the definition of $a^{\mathbf{k}}$,

$$|\mathbf{x} - \mathbf{y}|^2 a^{\mathbf{k}} - 2 \sum_{i=1}^{3} a^{\mathbf{k} - \mathbf{e}_i} + \sum_{i=1}^{3} a^{\mathbf{k} - 2\mathbf{e}_i} + \frac{1}{k_1} ((x_1 - y_1) a^{\mathbf{k} - \mathbf{e}_i} - a^{\mathbf{k} - 2\mathbf{e}_i}) = 0, \tag{C.13}$$

where $\mathbf{e}_i$ are standard Cartesian basis. Another two similar equations can be obtained by permuting indices, summing these equations leads to a symmetric one. In practice, Eq. (C.13) is used to reduce calculation time slightly [174].

Data: Source positions $\mathbf{y}_j$, target positions $\mathbf{x}_i$, source particles weights w_j.
Data: User input Taylor degree p, θ and N_0.
Build Tree;
foreach x in $\{\mathbf{x}_i\}$ **do**:
  compute_potential(x,root);
end

function *compute_potential*(x,root):
if θ is satisfied **then**:
  calculate the moment of tree if needed;
  calculate particle-cluster interaction using Taylor expansion;
else:
  if tree has children **then**:
    foreach c in children **do**:
      compute_potential(x,c);
    end
  else:
    calculate particle-cluster interaction using direct summation;
  end
end

Table C.1: The algorithm of treecode method.

C.2.0.3 Implementation of Treecode

A hierarchy tree must be built to trigger the Treecode method. The particles are stored into an octree recursively, at each level the space are divided into eight subspaces (four or two subspaces are used as well to avoid very narrow subspaces) until the number of particles is smaller than a user-specified number N_0. The root cell is the smallest rectangular box that contains all particles. In practice, both the particle coordinates and charges are stored in linear array, which are rearranged so that in each cell the particles indices are stored to a chunk in an array.

There are two options to compute the particle-cluster interaction, i.e., through Taylor expansion [Eq. (C.7)] or the direct summation using Eq. (C.5). The criterion used here is the so-called multipole acceptance criterion (MAC): the Taylor approximation only being employed if the following relation holds

$$\frac{r_c}{R} \leqslant \theta, \tag{C.14}$$

where θ is a user-specified parameter to control the error. A smaller θ gives a more accurate result, at the same time, the speed will be low. A good value for θ would be 0.5, however, we will use 0.3 for the following tests.

The pseudocode for treecode method is shown in Table C.1, the languages used in our implementation are Python and C. Meshes, magnetization configuration and

demagnetizing field calculation from magnetic potential parts are written in Python. Treecode parts are implemented in C and are wrapped by Cython from which these C functions can be called using Python directly.

C.2.1 Combine Treecode with FEM/BEM

In the hybrid finite element method/boundary element method (FEM/BEM), the surface integral for U_2 is computed analytically which leads to a dense matrix, to avoid using dense matrix we need to come back to the original integral for U_2:

$$U_2(\mathbf{x}) = \frac{1}{4\pi} \oint_{\partial V} U_1(\mathbf{y}) \nabla_y \frac{1}{|\mathbf{x}-\mathbf{y}|} \cdot \mathbf{n}_y \mathrm{d}S + \left(\frac{\Omega(\mathbf{x})}{4\pi} - 1 \right) U_1(\mathbf{x}). \tag{C.15}$$

Noticing that the first term in Eq. (C.15) can be discretized into the general summation [Eq. (C.1)] using numerical integral scheme:

$$\int_{\partial V_c} U_1(\mathbf{y}) \nabla_y \frac{1}{|\mathbf{x}-\mathbf{y}|} \cdot \mathbf{n}_y \mathrm{d}S \approx \sum_j U_1(\mathbf{y}_j) S_j \mathbf{F}(\mathbf{y}_j) \cdot \mathbf{n}_{y_j} = V_{i,c} \tag{C.16}$$

where

$$\mathbf{F}(\mathbf{y}) = \nabla_y \frac{1}{|\mathbf{x}-\mathbf{y}|} = \nabla_y \phi(\mathbf{x}, \mathbf{y}). \tag{C.17}$$

However, this approximation is not accurate if the distance between target and source particles is small, in this case we need to compute it analytically. Therefore, we define a critical radius $\tilde{R}_c = R_c l_c$ so that if $R < \tilde{R}_c$, the analytical equation will be used to calculate the potential; l_c is the characteristic length of the cells for the given mesh. This extra step slows down the whole algorithm slightly because for some points we need to compute it using Treecode method first, then subtract it using direct method, and lastly sum it using analytical expression again, this could happen since in the correction step we have used the sphere structure while the basic structure in Treecode method is rectangle box. In our implementation, we try to avoid this by computing the whole leaf using direct method with the assumption that the correct radius and the minimum tree radius are at the same scale. By inserting Eq. (C.6) into Eq. (C.16), we obtain,

$$\begin{aligned} V_{i,c} &= \sum_{||\mathbf{k}||=0} \frac{1}{\mathbf{k}!} D_{\mathbf{y}}^{\mathbf{k}} \phi(\mathbf{x}_i, \mathbf{y}_c) \sum_{\mathbf{y}_j \in c} q_j \nabla_{y_j} (\mathbf{y}_j - \mathbf{y}_c)^{\mathbf{k}} \cdot \mathbf{n}_{y_j} \\ &\approx \sum_{||\mathbf{k}||=0}^{p} a^{\mathbf{k}}(\mathbf{x}_i, \mathbf{y}_c) M_c^{\mathbf{k}}, \end{aligned} \tag{C.18}$$

where

$$\begin{aligned} q_j &= U_1(\mathbf{y}_j) S_j \\ M_c^{\mathbf{k}} &= \sum_{\mathbf{y}_j \in c} q_j \nabla_{y_j} (\mathbf{y}_j - \mathbf{y}_c)^{\mathbf{k}} \cdot \mathbf{n}_{y_j} \end{aligned} \tag{C.19}$$

and $a^{\mathbf{k}}(\mathbf{x}_i, \mathbf{y}_c)$ is same as in Eq. (C.8).

C.3 Numerical Tests

We have implemented Treecode method the algorithm described above: coefficients are calculated using recursive relation and the correction will be taken according to sphere radius. There are four parameters to be test in this Treecode-BEM algorithm: θ, p, N_0 and R_c – the first three determine the performance and the last one decides both the memory usage and accuracy.

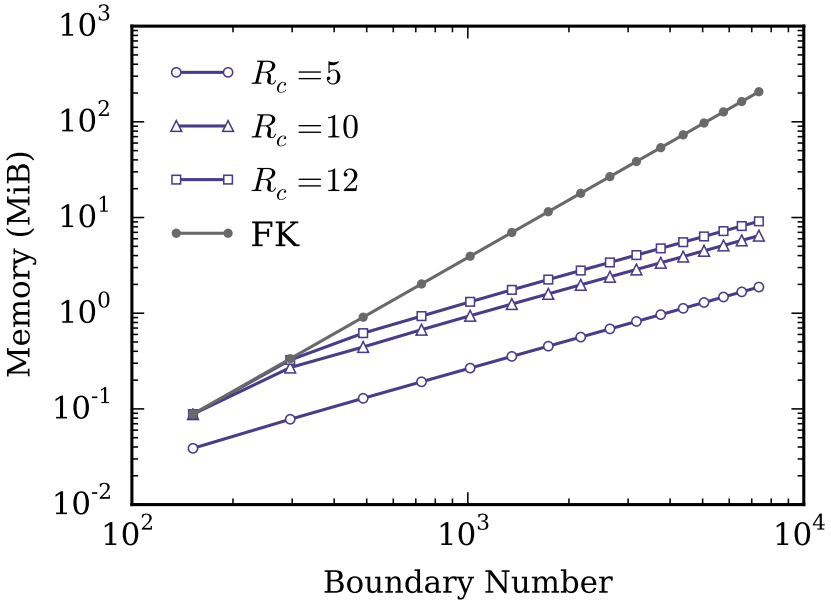

Figure C.2: The memory usage for Treecode-BEM comparing with FK method.

We will use a unit cube mesh for the testing. Figure C.2 shows the memory usages as a function of the number of boundary vertices for Treecode and CG methods. As we can see, the memory usage scales with N^2 for FK method while only scales with $\sim N\log(N)$ for Treecode methods, and a larger R_c costs more memory.

The total demagnetization energy for the unit cube mesh with uniform magnetization $(1,0,0)$ is $E_0 = -(1/6)\mu_0 M_s^2$. The relative error of the demagnetization energy for both FK and Treecode methods are shown in Fig. C.3(a). It can be seen that both methods converge. Very interestingly, $R_c = 0$ gives a better demagnetization energy. However, this does not mean $R_c = 0$ is better than $R_c = 0$. In principle FK method is the limit case of $R_c \to \infty$ in Treecode method, so we stick to that FK is the standard and parameters chosen in Treecode should lead to a bounded relative error with respect to FK results.

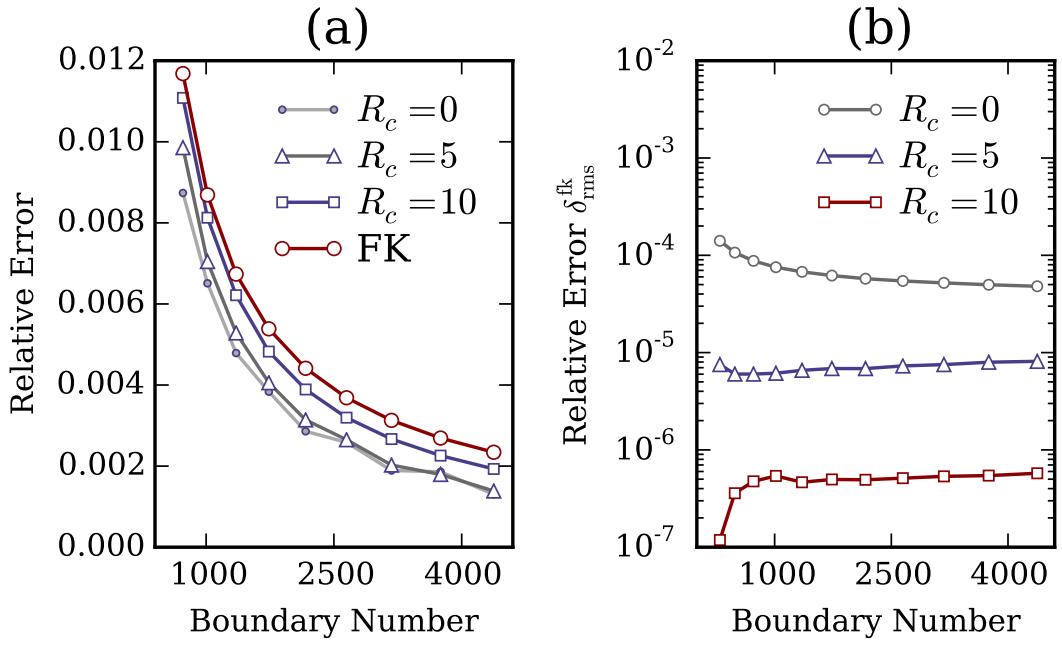

Figure C.3: (a) The relative error of the demagnetization energy for FK and Treecode methods. (b) The relative error respect to FK method ($\delta^{\text{fk}}_{\text{rms}}$) for a unit cube mesh with uniform magnetization $(0, 0, 1)$. The parameters used are $\theta = 0.3$, $p = 4$, and $N_0 = 100$.

The influence of R_c can be qualified by defining the relative error:

$$\delta^{\text{fk}}_{\text{rms}} = \sqrt{\frac{\sum_{i=1}^{N}\sum_{j=1}^{3}(H^i_{\text{d,j,tr}} - H^i_{\text{d,j,fk}})^2}{\sum_{i=1}^{N}\sum_{j=1}^{3}(H^i_{\text{d,j,fk}})^2}}. \tag{C.20}$$

Figure C.3(b) shows the relative error $\delta^{\text{fk}}_{\text{rms}}$ as a function of boundary number for different R_c. As expected, a larger R_c gives a smaller $\delta^{\text{fk}}_{\text{rms}}$. Therefore, for practical applications we can choose $R_c = 10$. Another important concern is the running time. Figure C.4 shows the comparison of running time for Treecode and FK methods. As we can see, the Treecode method is slower than the FK method. We also implement a simplified version which is slightly faster than the Treecode method described above.

C.4 Improvement

As shown in Fig. (C.4), the standard version is 2-3 times slower than the FK method. The reasons probably are:

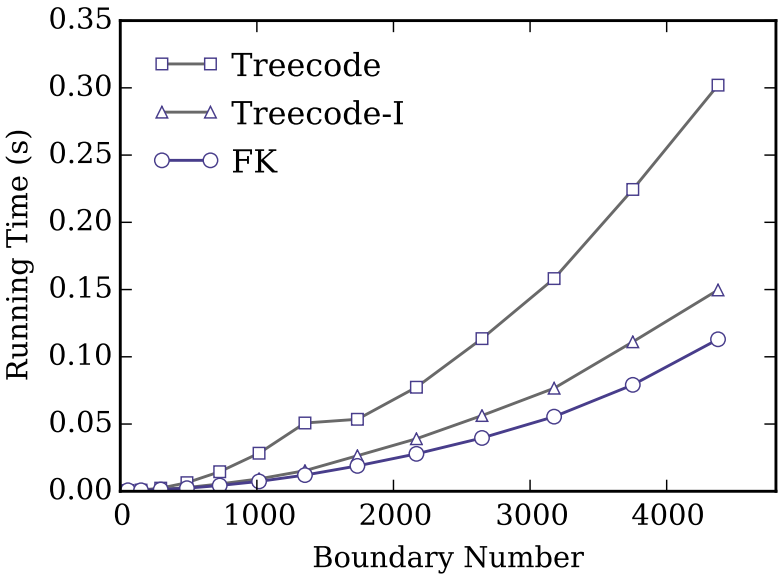

Figure C.4: Running time for FK method and Treecode method with parameters used are $\theta = 0.3$, $p = 4$, and $N_0 = 100$.

1. The direct computation is expensive: we have defined a radius R_c within which a sphere is constructed, all the points in the sphere are computed using analytical equations, the points beyond the sphere but not far away enough (i.e. $R\theta < r_c$) are computed using directly method.

2. The recursive method to compute the coefficients are not fast enough, for example, memory clash might be serious in our three-dimensional array.

Therefore, the possible ways to improve the performance are

1. Replace the direct computation by analytical equations and the price is a bit more memory, i.e., $\approx N \log N$. Because of this change, we are not going to correct according to the sphere radius, so we hope the minimum tree radius r_c and correct radius R_c satisfy

$$r_c > \frac{\theta}{1-\theta} R_c. \tag{C.21}$$

   Furthermore, we still employ the directly calculation if the particle number in a leaf is smaller than 10.

2. Using the directly method to compute the coefficients (needs to optimize manually such as find the common terms to reduce computation times) and using one dimensional array to avoid memory clash. (Note that there are some discussions about the traceless Maxwell-Cartesian tensor which might be useful [175], but we neglect this at the moment)

Figure (C.4) shows the running time for the simplified Treecode method – Treecode-I. As we can see, Treecode-I is almost as fast as FK method. In this simplified implementation, N_0, the default maximum number of particles N_0 that each leaf contains is set to 1, thus, the tree radius is totally determined by R_c. Due to the coefficients are computed using direct method, the two major variables in Treecode-I are θ and R_c.

C.5 Summary

We have implemented the Treecode-BEM method to compute the demagnetizing field. The memory usage of Treecode method scale with $N \log N$ where N is the number of boundary vertices. A simplified version (Treecode-I) is implemented as well. The simplified version is as fast as FK method.

Bibliography

[1] W. Wang, M. Dvornik, M.-a. Bisotti, D. Chernyshenko, M. Beg, M. Albert, A. Vansteenkiste, B. V. Waeyenberge, A. N. Kuchko, V. V. Kruglyak, and H. Fangohr, Physical Review B **92**, 054430 (2015).

[2] W. Wang, M. Albert, M. Beg, M.-A. Bisotti, D. Chernyshenko, D. Cortés-Ortuño, I. Hawke, and H. Fangohr, Phys. Rev. Lett. **114**, 087203 (2015).

[3] W. Wang, M. Beg, B. Zhang, W. Kuch, and H. Fangohr, Phys. Rev. B **92**, 020403 (2015).

[4] J. B. Carlson, Science **189**, 753 (1975).

[5] R. L. Stamps, S. Breitkreutz, J. Å kerman, A. V. Chumak, Y. Otani, G. E. W. Bauer, J.-U. Thiele, M. Bowen, S. a. Majetich, M. Kläui, I. L. Prejbeanu, B. Dieny, N. M. Dempsey, and B. Hillebrands, J. Phys. D. Appl. Phys. **47**, 333001 (2014).

[6] J. Lenz and A. S. Edelstein, IEEE Sens. J. **6**, 631 (2006).

[7] M. Niemier, Nat. Nanotechnol. **9**, 14 (2014).

[8] T. Gilbert, IEEE Trans. Magn. **40**, 3443 (2004).

[9] B. Skubic, J. Hellsvik, L. Nordström, and O. Eriksson, J. Phys. Condens. Matter **20**, 315203 (2008).

[10] V. V. Kruglyak and A. N. Kuchko, Phys. B Condens. Matter **339**, 130 (2003).

[11] V. V. Kruglyak, S. O. Demokritov, and D. Grundler, J. Phys. D. Appl. Phys. **43**, 264001 (2010).

[12] S. Neusser and D. Grundler, Adv. Mater. **21**, 2927 (2009).

[13] J. Podbielski, F. Giesen, and D. Grundler, Phys. Rev. Lett. **96**, 167207 (2006).

[14] C. Rüegg, A. Furrer, D. Sheptyakov, T. Strässle, K. W. Krämer, H. U. Güdel, and L. Mélési, Phys. Rev. Lett. **93**, 257201 (2004).

[15] S. O. Demokritov, V. E. Demidov, O. Dzyapko, G. A. Melkov, A. A. Serga, B. Hillebrands, and A. N. Slavin, Nature **443**, 430 (2006).

[16] V. E. Demidov, O. Dzyapko, S. O. Demokritov, G. A. Melkov, and A. N. Slavin, Phys. Rev. Lett. **100**, 047205 (2008).

[17] I. S. Tupitsyn, P. C. E. Stamp, and A. L. Burin, Phys. Rev. Lett. **100**, 257202 (2008).

[18] S.-K. Kim, J. Phys. D. Appl. Phys. **43**, 264004 (2010).

[19] M. Kostylev, A. Stashkevich, and N. Sergeeva, Phys. Rev. B **69**, 064408 (2004).

[20] J. Topp, J. Podbielski, D. Heitmann, and D. Grundler, Phys. Rev. B **78**, 024431 (2008).

[21] M. Kostylev, P. Schrader, R. L. Stamps, G. Gubbiotti, G. Carlotti, A. O. Adeyeye, S. Goolaup, and N. Singh, Appl. Phys. Lett. **92**, 132504 (2008).

[22] K. S. Lee, D. S. Han, and S. K. Kim, Phys. Rev. Lett. **102**, 127202 (2009).

[23] A. V. Chumak, V. I. Vasyuchka, A. A. Serga, M. P. Kostylev, V. S. Tiberkevich, and B. Hillebrands, Phys. Rev. Lett. **108**, 257207 (2012).

[24] M. Donahue and D. Porter, "OOMMF User's Guide, Version 1.0," (1999), http://math.nist.gov/oommf/.

[25] W. Scholz, J. Fidler, T. Schrefl, D. Suess, R. Dittrich, H. Forster, and V. Tsiantos, Comput. Mater. Sci. **28**, 366 (2003).

[26] T. Fischbacher, M. Franchin, G. Bordignon, and H. Fangohr, IEEE Trans. Magn. **43**, 2896 (2007).

[27] R. Chang, M. a. Escobar, S. Li, M. V. Lubarda, and V. Lomakin, J. Appl. Phys. **111**, 07D129 (2012).

[28] S. Zhang and Z. Li, Phys. Rev. Lett. **93**, 127204 (2004).

[29] S. R. Boona, R. C. Myers, and J. P. Heremans, Energy Environ. Sci. **7**, 885 (2014).

[30] D. Hinzke and U. Nowak, Phys. Rev. Lett. **107**, 027205 (2011).

[31] J.-i. Ohe, H. Adachi, S. Takahashi, and S. Maekawa, Phys. Rev. B **83**, 1 (2011).

[32] K. Everschor, M. Garst, B. Binz, F. Jonietz, S. Mühlbauer, C. Pfleiderer, and A. Rosch, Phys. Rev. B **86**, 054432 (2012).

[33] L. Kong and J. Zang, Phys. Rev. Lett. **111**, 067203 (2013).

[34] W. Jiang, P. Upadhyaya, Y. Fan, J. Zhao, M. Wang, L. T. Chang, M. Lang, K. L. Wong, M. Lewis, Y. T. Lin, J. Tang, S. Cherepov, X. Zhou, Y. Tserkovnyak, R. N. Schwartz, and K. L. Wang, Phys. Rev. Lett. **110**, 1 (2013).

[35] S. Borlenghi, W. Wang, H. Fangohr, L. Bergqvist, and A. Delin, Phys. Rev. Lett. **112**, 047203 (2014).

[36] X.-G. Wang, G.-H. Guo, Y.-Z. Nie, G.-F. Zhang, and Z.-X. Li, Phys. Rev. B **86**, 054445 (2012).

[37] V. Baryakhtar, B. Ivanov, A. Sukstanskii, and E. Melikhov, Physical Review B **56**, 619 (1997).

[38] R. Urban, G. Woltersdorf, and B. Heinrich, Physical Review Letters **87**, 217204 (2001).

[39] V. L. Safonov, Journal of Applied Physics **91**, 8653 (2002).

[40] L. De Angeli, D. Steiauf, R. Singer, I. Köberle, F. Dietermann, and M. Fähnle, Phys. Rev. B **79**, 052406 (2009).

[41] H. T. Nembach, J. M. Shaw, C. T. Boone, and T. J. Silva, Phys. Rev. Lett. **110**, 117201 (2013).

[42] Y. Tserkovnyak, A. Brataas, and G. Bauer, Physical Review Letters **88**, 117601 (2002).

[43] I. Dzyaloshinskii, J. Phys. Chem. Solids **4**, 241 (1958).

[44] T. Moriya, Phys. Rev. **120**, 91 (1960).

[45] A. Thiaville, S. Rohart, E. Jué, V. Cros, and A. Fert, Europhys. Lett. **100**, 57002 (2012).

[46] O. A. Tretiakov and A. Abanov, Phys. Rev. Lett. **105**, 157201 (2010).

[47] N. Nagaosa and Y. Tokura, Nat. Nanotechnol. **8**, 899 (2013).

[48] S.-Z. Lin, C. Reichhardt, C. D. Batista, and A. Saxena, Phys. Rev. Lett. **110**, 207202 (2013).

[49] J. Iwasaki, M. Mochizuki, and N. Nagaosa, Nat. Commun. **4**, 1463 (2013).

[50] Y.-H. Liu, Y.-Q. Li, and J. H. Han, Phys. Rev. B **87**, 100402 (2013).

[51] J. Iwasaki, A. J. Beekman, and N. Nagaosa, Phys. Rev. B **89**, 064412 (2014).

[52] H. Kronmüller, in *Handbook of Magnetism and Advanced Magnetic Materials* (John Wiley & Sons, Ltd, 2007).

[53] D. Wei, in *Micromagnetics and Recording Materials* (Springer Berlin Heidelberg, 2012).

[54] S. Blundell, *Magnetism in Condensed Matter*, Oxford Master Series in Condensed Matter Physics (OUP Oxford, 2001).

[55] R. F. L. Evans, W. J. Fan, P. Chureemart, T. A. Ostler, M. O. A. Ellis, and R. W. Chantrell, J. Phys. Condens. Matter **26**, 103202 (2014).

[56] U. Nowak, in *Handbook of Magnetism and Advanced Magnetic Materials* (John Wiley & Sons, Ltd, 2007).

[57] G. Tatara, H. Kohno, and J. Shibata, Phys. Rep. **468**, 213 (2008).

[58] C. P. Slichter, *Principles of Magnetic Resonance*, Springer Series in Solid-State Sciences (Springer, 1990).

[59] R. Wieser, Eur. Phys. J. B **88**, 77 (2015).

[60] J. Stöhr and H. C. Siegmann, *Magnetism: From Fundamentals to Nanoscale Dynamics*, Springer Series in Solid-State Sciences (Springer Berlin Heidelberg, 2006).

[61] A. Fert, V. Cros, and J. Sampaio, Nat. Nanotechnol. **8**, 152 (2013).

[62] S. Rohart and A. Thiaville, Phys. Rev. B **88**, 184422 (2013).

[63] S. Mühlbauer, B. Binz, F. Jonietz, C. Pfleiderer, A. Rosch, A. Neubauer, R. Georgii, and P. Böni, Science **323**, 915 (2009).

[64] S. X. Huang and C. L. Chien, Phys. Rev. Lett. **108**, 267201 (2012).

[65] J. L. García-Palacios and F. J. Lázaro, Phys. Rev. B **58**, 14937 (1998).

[66] L. D. Landau and E. Lifshitz, Phys. Z. Sowjetunion **8**, 101 (1935).

[67] L. Berger, Phys. Rev. B **54**, 9353 (1996).

[68] J. Slonczewski, J. Magn. Magn. Mater. **159**, L1 (1996).

[69] A. Thiaville, Y. Nakatani, J. Miltat, and Y. Suzuki, Europhys. Lett. **69**, 990 (2005).

[70] D. Claudio-Gonzalez, A. Thiaville, and J. Miltat, Phys. Rev. Lett. **108**, 227208 (2012).

[71] A. Logg and G. N. Wells, ACM Trans. Math. Softw. **37**, 2 (2010).

[72] J. E. Miltat and M. J. Donahue, in *Handbook of Magnetism and Advanced Magnetic Materials* (John Wiley & Sons, Ltd, 2007).

[73] A. J. Newell, W. Williams, and D. J. Dunlop, J. Geophys. Res. **98**, 9551 (1993).

[74] T. Okubo, S. Chung, and H. Kawamura, Phys. Rev. Lett. **108**, 017206 (2012).

[75] J. Struck, M. Weinberg, C. Ölschläger, P. Windpassinger, J. Simonet, K. Sengstock, R. Höppner, P. Hauke, A. Eckardt, M. Lewenstein, and L. Mathey, Nat. Phys. **9**, 738 (2013).

[76] M. d'Aquino, C. Serpico, G. Miano, and C. Forestiere, J. Comput. Phys. **228**, 6130 (2009).

[77] S.-Z. Lin, C. D. Batista, and A. Saxena, Phys. Rev. B **89**, 024415 (2014).

[78] N. L. Schryer and L. R. Walker, J. Appl. Phys. **45**, 5406 (1974).

[79] A. Goussev, J. Robbins, and V. Slastikov, Phys. Rev. Lett. **104**, 147202 (2010).

[80] K. Y. Guslienko, IEEE Magn. Lett. **6**, 4000104 (2015).

[81] C. Schütte and M. Garst, Phys. Rev. B **90**, 094423 (2014).

[82] A. A. Belavin and A. M. Polyakov, JETP Lett. **22**, 245 (1975).

[83] E. Martinez, L. Lopez-Diaz, L. Torres, C. Tristan, and O. Alejos, Phys. Rev. B **75**, 174409 (2007).

[84] D. V. Berkov, in *Handbook of Magnetism and Advanced Magnetic Materials* (John Wiley & Sons, Ltd, 2007).

[85] A. R. Soheili and M. Namjoo, World J. Model. Simulat. **4**, 83 (2008).

[86] N. Kasdin, J. Guid. Control. Dyn. **18**, 114 (1995).

[87] A. Tocino and R. Ardanuy, J. Comput. Appl. Math. **138**, 219 (2002).

[88] F. Costabile and A. Napoli, Appl. Numer. Math. **61**, 160 (2011).

[89] K. Burrage and P. Burrage, Appl. Numer. Math. **22**, 81 (1996).

[90] R. Mannella, Int. J. Mod. Phys. C **13**, 1177 (2002).

[91] M. d'Aquino, C. Serpico, G. Coppola, I. D. Mayergoyz, and G. Bertotti, J. Appl. Phys. **99**, 08B905 (2006).

[92] J. H. Mentink, M. V. Tretyakov, A. Fasolino, M. I. Katsnelson, and T. Rasing, J. Phys. Condens. Matter **22**, 176001 (2010).

[93] M. Khodabin, K. Maleknejad, M. Rostami, and M. Nouri, Math. Comput. Model. **53**, 1910 (2011).

[94] W. Scholz, T. Schrefl, and J. Fidler, J. Magn. Magn. Mater. **233**, 296 (2001).

[95] F. Romá, L. F. Cugliandolo, and G. S. Lozano, Phys. Rev. E **90**, 023203 (2014).

[96] D. V. Berkov and N. L. Gorn, J. Phys. D. Appl. Phys. **41**, 164013 (2008).

[97] A. Vansteenkiste, J. Leliaert, M. Dvornik, F. Garcia-Sanchez, and B. Van Waeyenberge, AIP Adv. **4**, 107133 (2014).

[98] Y. Shu, M. Lin, and K. Wu, Mech. Mater. **36**, 975 (2004).

[99] N. Vukadinovic, J. Ben Youssef, H. Le Gall, and J. Ostorero, Phys. Rev. B **62**, 9021 (2000).

[100] S.-M. Seo, K.-J. Lee, H. Yang, and T. Ono, Phys. Rev. Lett. **102**, 147202 (2009).

[101] M. Mruczkiewicz, M. Krawczyk, R. V. Mikhaylovskiy, and V. V. Kruglyak, Physical Review B **86**, 024425 (2012).

[102] M. C. Hickey and J. S. Moodera, Phys. Rev. Lett. **102**, 137601 (2009).

[103] E. M. Hankiewicz, G. Vignale, and Y. Tserkovnyak, Phys. Rev. B **78**, 020404 (2008).

[104] M. Fähnle and S. Zhang, J. Magn. Magn. Mater. **326**, 232 (2013).

[105] Y. Tserkovnyak, E. M. Hankiewicz, and G. Vignale, Phys. Rev. B **79**, 094415 (2009).

[106] S. Zhang and S. S.-L. Zhang, Phys. Rev. Lett. **102**, 086601 (2009).

[107] A. I. Akhiezer, V. G. Bar'yakhtar, and S. V. Peletminskii, *Spin Waves* (North-Holland, Amsterdam, 1968).

[108] V. Baryakhtar, in *Frontiers in Magnetism of Reduced Dimension Systems*, NATO ASI Series, Vol. 49, edited by V. Bar'yakthar, P. Wigen, and N. Lesnik (Springer Netherlands, 1998) pp. 63–94.

[109] V. G. Bar'yakhtar, B. A. Ivanov, T. K. Soboleva, and A. L. Sukstanskii, Zh. Eksp. Teor. Fiz **64**, 857 (1986).

[110] V. G. Baryakhtar and A. G. Danilevich, Low Temp. Phys. **39**, 993 (2013).

[111] B. Hillebrands and A. Thiaville, *Spin Dynamics in Confined Magnetic Structures III* (Springer, New York, 2006).

[112] T. Weindler, H. G. Bauer, R. Islinger, B. Boehm, J.-Y. Chauleau, and C. H. Back, Phys. Rev. Lett. **113**, 237204 (2014).

[113] M. Dvornik, A. Vansteenkiste, and B. Van Waeyenberge, Phys. Rev. B **88**, 054427 (2013).

[114] U. Atxitia and O. Chubykalo-Fesenko, Phys. Rev. B **84**, 144414 (2011).

[115] D.-S. Han, S.-K. Kim, J.-Y. Lee, S. J. Hermsdoerfer, H. Schultheiss, B. Leven, and B. Hillebrands, Appl. Phys. Lett. **94**, 112502 (2009).

[116] V. G. Baryakhtar, Low Temp. Phys. **40**, 626 (2014).

[117] Y. Nakatani, A. Thiaville, and J. Miltat, J. Magn. Magn. Mater. **290**, 750 (2005).

[118] L. O'Brien, E. R. Lewis, A. Fernández-Pacheco, D. Petit, R. P. Cowburn, J. Sampaio, and D. Read, Phys. Rev. Lett. **108**, 187202 (2012).

[119] V. L. Sobolev, S. C. Chen, and H. L. Huang, J. Magn. Magn. Mater. **172**, 83 (1997).

[120] J. Shibata, G. Tatara, and H. Kohno, J. Phys. D. Appl. Phys. **44**, 384004 (2011).

[121] D. A. Allwood, G. Xiong, C. C. Faulkner, D. Atkinson, D. Petit, and R. P. Cowburn, Science **309**, 1688 (2005).

[122] R. Hertel, W. Wulfhekel, and J. Kirschner, Phys. Rev. Lett. **93**, 257202 (2004).

[123] R. Wieser, U. Nowak, and K. Usadel, Phys. Rev. B **69**, 064401 (2004).

[124] S. S. P. Parkin, M. Hayashi, and L. Thomas, Science **320**, 190 (2008).

[125] B. Hu and X. R. Wang, Phys. Rev. Lett. **111**, 027205 (2013).

[126] P. Yan and X. R. Wang, Phys. Rev. B **80**, 214426 (2009).

[127] P. Yan and X. Wang, Phys. Rev. Lett. **107**, 177207 (2011).

[128] X. S. Wang, P. Yan, Y. H. Shen, G. E. W. Bauer, and X. R. Wang, Phys. Rev. Lett. **109**, 167209 (2012).

[129] J.-S. Kim, M. Stärk, M. Kläui, J. Yoon, C.-Y. You, L. Lopez-Diaz, and E. Martinez, Phys. Rev. B **85**, 174428 (2012).

[130] P. Yan, A. Kamra, Y. Cao, and G. E. W. Bauer, Phys. Rev. B **88**, 144413 (2013).

[131] A. Janutka, IEEE Magn. Lett. **4**, 4000104 (2013).

[132] J. Zang, M. Mostovoy, J. H. Han, and N. Nagaosa, Phys. Rev. Lett. **107**, 136804 (2011).

[133] J.-H. Moon, S.-M. Seo, K.-J. Lee, K.-W. Kim, J. Ryu, H.-W. Lee, R. McMichael, and M. Stiles, Phys. Rev. B **88**, 184404 (2013).

[134] N. A. Porter, J. C. Gartside, and C. H. Marrows, Phys. Rev. B **90**, 024403 (2014).

[135] H.-B. Braun, Phys. Rev. B **50**, 16 485 (1994).

[136] J. Lekner, Am. J. Phys. **75**, 1151 (2007).

[137] E. G. Tveten, A. Qaiumzadeh, and A. Brataas, Phys. Rev. Lett. **112**, 147204 (2014).

[138] P. Yan and G. Bauer, Phys. Rev. Lett. **109**, 087202 (2012).

[139] K. Zakeri, Y. Zhang, J. Prokop, T.-H. Chuang, N. Sakr, W. X. Tang, and J. Kirschner, Phys. Rev. Lett. **104**, 137203 (2010).

[140] A. Kosevich, B. Ivanov, and A. Kovalev, Phys. Rep. **194**, 117 (1990).

[141] T. H. R. Skyrme, Nucl. Phys. **31**, 556 (1962).

[142] X. Z. Yu, Y. Onose, N. Kanazawa, J. H. Park, J. H. Han, Y. Matsui, N. Nagaosa, and Y. Tokura, Nature **465**, 901 (2010).

[143] S. Heinze, K. von Bergmann, M. Menzel, J. Brede, A. Kubetzka, R. Wiesendanger, G. Bihlmayer, and S. Blügel, Nat. Phys. **7**, 713 (2011).

[144] N. Romming, C. Hanneken, M. Menzel, J. E. Bickel, B. Wolter, K. von Bergmann, A. Kubetzka, and R. Wiesendanger, Science **341**, 636 (2013).

[145] N. Romming, A. Kubetzka, C. Hanneken, K. von Bergmann, and R. Wiesendanger, Phys. Rev. Lett. **114**, 177203 (2015).

[146] U. K. Rössler, A. N. Bogdanov, and C. Pfleiderer, Nature **442**, 797 (2006).

[147] J. Iwasaki, M. Mochizuki, and N. Nagaosa, Nat. Nanotechnol. **8**, 742 (2013).

[148] S.-Z. Lin, C. D. Batista, C. Reichhardt, and A. Saxena, Phys. Rev. Lett. **112**, 187203 (2014).

[149] M. Mochizuki, X. Z. Yu, S. Seki, N. Kanazawa, W. Koshibae, J. Zang, M. Mostovoy, Y. Tokura, and N. Nagaosa, Nat. Mater. **13**, 241 (2014).

[150] Y.-T. Oh, H. Lee, J.-H. Park, and J. H. Han, Phys. Rev. B **91**, 104435 (2015).

[151] M. Mochizuki, Phys. Rev. Lett. **108**, 017601 (2012).

[152] Y. Onose, Y. Okamura, S. Seki, S. Ishiwata, and Y. Tokura, Phys. Rev. Lett. **109**, 037603 (2012).

[153] Y. Okamura, F. Kagawa, M. Mochizuki, M. Kubota, S. Seki, S. Ishiwata, M. Kawasaki, Y. Onose, and Y. Tokura, Nat. Commun. **4**, 2391 (2013).

[154] T. Schwarze, J. Waizner, M. Garst, A. Bauer, I. Stasinopoulos, H. Berger, C. Pfleiderer, and D. Grundler, Nat. Mater. **14**, 478 (2015).

[155] A. Neubauer, C. Pfleiderer, B. Binz, A. Rosch, R. Ritz, P. G. Niklowitz, and P. Böni, Phys. Rev. Lett. **102**, 186602 (2009).

[156] Y. Zhou and M. Ezawa, Nat. Commun. **5**, 4652 (2014).

[157] S. D. Yi, S. Onoda, N. Nagaosa, and J. H. Han, Phys. Rev. B **80**, 054416 (2009).

[158] B. Zhang, W. Wang, M. Beg, H. Fangohr, and W. Kuch, Appl. Phys. Lett. **106**, 102401 (2015).

[159] R. P. Cowburn, D. K. Koltsov, A. O. Adeyeye, M. E. Welland, and D. M. Tricker, Phys. Rev. Lett. **83**, 1042 (1999).

[160] R. Liu, J. Wang, Q. Liu, H. Wang, and C. Jiang, J. Appl. Phys. **103**, 013910 (2008).

[161] J.-V. Kim, F. Garcia-Sanchez, J. Sampaio, C. Moreau-Luchaire, V. Cros, and A. Fert, Phys. Rev. B **90**, 064410 (2014).

[162] N. Papanicolaou and T. Tomaras, Nucl. Phys. B **360**, 425 (1991).

[163] A. A. Kovalev, Phys. Rev. B **89**, 241101 (2014).

[164] A. A. Thiele, Phys. Rev. Lett. **30**, 230 (1973).

[165] P. Reimann, Phys. Rep. **361**, 57 (2002).

[166] P. Hänggi and F. Marchesoni, Rev. Mod. Phys. **81**, 387 (2009).

[167] N. R. Quintero, J. A. Cuesta, and R. Alvarez-Nodarse, Phys. Rev. E **81**, 030102 (2010).

[168] E. Beaurepaire, J.-C. Merle, A. Daunois, and J.-Y. Bigot, Phys. Rev. Lett. **76**, 4250 (1996).

[169] C. Jarzynski, Phys. Rev. Lett. **78**, 2690 (1997).

[170] G. E. Crooks, Phys. Rev. E **60**, 2721 (1999).

[171] M. Rognes, R. Kirby, and A. Logg, SIAM J. Sci. Comput. **31**, 4130 (2009).

[172] M. F. Wheeler and I. Yotov, SIAM J. Numer. Anal. **44**, 2082 (2006).

[173] J. Barnes and P. Hut, Nature **324**, 446 (1986).

[174] P. Li, H. Johnston, and R. Krasny, J. Comput. Phys. **228**, 3858 (2009).

[175] B. Shanker and H. Huang, J. Comput. Phys. **226**, 732 (2007).